Electroreductive Desorption of Alkanethiols on Metal Surfaces Using In-situ Second Harmonic Generation

A Dissertation Presented to

the Faculty of the Department of Chemistry

University of Houston

In Partial Fulfillment

of the Requirements for the Degree

Doctor of Philosophy

By

Michelle DeLeon

May 2019

Electroreductive Desorption of Alkanethiols on Metal Surfaces Using In-situ Second Harmonic Generation

_____
Michelle DeLeon

APPROVED:

_____
Dr. Steven Baldelli, Chairman

_____
Dr. Shoujun Xu

_____
Dr. Roman S. Czernuszewicz

_____
Dr. Melissa Zastrow

_____
Dr. Luis Garfias

_____
Dr. Dan E. Wells, Dean, College of Natural
Sciences and Mathematics

Electroreductive Desorption of Alkanethiols on Metal Surfaces Using In-situ Second Harmonic Generation

An Abstract of a Dissertation

Presented to

the Faculty of the Department of Chemistry

University of Houston

In Partial Fulfillment

of the Requirements for the Degree

Doctor of Philosophy

By

Michelle DeLeon

May 2019

iii

Abstract

Surfaces are continually exposed to different environments such as gases, liquids, or even other solids. At these interfaces, many chemical reactions occur. The corrosion of metals is a widely studied phenomena in both academia and industry. At the metal-solution interface, processes such as self-assembled monolayers (SAMs) and underpotential deposition (UPD) can be used to inhibit corrosion. In-situ second harmonic generation (SHG) allows these processes to be monitored in real-time. Coupling with cyclic voltammetry (CV), the electrodesorption of three alkanethiols was observed for a gold and copperUPD-gold electrode. The SH response, as a function of potential, was sensitive to changes at the electrode surfaces as alkanethiols were reductively desorbed. After 30 CV sweeps, decanethiol (DT) was shown to reductively desorb from both the gold and copperUPD-gold electrodes. Long chain alkanethiol, octadecanethiol (ODT), remained near the surface for both electrodes. However, for dodecanethiol (DDT), after 30 CV sweeps, DDT was reductively desorbed from the gold electrode, but remained near the surface of the copperUPD-gold electrode.

These results were confirmed with ex-situ sum frequency generation (SFG), X-ray photoelectron spectroscopy (XPS), and contact angle (CA) measurements. Compared to a gold electrode, the copperUPD-gold electrode showed differing responses in both the SH and cyclic voltammograms. The addition of the copper UPD layer stabilized the alkanethiols, which was evident not only by the presence of DDT after 30 CVs, but also by the increase in reductive potentials to more negative potentials than that for a gold

electrode. These effects were visualized by the variations in the SH response between the two electrode surfaces. By adding a copper UPD layer onto a gold surface, there is a change in capacitance in the system. This change is magnified by the SH response as alkanethiols are reductively desorbed from a gold and copperUPD-gold electrode surface.

To my parents who sacrificed so that I may have opportunities they were not given. Without their love and support, I would not have accomplished all that I have.

And to my dog, Thor. I work hard so that he may have a better life.

Table of Contents

List of Figures

List of Tables

List of Abbreviations

CA   contact angle

CE   counter electrode

CV   cyclic voltammetry

CW   continuous wave

DAQ   data acquisition

DDT   dodecanethiol

DT   decanethiol

HER   hydrogen evolution reaction

KTP   potassium titanyl phosophate

LBO   lithium triborate

MSE   mercury-mercurous sulfate electrode

ODT   octadecanethiol

PMT   photomultiplier tube

PTFE   polytetrafluoroethylene

RE   reference electrode

SAM   self-assembled monolayer

SFG   sum frequency generation

SH   second harmonic

SHE   standard hydrogen electrode

SHG   second harmonic generation

UPD   underpotential deposition

WE   working electrode

XPS   X-ray photoelectron spectroscopy

Chapter 1
Introduction

1.1 Motivation

Surfaces are the first thing that come in contact with the environment; therefore not only the surface but also the interface (the boundary between any two phases) is of great interest.[1] Here, many chemical reactions occur. Information about the interaction of the surface with its surrounding environment is obtained using surface chemistry. By studying the surface phenomena of adsorption and oxidation, insight is provided about a surface's chemical behavior.

An organic molecule that spontaneously adsorbs to a surface is known as a self-assembled monolayer (SAM).[2-4] Alkanethiol self-assembled monolayers (SAMs) have been well studied due to their ease of preparation and vast applications. Alkanethiols are stable in both vacuum and ambient pressure and form well-ordered structures. A SAM is made up of three parts: a headgroup, a backbone, and a terminal group. The headgroup guides the self-assembly process connecting the hydrocarbon chain to the metal surface. The backbone is a chain of hydrocarbons, which pack to form a monolayer through van der Waals and hydrophobic forces.[5] The structure of the SAM can be further stabilized with longer chain lengths. The terminal group contribute to surface properties, which can tailor a surface for specific applications. Thiolate SAMs on gold have been used as model systems in surface modification. The adsorption of thiolates on gold is shown in Equation

1.1.[5-6] However, at negative potentials, alkanethiols can reductively desorb from the gold surface. This process is explained in Equations 1.2 and 1.3, where first Au-SR is cleaved and then the desorbed thiolate species is dissolved into the electrolyte solution and then diffuse away from the surface.[6-7]
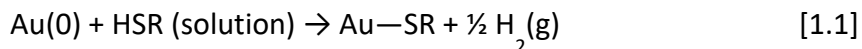
$$Au(0) + HSR \text{ (solution)} \rightarrow Au{-}SR + \frac{1}{2} H_2 \text{(g)} \qquad [1.1]$$

$$Au{-}SR + e^- \rightarrow Au(0) + {}^-SR \text{ (surface)} \qquad [1.2]$$

$$Au(0) + {}^-SR \text{ (surface)} \rightarrow Au(0) + {}^-SR \text{ (solution)} \qquad [1.3]$$

Underpotential deposition (UPD) is the phenomenon of the electrodeposition of a metal adlayer onto a dissimilar metal.[8] Generally, UPD forms adlayers with a coverage of no more than a monolayer. Both SAMs and UPD are used for surface modification, which have potential applications like wetting, lubrication, sensors, and corrosion inhibition. [9-16]

Second harmonic generation (SHG) is a second-order nonlinear optical technique where two photons of frequency ω interact with a material medium and generate a photon of twice the frequency, 2ω. Under the electric dipole approximation, SHG is only allowed when there is a break in symmetry. This provides a surface sensitive technique to probe the interface of two phases. Using SHG to probe solid-liquid interfaces, allows the technique to study surface modifications such as SAM and UPD. With the ability to monitor surface reactions in-situ, SHG is an excellent technique to work in parallel with cyclic voltammetry (CV). Maintaining a consistent environment helps eliminate

2

complicating factors to an already complex system. Using both SHG and CV, real-time information was acquired for studying the electrodesorption of alkanethiols from a gold and copperUPD-gold electrode.

1.2 Overview

The second chapter gives the theoretical background for second harmonic generation (SHG) and electrochemistry. For SHG, there is an overview of the technique as well as a more in-depth discussion about the second order nonlinear susceptibility. Two main uses of SHG are for rotational anisotropy and surface coverage. Examples of each are given. A brief overview of electrochemistry is provided as well as the specific methods of cyclic voltammetry (CV) and underpotential deposition (UPD).

The third chapter outlines optical components and characterization for experiments. Starting with optical set-ups, this chapter gives a thorough description of the optical layouts, alignment, and optimization procedures constructed for experiments. Data processing is presented to show how the SH and CV data were collected and analyzed simultaneously. After a working set-up was designed and developed, a cell was designed and constructed for in-situ experiments. The design, description, and picture of different cells are presented. Finally, sample preparations for in-situ SH and electrochemical experiments are discussed.

The fourth chapter summarizes the experiments performed for the reductive desorption of n-alkanethiols on both a gold and copperUPD-gold electrode. In-situ SHG allowed the real-time data acquisition of the electrodesorption of a self-assembled

monolayer from a metal electrode. With the help of ex-situ techniques of sum frequency generation (SFG), X-ray photoelectron spectroscopy (XPS), and contact angle (CA), the reductive desorption of short chain alkanethiols was verified. While the electrodesorption of alkanethiols from a copperUPD-gold electrode was not seen through cyclic voltammetry, the SH was sensitive to changes occurring at the electrode surface. From the results, it was found that the copperUPD layer stabilized alkanethiols compared to a gold electrode.

1.3 References

1.   Somorjai, G. A.; Li, Y., *Introduction to Surface Chemistry and Catalysis*. John Wiley & Sons: 2010.

2.   Laibinis, P. E.; Bain, C. D.; Whitesides, G. M., Attenuation of photoelectrons in monolayers of n-alkanethiols adsorbed on copper, silver, and gold. *The Journal of Physical Chemistry* **1991,** *95* (18), 7017-7021.

3.   Schreiber, F., Structure and growth of self-assembling monolayers. *Progress in Surface Science* **2000,** *65* (5), 151-257.

4.   Porter, M. D.; Bright, T. B.; Allara, D. L.; Chidsey, C. E., Spontaneously organized molecular assemblies. 4. Structural characterization of n-alkyl thiol monolayers on gold by optical ellipsometry, infrared spectroscopy, and electrochemistry. *Journal of the American Chemical Society* **1987,** *109* (12), 3559-3568.

5.   Vericat, C.; Vela, M. E.; Benitez, G.; Carro, P.; Salvarezza, R. C., Self-assembled monolayers of thiols and dithiols on gold: new challenges for a well-known system. *Chemical Society Reviews* **2010,** *39* (5), 1805-1834.

6.   Cai, X.; Baldelli, S., Surface Barrier Properties of Self-Assembled Monolayers as Deduced by Sum Frequency Generation Spectroscopy and Electrochemistry. *The Journal of Physical Chemistry C* **2011,** *115* (39), 19178-19189.

7.   Widrig, C. A.; Chung, C.; Porter, M. D., The electrochemical desorption of n-alkanethiol monolayers from polycrystalline Au and Ag electrodes. *Journal of Electroanalytical Chemistry and Interfacial Electrochemistry* **1991,** *310* (1), 335-359.

8.   Jennings, G. K.; Laibinis, P. E., Self-Assembled n-Alkanethiolate Monolayers on

      Underpotentially Deposited Adlayers of Silver and Copper on Gold. *Journal of the*

      American Chemical Society **1997,** *119* (22), 5208-5214.

9.   Eisenthal, K., Liquid interfaces probed by second-harmonic and sum-frequency

      spectroscopy. *Chemical Reviews* **1996,** *96* (4), 1343-1360.

10.   Feng, Y.; Teo, W. K.; Siow, K. S.; Gao, Z.; Tan, K. L.; Hsieh, A. K., Corrosion

      protection of copper by a self-assembled monolayer of alkanethiol. *Journal of*

      The Electrochemical Society **1997,** *144* (1), 55-64.

11.   Hutt, D. A.; Liu, C., Oxidation protection of copper surfaces using self-assembled

      monolayers of octadecanethiol. *Applied Surface Science* **2005,** *252* (2), 400-411.

12.   Jennings, G. K.; Laibinis, P. E., Self-assembled monolayers of alkanethiols on

      copper provide corrosion resistance in aqueous environments. *Colloids and*

      Surfaces A: Physicochemical and Engineering Aspects **1996,** *116* (1), 105-114.

13.   Jennings, G. K.; Munro, J. C.; Yong, T.-H.; Laibinis, P. E., Effect of Chain Length on

      the Protection of Copper by n-Alkanethiols. *Langmuir* **1998,** *14* (21), 6130-6139.

14.   Laibinis, P. E.; Whitesides, G. M., Self-assembled monolayers of n-alkanethiolates

      on copper are barrier films that protect the metal against oxidation by air.

      Journal of the American Chemical Society **1992,** *114* (23), 9022-9028.

15.   Swalen, J. D.; Allara, D.; Andrade, J. D.; Chandross, E.; Garoff, S.; Israelachvili, J.;

      McCarthy, T.; Murray, R.; Pease, R., Molecular monolayers and films. A panel

      report for the materials sciences division of the department of energy. *Langmuir*

      1987, *3* (6), 932-950.

16.   Yamamoto, Y.; Nishihara, H.; Aramaki, K., Self-Assembled Layers of Alkanethiols

on Copper for Protection Against Corrosion. *Journal of the Electrochemical*

Society **1993,** *140* (2), 436-443.

Chapter 2
Theoretical Background

The following chapter provides the theoretical background for techniques and topics that are needed for further understanding of results acquired. While second harmonic generation and electrochemistry are useful techniques alone, the ability to use both simultaneously allows samples to be studied in-situ. Each technique reveals different information about the solid-liquid interfaces that are probed. The types of information given are further explained in the following sections.

2.1 Second Harmonic Generation

Second harmonic generation (SHG) is a surface specific, second-order, nonlinear optical process.[1-3] This technique provides information about the surface symmetry and the surface coverage.[2, 3]
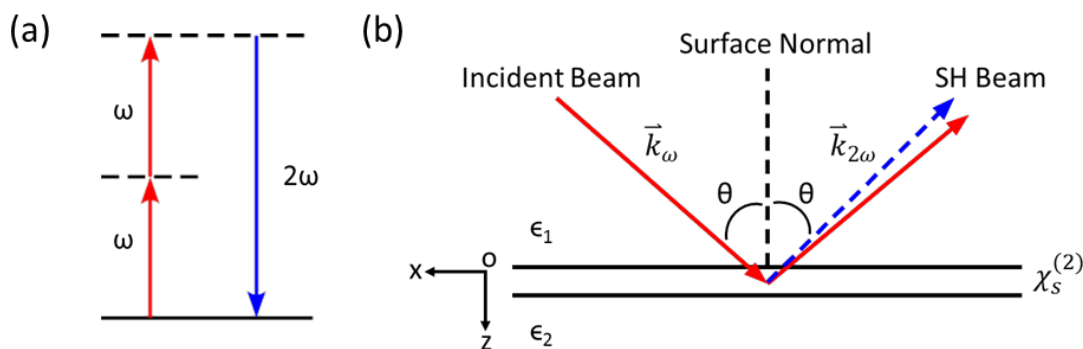
Figure 2.1 (a) Energy level diagram for the generation of the SH. **(b)** Schematic of the generation of the SH from a flat surface, where $\vec{k}_\omega$ and $\vec{k}_{2\omega}$ represents the momentum vectors of the incident and SH beam, respectively; ϵ_1 and ϵ_2 represents the permittivity of medium 1 and medium 2, respectively; $\chi_s^{(2)}$ represents the second order susceptibility; and θ represents the angle of incidence and reflection.

The general mechanism for the generation of the second harmonic (SH) is shown in Figure 2.1 (a), where two photons of frequency ω interact with the material medium and generate a photon of twice the frequency, 2ω. Figure 2.1 (b) shows how the SH is generated at an interface between two mediums.[4] A beam of frequency ω is incident on a material at an angle θ from the surface normal. This beam polarizes the material medium and that polarization acts as a source of polarization for the SH beam, which reflects off the surface at an angle θ. When the refractive index of the incident medium is the same for frequencies ω and 2ω, the angle of incidence and the angle of reflection are equal due to the conservation of momentum:

$$\vec{k}_\omega + \vec{k}_\omega = \vec{k}_{2\omega} \qquad [2.1]$$

$$\omega_1 n_1 \, sin(\theta_1) + \omega_1 n_1 \, sin(\theta_1) = \omega_2 n_2 \, sin(\theta_2) \qquad [2.2]$$

where $\vec{k}_\omega$ and $\vec{k}_{2\omega}$ are the wave vectors for the incident and SH beam respectively, and ω, n, and θ correspond to the frequency, refractive index, and angle from the surface normal for (1) the incident and (2) the SH beam.[5, 6] The polarization induced at the surface is expressed as a power series of electric field. Since the SH is a second order process, the polarization term of interest shown in Equation 2.4 is a product of the second order susceptibility and the square of the electric field.[1, 7, 8]

$$P = \varepsilon_0(\chi^{(1)} \cdot E + \chi^{(2)} : E^2 + \chi^{(3)} : E^3 + \cdots) \qquad [2.3]$$

$$P^{(2)} = \varepsilon_0 \chi^{(2)} : EE \qquad [2.4]$$

The second order susceptibility is a property of the material.[5] The susceptibility is made up of different components that correspond to a set of Cartesian coordinates, ijk, which is shown in Equation 2.5.[3, 4, 8] The components of the second order susceptibility, χ_{ijk}, are accessed by changing the polarization combination of the incident and the SH beam, where i corresponds to the SH field's polarization and j, k are degenerate due to the one input field. Four different polarization combinations are allowed: pp, ss, ps, and sp, where p refers to polarized light parallel to the incidence plane and s refers to polarized light perpendicular to the incidence plane.

$$P_i^{(2)} = \varepsilon_0 \sum_{jk} \chi_{ijk}^{(2)} E_j(\omega) \, E_k(\omega) \qquad [2.5]$$

The intensity of the SH signal is proportional to the square of the second order polarization shown in Equation 2.6.

$$I(2\omega) \propto \left| P^{(2)} \right|^2 \qquad [2.6]$$

As stated earlier, SHG is surface specific. This is proven by the fact that this second order process is only allowed at the interface, where the inversion symmetry is broken.[7] Under inversion, the relationship from Equation 2.4 becomes:

$$-P^{(2)} = \varepsilon_0 \chi^{(2)} : (-E)(-E) \qquad [2.7]$$

where $P^{(2)} = -P^{(2)}$, which is true only if $\chi_s^{(2)} = 0$. Therefore, at an interface, the inversion symmetry is broken and rise to the SH is allowed.

More specifically, interfacial second harmonic generation is sensitive to the electronic and structural properties of metals. At interfaces between two mediums, as shown in Figure 2.1 (b), there exist variances in matter, fields, and properties. For instance, the change in susceptibility across the interface, $\chi_0^{(n)} \rightarrow \chi_s^{(n)} \rightarrow \chi_2^{(n)}$. The effective second-order surface polarization encompasses several contributions shown in Equation 2.8.[3, 4, 9, 10]

$$P_{\text{s, eff}}^{(2)} = \alpha[E(\omega) \cdot \nabla E(\omega)] + \beta E(\omega)[\nabla \cdot E(\omega)] \qquad [2.8]$$

$$+ \left(\frac{2i\omega}{c}\right)\gamma[E(\omega) \times B(\omega)]$$

$$+ \chi_s^{(2)}\delta(z) : E(\omega)E(\omega)$$

The first two terms correspond to the electric quadrupole, where E is the electric field shown as a function of frequency, ω. The third term represents the magnetic dipole, B, as a function of frequency. The last term represents the electric dipole contributions. The coefficients α, β, and γ are defined in Equation 2.9, 2.10, and 2.11, respectively, where $\omega_p = (4\pi n e^2/m)^{1/2}$ is the plasma frequency of the conduction electrons, n is the density with a discontinuity at the surface of the metal, e and m are the charge and mass of an electron, and c is the speed of light.[11-14]

$$\alpha = \frac{ie^3 n}{4m^2 c\omega^3} \qquad [2.9]$$

$$\beta = \frac{e^3 n}{m^2 \omega_p^2 \omega^3} = \frac{e}{8\pi m\omega^2} \qquad [2.10]$$

11

$$\gamma = \frac{n_0 e^3}{8m^2 \omega^4} \qquad [2.11]$$

With the delta distribution, $\delta(z)$, $z = 0^+$, the nonlinear electric dipole interaction is restricted to the surface. For a metal, the surface polarization is restricted to the electric dipole contribution. Under the electric dipole approximation, the intensity of the SH is expressed in Equation 2.12, where ω and 2ω represent the frequency of the fundamental and SH electric fields, respectively.

$$I^{2\omega} = \frac{32\pi^3 \omega^2 \sec^2 \theta_0^{2\omega}}{c^3 \varepsilon_1(\omega)\varepsilon_1^{1/2}(2\omega)} \left| e^{2\omega} \cdot \chi^{(2)} : e^\omega e^\omega \right|^2 I^2(\omega) \qquad [2.12]$$

From the metal-liquid interface, SHG provides information about the surface symmetry and surface coverage of the metal. Second harmonic rotational anisotropy reveals the surface structure of metals. Using electrochemistry simultaneously with SHG offers an in-situ explanation of the surface properties while applying an external potential. With these complimentary techniques, surface coverage from the adsorption of an adlayer onto a metal surface through underpotential deposition can be observed as well as the reductive desorption of self-assembled monolayers at negative potentials. These applications of second harmonic generation will be expanded upon in later sections.

2.1.1 Second Order Nonlinear Susceptibility

As stated above, the second order susceptibility, $\chi^{(2)}$, is a property of the material being studied. By probing certain components of the third-rank tensor, information about the surface is acquired. To identify the tensor elements contributing to the signal, it is important to understand how the components of the second order susceptibility, χ_{ijk}, are accessed by changing the polarization, but first, a more general case is discussed where the nonlinear susceptibility is related to the complex amplitudes of electric field and polarization.

The electric field vector of an optical wave can be expressed by the sum of a number of frequency components, shown in Equation 2.13. The field amplitude, A_n, is defined in relation to the electric field by Equation 2.14.

$$\tilde{E}(r,t) = \sum_n' \tilde{E}_n(r,t) \qquad [2.13]$$

$$E_n(r) = A_n e^{ik_n \cdot r} \qquad [2.14]$$

The total electric field is then represented in terms of field amplitudes by the following expressions.

$$\tilde{E}(r,t) = \sum_n' E_n(r)e^{-i\omega_n t} + c.c. \qquad [2.15]$$

$$\tilde{E}(r,t) = \sum_n' A_n e^{i(k_n \cdot r - \omega_n t)} + c.c. \qquad [2.16]$$

The field amplitudes can also be conveyed using an alternative notation with respect to the frequency component, ω_n.[8, 15]

$$E_n = E(\omega_n) \text{ and } A_n = A(\omega_n)$$ [2.17]

With the different notation, the total field can be written in a more compact form.

$$\tilde{E}(r,t) = \sum_n E(\omega_n)e^{-i\omega_n t}$$ [2.18]

$$\tilde{E}(r,t) = \sum_n A(\omega_n)e^{i(k_n \cdot r - \omega_n t)}$$ [2.19]

According to the definition of field amplitude, the electric field given by the following equation:

$$\tilde{E}(r,t) = \mathcal{E}\cos(k \cdot r - \omega t)$$ [2.20]

is also represented by the complex field amplitudes in Equation 2.21 or by the slowly varying amplitudes in Equation 2.22.

$$E(\omega) = \frac{1}{2}\mathcal{E}e^{ik \cdot r}, \qquad E(-\omega) = \frac{1}{2}\mathcal{E}e^{-ik \cdot r}$$ [2.21]

$$A(\omega) = \frac{1}{2}\mathcal{E}, \qquad A(-\omega) = \frac{1}{2}\mathcal{E}$$ [2.22]

In both of the above representations, factors of ½ appear because the physical field amplitude $\mathcal{E}$ has been divided equally between the positive and negative frequency components.

14

The nonlinear polarization can be expressed in a similar notation, shown below.

$$\tilde{P}(r,t) = \sum_n P(\omega_n)e^{-i\omega_n t} \qquad\qquad [2.23]$$

Now, the components of the second-order susceptibility tensor $\chi_{ijk}^{(2)}(\omega_n + \omega_m, \omega_n, \omega_m)$ are defined as the constants of proportionality relating the amplitude of the nonlinear polarization to the product of field amplitudes. This is represented in Equation 2.24, where the subscripts n and m refer to the two incident electric fields and the notation ijk correspond to a set of Cartesian coordinates.

$$P_i(\omega_n + \omega_m)^{(2)} = \sum_{jk} \sum_{nm} \chi_{ijk}^{(2)}(\omega_n + \omega_m, \omega_n, \omega_m) E_j(\omega_n) E_k(\omega_m) \qquad [2.24]$$

From the above equation, the tensor element can have many forms. With ijk taking the values of x, y, and z, there alone are 27 Cartesian components. Therefore, there are 27 components for each possible frequency combination. With 12 possible frequency combinations, there are as many as 324 different values that describe the interaction. Fortunately, symmetry places restrictions on various components of the tensor, $\chi^{(2)}$, which limits the amount of values that actually contribute to polarization.

Since j, k, n, and m are dummy indices, the contribution to the nonlinear polarization shown by the product in Equation 2.24 can also be represented by interchanging k with j and by interchanging n with m. This is expressed below in Equation 2.25. This is known as intrinsic permutation symmetry, where the below expression holds true if it is required that the nonlinear susceptibility remains unchanged by the

simultaneous interchange of the two incident frequency arguments and the last two Cartesian components.

$$\chi_{ijk}^{(2)}(\omega_n + \omega_m, \omega_n, \omega_m) = \chi_{ikj}^{(2)}(\omega_n + \omega_m, \omega_m, \omega_n) \qquad [2.25]$$

For the case of a lossless nonlinear medium, there are two additional symmetry restrictions on the nonlinear susceptibility tensor. Firstly, all the components of $\chi_{ijk}^{(2)}(\omega_n + \omega_m, \omega_n, \omega_m)$ are real.[8, 15] This indicates that an electric field induces a polarization that is in phase with the susceptibility and that the polarization response to the incident field is instantaneous.[8, 15] The dependence of χ on field strength is shown in Equation 2.3. Secondly, full permutation symmetry is allowed. This condition states that all frequency elements of the nonlinear susceptibility can be freely interchanged as long as the corresponding Cartesian coordinates are interchanged simultaneously.[8, 15] This argument includes the first term, which is the sum of the latter two terms, thus the signs of the frequency must be inverted when the first frequency is replaced with either of the latter two. An example is shown below.

$$\chi_{ijk}^{(2)}(\omega_3 = \omega_1 + \omega_2) = \chi_{jki}^{(2)}(\omega_1 = -\omega_2 + \omega_3) \qquad [2.26]$$

Whenever dispersion of the susceptibility can be neglected, Kleinman symmetry is valid. This assumes that the nonlinear susceptibility does not depend on frequency and hence the indices may be permuted without permuting the frequencies. An example is shown in Equation 2.27.

$$\chi_{ijk}^{(2)}(\omega_3 = \omega_1 + \omega_2) = \chi_{jki}^{(2)}(\omega_3 = \omega_1 + \omega_2) \qquad [2.27]$$

Within the Kleinman symmetry condition and in SHG, χ is symmetric in the last two indices since ω_n and ω_m are equal. This allows for a contracted notation given below in Table 2.1.

Table 2.1 Contracted notation where the indices j and k are identical.

j, k	11	22	33	23, 32	31, 13	12, 21
l	1	2	3	4	5	6

The contracted notation can then be used to represent the nonlinear susceptibility in a simpler matrix. This gives a 3 × 6 matrix referred to as the d-matrix.

$$d_{il} = \begin{pmatrix} d_{11} & d_{12} & d_{13} & d_{14} & d_{15} & d_{16} \\ d_{21} & d_{22} & d_{23} & d_{24} & d_{25} & d_{26} \\ d_{31} & d_{32} & d_{33} & d_{34} & d_{35} & d_{36} \end{pmatrix} \qquad [2.28]$$

By introducing the Kleinman symmetry condition, not all 18 elements of the d-matrix are independent given that the indices of d_{ijk} can be freely permuted. An example is shown below.

$$d_{12} = d_{122} = d_{212} = d_{26} \qquad [2.29]$$

This gives a d-matrix with only 10 independent elements.

$$d_{il} = \begin{pmatrix} d_{11} & d_{12} & d_{13} & d_{14} & d_{15} & d_{16} \\ d_{16} & d_{22} & d_{23} & d_{24} & d_{14} & d_{12} \\ d_{15} & d_{24} & d_{33} & d_{23} & d_{13} & d_{14} \end{pmatrix} \qquad [2.30]$$

17

Second harmonic generation nonlinear polarization can be described by the following matrix equation.

$$
\begin{pmatrix} P_x(2\omega) \\ P_y(2\omega) \\ P_z(2\omega) \end{pmatrix} = 2 \begin{pmatrix} d_{11} & d_{12} & d_{13} & d_{14} & d_{15} & d_{16} \\ d_{21} & d_{22} & d_{23} & d_{24} & d_{25} & d_{26} \\ d_{31} & d_{32} & d_{33} & d_{34} & d_{35} & d_{36} \end{pmatrix} \times \begin{pmatrix} E_x(\omega)^2 \\ E_y(\omega)^2 \\ E_z(\omega)^2 \\ 2E_y(\omega)E_z(\omega) \\ 2E_x(\omega)E_z(\omega) \\ 2E_x(\omega)E_y(\omega) \end{pmatrix} \qquad [2.31]
$$

Furthermore, the 10 independent tensor elements are further eliminated by the specific symmetry of the sample studied. By applying symmetry elements, for example, inversion symmetry, equivalent and vanishing tensor are identified. The specific susceptibility tensor elements giving rise to second harmonic signal are identified through these transformations.

2.1.2 Rotational Anisotropy

Second harmonic rotational anisotropy allows the isotropic and anisotropic sources of a surface to be studied. By rotating a sample about the surface normal, the modulation in SH intensity is monitored. With the SH anisotropy, the rotational symmetry of a surface can be further examined as the surface experiences changes over the course of an experiment. SH rotational anisotropy has been employed to study many systems. A few of the more popular are the crystallinity of metal single crystals as well as the symmetry of metal-liquid interfaces at applied potentials. Furthermore, by applying the

four different polarization combinations, the SH signal is connected to specific symmetry properties of the nonlinear susceptibility tensor.[3]

An example of rotational anisotropy is given below in Figure 2.2. Copper is a metal of interest in both academia and industry due to its high thermal and electrical conductivities and low cost.[16] Considering only the top layer of copper compacted atoms, the Cu(111) surface is suspected to have six-fold symmetry, but if the top two layers are considered, the Cu(111) surface will show a three-fold symmetry.[17-19] The different symmetries from the Cu(111) surface are displayed in Figure 2.2 for all four polarization combinations: pp, ps, sp, and ss. Figure 2.2 (b), (c), and (d) show a six-fold symmetry, while (a) shows a three-fold symmetry.
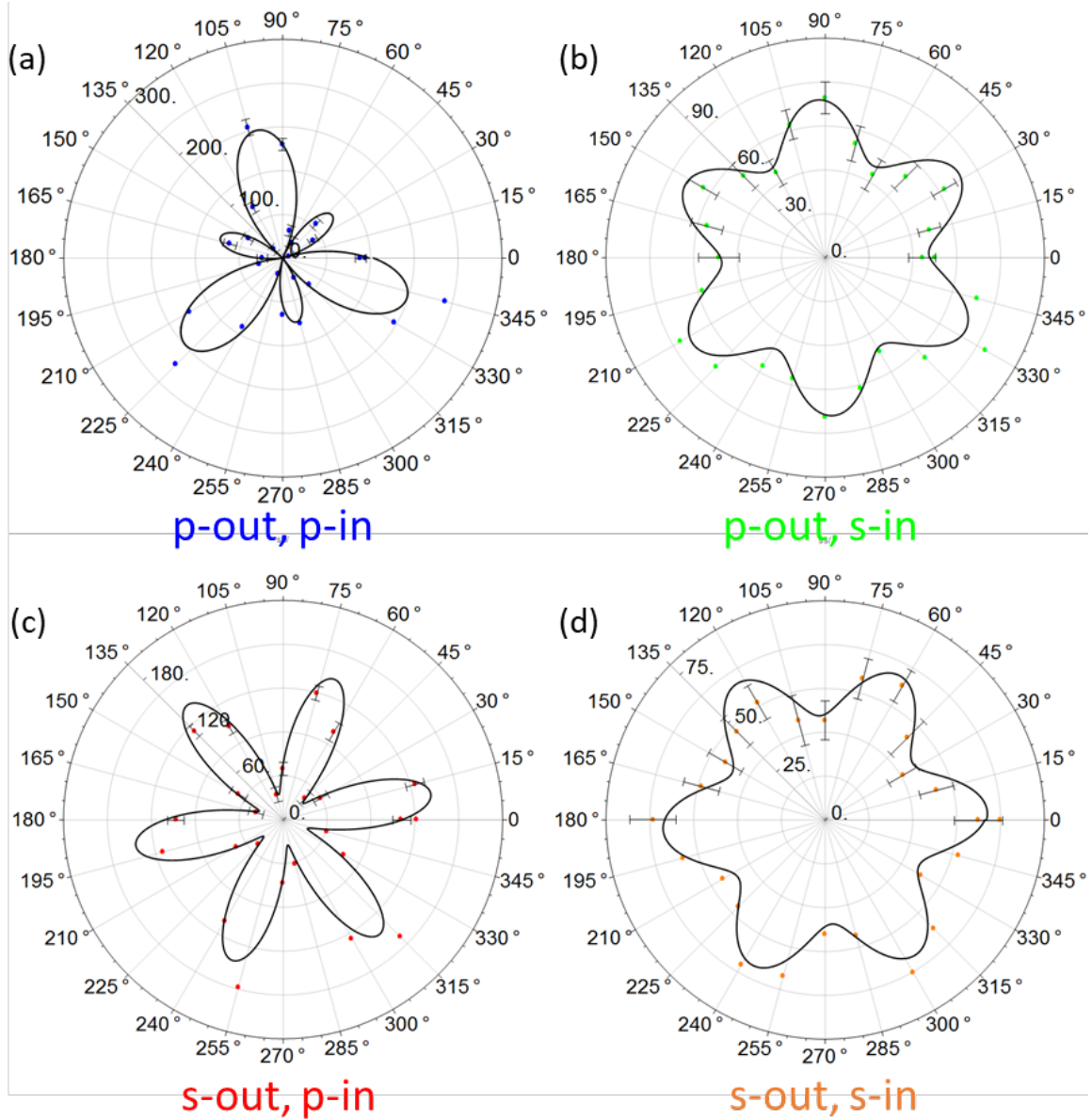
Figure 2.2 Polar plots for Cu(111) for the different polarization combinations **(a)** p-out, p-in; **(b)** p-out, s-in; **(c)** s-out, p-in; **(d)** s-out, s-in.

The polar plots are fitted with a non-linear model function on Wolfram Mathematica. For ps, sp, and ss polarizations, the fit equation is shown in Equation 2.32. For the pp polarization, a three-fold symmetry was shown and the fit Equation 2.33 was used. Both equations are shown as a function of azimuthal angle, φ.

$$f(\varphi) = a + b \times \cos[c \times \varphi + d] \qquad\qquad [2.32]$$

$$f(\varphi) = \sqrt{(a + b \times \cos[c \times \varphi + d])^2 + e^2} \qquad [2.33]$$

The variables a and b correspond to the isotropic and anisotropic contributions to the symmetry. The symmetry order is represented by c. The variable d is a phase correction with respect to φ. In Equation 2.33, e accounts for incoherent background. Table 2.2 shows the fitting parameters for each polarization combination.

Table 2.2 Fitting parameters for polar plots of Cu(111) for all four polarization combinations.

	pp	sp	ss	ps
a	44.5	79.9	48.7	59.6
b	134.1	56.5	10.6	12.4
c	3	6	6	6
d	7.3	1.1	0.3	9.2
e	5.8×10^{-6}	0	0	0

2.1.3 Surface Coverage

The adsorption of adlayers of metals, molecules, ions at an interface changes surface properties.[3] The change can be monitored by the SH response to the surface. One of the first examples of a change in SH due to adsorption was by Heinz on a Rh(111) surface. For the adsorption of O_2 and CO_2, a decrease in the SH was observed, however, for the adsorption of Na, an increase in the SH was detected.[20] The SH increased because Na donated an electron to Rh. These results revealed the sensitivity of the SH to different chemical reactions occurring at the surface. Another advantage to using SHG to monitor

the surface coverage is the ability to study systems in-situ. This allows for reactions at interfaces to be monitored in real-time.

2.2 Interfacial Electrochemistry

Interfacial electrochemistry is the study of processes at the interface between an electronic and ionic conductor, an electrode and electrolyte. More specifically, an interface is the region between two adjacent phases whose properties differ considerably from those of the bulk. An electrode surface can be electrochemically modified by adsorbates and produce a differing and more complicated structure. These surfaces have applications in many fields, such as electrocatalysis, corrosion inhibition, and electronics.

The system of focus for the experiments in the following chapters involves the interface between a metal and an electrolyte. At this metal-solution interface, there are different types of interactions that occur. An overview of these interactions are shown in Figure 2.3 below. In the figure, the grey circles represent a metal surface and the white circles represent the solution. The metal surface can take various forms depending on the lattice structure. Amongst the solution molecules are circles with a dipole moment and ions represented by a charge. These additional elements represent possible interactions that may occur at the surface. One example is the adsorption of a cation on a top site of the metal surface. The adsorption site is dependent on many factors including the metal structure. Another reaction that can occur at the surface is the deposition of a metal. This is shown at the bottom of Figure 2.3. Both ion and electron transfer reactions involve charge transfer across the interface. This charge transfer is measured as electric current.
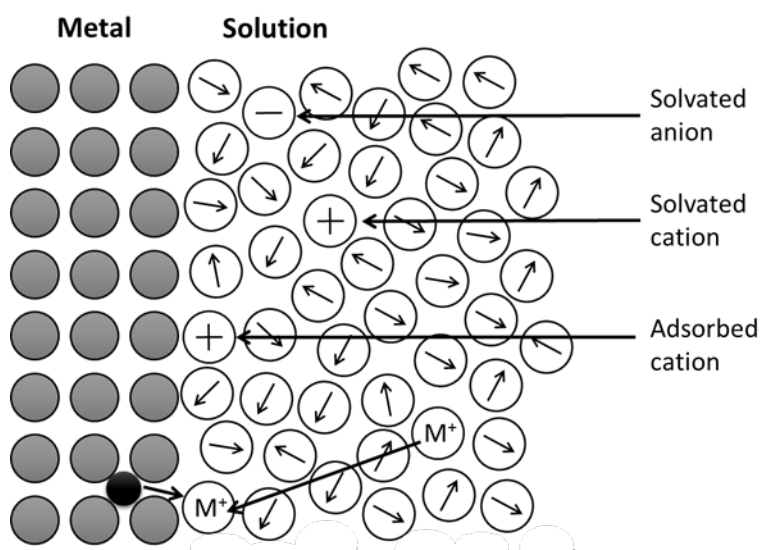
Figure 2.3 Example of processes at the metal-solution interface. Grey circles represent the metal, white circles represent the solution, circles with charges are cations or anions, respectively, and black circles represent electrons.

A three electrode system is employed to carry out electrochemistry experiments. The three electrodes are a working, counter, and reference electrode. They are connected via a potentiostat and assembled in a electrochemical cell. The working electrode (WE) is the electrode used to investigate electrochemical phenomena. The applied potential is controlled at this electrode and must be well taken care of in regards to cleanliness and surface quality. The counter electrode's (CE) function is to allow current to be passed through the cell. The reference electrode (RE) has a set potential, which provides a reference in regards to the applied potential at the working electrode. An electrolyte is used to ensure good electric conductivity.

2.2.1 Cyclic Voltammetry

One electrochemical technique employed by a potentiostat is cyclic voltammetry (CV). A current potential plot, referred to as a cyclic voltammogram trace, is produced by cycling between a specific applied potential range for a specified number of cycles and recording the current response at the WE. The applied potential extents are usually limited by the solution oxidation and reduction. The applied potential at the WE is measured against the RE, which maintains a constant potential via a redox process (e.g. Ag/AgCl). CV can be used to ascertain information about chemical reactions that occur at an interface. It can be used to study the adsorption of molecules, the presence of intermediates in oxidation-reduction reactions, and the reversibility of a reaction. For the purpose of the experiments in the following chapters, CV is used for the underpotential deposition of copper on to a gold evaporated film and to reductively desorb *n*-alkanethiol monolayers from an electrode.
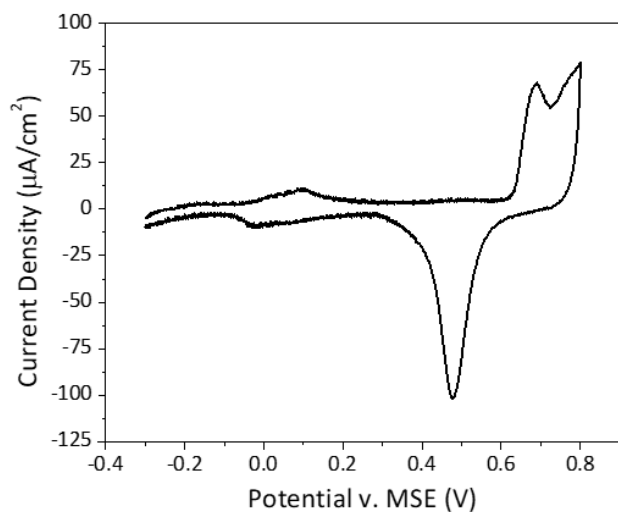
Figure 2.4 Cyclic voltammogram trace of gold in 0.1M H_2SO_4. Scan Rate: 50 mV/s

A sample cyclic voltammogram trace is shown in Figure 2.4. The potential range is chosen from -0.3 to 0.8 V. This range shows the oxidation and reduction of gold in 0.1M H_2SO_4. The anodic curve runs from -0.3 to 0.8 V and shows features corresponding to the oxidation of gold. The cathodic curve runs from 0.8 to -0.3 V and shows a peak corresponding to the reduction of gold.

2.2.2 Underpotential Deposition

Underpotential deposition (UPD) is the phenomena of the electrodeposition of a metal adlayer onto a dissimilar metal.[3, 21-24] This deposition occurs at a potential positive to the thermodynamically reversible potential for the deposition of a metal ion onto a substrate of the corresponding metal. Therefore, UPD is understood to be when a metal ion more readily deposits onto a substrate differing from itself. Generally, UPD is used to deposit sub-to-monolayer films onto a metal substrate.
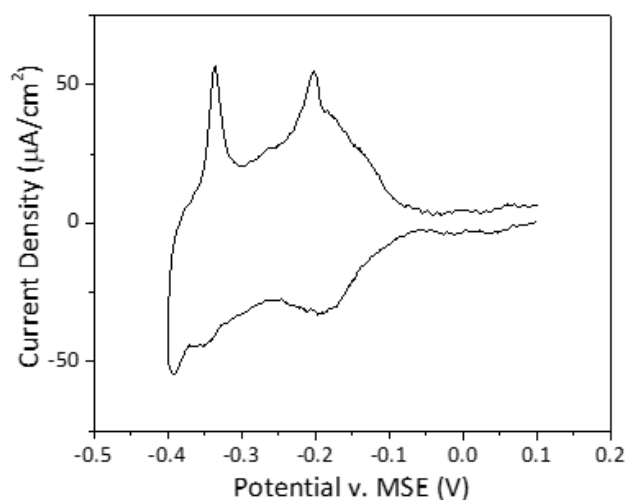
Figure 2.5 Underpotential deposition of copper onto a gold electrode. Cyclic voltammogram trace of gold in 1mM $CuSO_4 \cdot 5H_2O$ and 0.1M H_2SO_4. Scan Rate: 20 mV/s

25

Figure 2.5 shows a cyclic voltammogram trace of a gold electrode in 1mM CuSO$_4 \cdot$5H$_2$0 and 0.1M H$_2$SO$_4$. This represented the underpotential deposition of copper onto the gold WE. The peaks corresponding to the deposition are shown in the cathodic scan from 0.1 to -0.4 V. When the potential is reversed, the two peaks in the anodic scan correspond to the stripping of the copper from the gold WE. This points to a reversible process.

2.3 References

1. Eisenthal, K. B., Liquid Interfaces Probed by Second-Harmonic and Sum-Frequency Spectroscopy. *Chemical Reviews* **1996,** *96* (4), 1343-1360.

2. Corn, R. M.; Higgins, D. A., Optical second harmonic generation as a probe of surface chemistry. *Chemical Reviews* **1994,** *94* (1), 107-125.

3. Pettinger, B. B., C.; Lipkowski, J.; Schmickler, W. , Second Harmonic Generation Anisotropy from Single Crystalline Electrode Surfaces. In *Interfacial electrochemistry: theory: experiment, and applications*, Routledge: 1999; pp 373-404.

4. Richmond, G. L.; Robinson, J. M.; Shannon, V. L., Second harmonic generation studies of interfacial structure and dynamics. *Progress in Surface Science* **1988,** *28* (1), 1-70.

5. Bloembergen, N.; Pershan, P., Light waves at the boundary of nonlinear media. *Physical Review* **1962,** *128* (2), 606.

6. Wang*, H.-F.; Gan†‡, W.; Lu†‡ §, R.; Rao†‡¶, Y.; Wu†, B.-H., Quantitative spectral and orientational analysis in surface sum frequency generation vibrational spectroscopy (SFG-VS). *International Reviews in Physical Chemistry* **2005,** *24* (2), 191-256.

7. Shen, Y. R., Surface properties probed by second-harmonic and sum-frequency generation. *Nature* **1989,** *337*, 519.

8. Boyd, R. W., *Nonlinear optics*. Elsevier: 2003.

9.   Bloembergen, N.; Pershan, P. S., Light Waves at the Boundary of Nonlinear Media. *Physical Review* **1962,** *128* (2), 606-622.

10.   Shen, Y.-R., The principles of nonlinear optics. *New York, Wiley-Interscience, 1984, 575 p.* **1984**.

11.   Jha, S. S., Nonlinear Optical Reflection from a Metal Surface. *Physical Review Letters* **1965,** *15* (9), 412-414.

12.   Jha, S. S., Theory of Optical Harmonic Generation at a Metal Surface. *Physical Review* **1965,** *140* (6A), A2020-A2030.

13.   Jha, S. S.; Warke, C. S., Interband Contributions to Optical Harmonic Generation at a Metal Surface. *Physical Review* **1967,** *153* (3), 751-759.

14.   Bloembergen, N.; Chang, R. K.; Jha, S. S.; Lee, C. H., Optical Second-Harmonic Generation in Reflection from Media with Inversion Symmetry. *Physical Review* **1968,** *174* (3), 813-822.

15.   Powers, P. E., *Fundamentals of Nonlinear Optics*. CRC Press: Boca Rotan, 2011.

16.   Jennings, G. K.; Munro, J. C.; Yong, T.-H.; Laibinis, P. E., Effect of Chain Length on the Protection of Copper by n-Alkanethiols. *Langmuir* **1998,** *14* (21), 6130-6139.

17.   Sipe, J. E.; Moss, D. J.; van Driel, H. M., Phenomenological theory of optical second- and third-harmonic generation from cubic centrosymmetric crystals. *Physical Review B* **1987,** *35* (3), 1129-1141.

18.   Shannon, V. L.; Koos, D. A.; Kellar, S. A.; Huifang, P.; Richmond, G. L., Rotational anisotropy in the second harmonic response from copper(111) in aqueous solutions. *The Journal of Physical Chemistry* **1989,** *93* (17), 6434-6440.

19.   Tom, H. W. K.; Aumiller, G. D., Observation of rotational anisotropy in the second-harmonic generation from a metal surface. *Physical Review B* **1986,** *33* (12), 8818-8821.

20.   Tom, H. W. K.; Mate, C. M.; Zhu, X. D.; Crowell, J. E.; Heinz, T. F.; Somorjai, G. A.; Shen, Y. R., Surface Studies by Optical Second-Harmonic Generation: The Adsorption of ${\mathrm{O}}_{2}$, CO, and Sodium on the Rh(111) Surface. *Physical Review Letters* **1984,** *52* (5), 348-351.

21.   Bard, A. J.; Faulkner, L. R.; Leddy, J.; Zoski, C. G., *Electrochemical methods: fundamentals and applications*. wiley New York: 1980; Vol. 2.

22.   Jennings, G. K.; Laibinis, P. E., Self-Assembled n-Alkanethiolate Monolayers on Underpotentially Deposited Adlayers of Silver and Copper on Gold. *Journal of the American Chemical Society* **1997,** *119* (22), 5208-5214.

23.   Herrero, E.; Buller, L. J.; Abruña, H. D., Underpotential Deposition at Single Crystal Surfaces of Au, Pt, Ag and Other Materials. *Chemical Reviews* **2001,** *101* (7), 1897-1930.

24.   Bockris, J. O. M.; Reddy, A. K.; Gamboa-Aldeco, M., *Modern Electrochemistry: Fundamentals of Electrodics. V. 2a*. Plenum Press: 1998.

Chapter 3
Experimental Design and Procedure

The following chapter outlines all experimental procedures from optical components, sample preparation, and electrochemistry. The first focus is on the alignment and optimization of the Ti:sapphire oscillator, which produces a femtosecond pulse that is then used in second harmonic experiments. After pulse characterization, an optical system was designed and assembled to generate the second harmonic for rotational anisotropy and in-situ electrochemical experiments. With this specific optical design, specialized cell designs were designed and constructed to probe solid-liquid interfaces in conjunction with electrochemistry. Lastly, experimental parameters are outlined.

3.1 Ti:sapphire Oscillator

To generate the second harmonic (SH), short pulses are needed for their high peak powers to drive the second-order nonlinear response.[1] A Ti:sapphire (Ti^{3+}:Al_2O_3) oscillator is used as the excitation source because the large gain bandwidth of Ti^{3+}:Al_2O_3 makes it an attractive medium for short pulse generation. This oscillator is optimal due to its high repetition rate and short pulse duration. The schematic of the oscillator is shown in Figure 3.1.
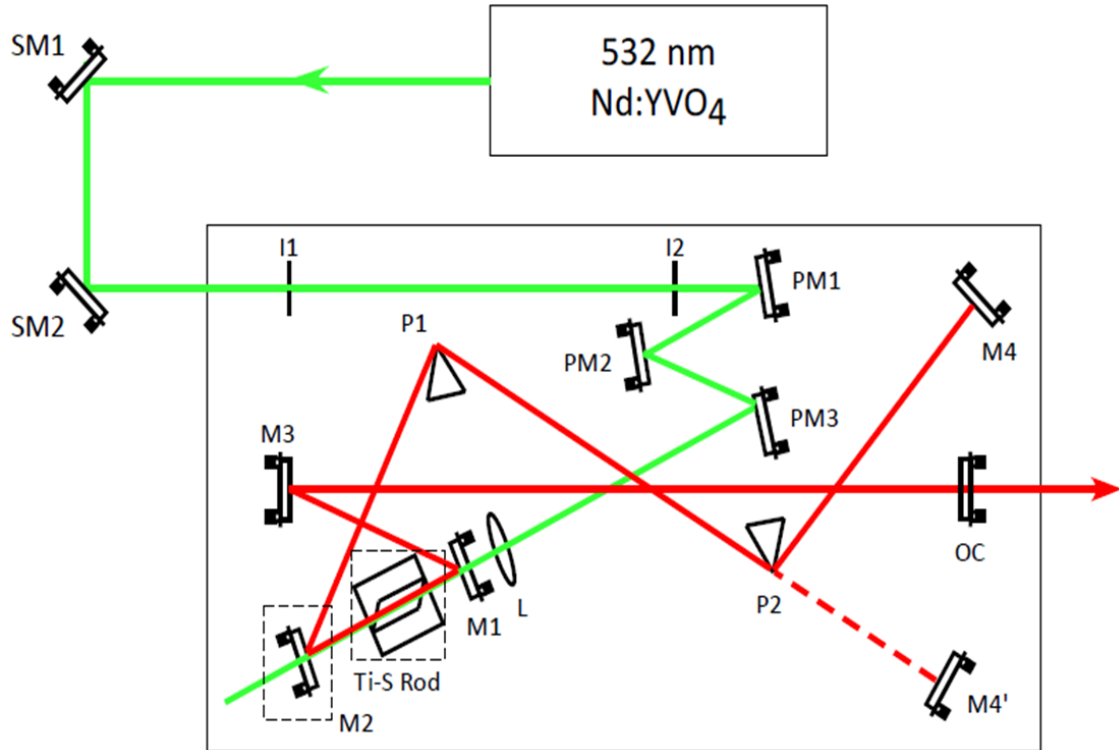
Figure 3.1 Schematic of the layout and optical components of the Ti:Sapphire oscillator where SM represents a steering mirror, PM represents a pumping mirror, M represents a mirror, P represents a prism, L represents a lens, and OC represents an output coupler.

A continuous wave (cw) 532 nm Nd:YVO$_4$ laser is used to pump the gain medium, the Ti:sapphire crystal rod. At the gain medium, the light is amplified by stimulated emission to produce lasing, by population inversion. The intensity of this beam then induces a change in the refractive index. Due to the non-uniform power density distribution in a Gaussian beam, the refractive index changes across the beam profile,[2] with the greatest index change occurring at the center of the beam. As the beam passes through the center of the Ti:sapphire rod, the change in refractive index leads to self-focusing and the creation of a Kerr lens. This process is referred to as the Kerr lensing effect.[2] This results in mode locking, which is initiated from a perturbation of any

intracavity optic. The mode locking in the oscillator is not self-starting but, after initiation, is self-sustaining. From a mode locked Ti:sapphire oscillator, the generation of femtosecond pulses for experimental use is achieved.

3.1.1 Start Up and Shut Down Procedure

The pump laser, a Sprout-H-7W, was purchased from Lighthouse Photonics. The laser system consists of a laser head and power supply-cooler. Before turning on the laser, a Neslab CFT-25 recirculating chiller was set to 20 ˚C and turned on to keep the Ti:sapphire crystal at a constant temperature without overheating. After five minutes of cooling, the key on the power supply-cooler of the laser was switched from standby to the on position. Next, the shutter was opened at the output of the laser head by centering the groove on the shutter wheel. To turn on the laser, the black control knob on the front of the power supply was pushed once. For aligning the Ti:sapphire, the laser has an idle mode where a low power output of about 10 mW is achieved by pushing the black knob once. To return to normal operation, the black knob was again pushed once, and finally to turn off the laser, the black knob was pushed twice. For complete shutdown, the laser was turned off, the shutter was closed, and the key was returned to the standby position.

3.1.2 Alignment Procedure

For aligning the Ti:Sapphire oscillator, the laser was used in the idle function. The following steps were taken for alignment of the oscillator. Reference Figure 3.1 for optic identification.

1. The steering mirrors (SM1 and SM2) were used to align the beam through the center of the iris's (I1 and I2) in a corresponding manner. Using SM1 for I1 and SM2 for I2, the beam was continually centered through the iris until no change was observed between the two.

2. The lens (L) and mirror (M1) were removed from the oscillator.

3. A floating iris set to the desired height was used to ensure that the height of the green beam was level after each pump mirror (PM1, PM2, and PM3) and throughout the entire cavity.

4. Using the floating iris, the green beam's height was checked before and after the Ti:Sapphire rod. The knobs on the translational stage that the rod is mounted on adjusted the left and right position of the rod to center the position that the beam hits the Ti:sapphire rod. For optimal alignment, the beam passed through the rod with maximum transmission and minimal reflection.

5. M1 was reinserted into the cavity making sure the position of the green beam does not change before and after the Ti:Sapphire rod. Using the floating iris, the back reflection from M1 was aligned so that the back reflection was aligned with the input beam. This ensured the beam path through the mirror was not only centered but also perpendicular to the optic.

6. The lens (L) was then placed into the cavity. The height of the lens was manually set to assure the height of the back reflections was consistent with that of the green beam throughout the oscillator. This was examined with the floating iris.

7. The back reflections from M2 were checked using the floating iris. If alignment up to this point was correct, the heights of both spots would be the same. However, if the back reflections are not aligned, then repeat all previous steps.

8. The height of the green beam before P1 and before P2 was checked with the floating iris. M2 was used to adjust the height of the beam hitting P1, while the P1 stage was used to adjust the height in front of P2.

9. After finishing all preliminary alignment, the laser was returned to normal operation mode and the power was set to 1.0 W.

10. P2 was moved out of the beam path. With a near infrared (IR) viewer, the fluorescence of the beam was checked, which can be seen in Figure 3.2 (b), (c), and (d). The floating iris was used for centering and aligning the fluorescence and its back reflection. The fluorescence travelled two paths. One path originated from the Ti:sapphire rod and M1. The florescence travels to M3 and was reflected toward the output coupler (OC). The red beam was centered on the OC using the mirror mount of M3, and the back reflection of the fluorescence from OC was centered back onto itself using the adjustment knobs on the OC. The second fluorescence path originated from the Ti:sapphire rod and M2. The beam is reflected towards P1 and then sent towards M4'. The stage of P1 was used to align the height of the red beam, and the mirror mount of M4' was used to align the back reflection of the fluorescence back onto itself.

11. After first alignment of fluorescence at low power, the laser power was set to 5.0

W to look for lasing. To achieve continuous wave (cw) lasing, the back reflection of the fluorescence from M4' and the OC must be perfectly reflected back onto itself. Until lasing is attained, the back reflections were continually checked and re-aligned by alternating the position of the floating iris between both beam paths at points close to the two optics contributing to the fluorescence and its beam path. These optics were identified in step 10.

12. When lasing is achieved, P2 was placed into the path of fluorescence to send the beam towards M4, which was equipped with slits. For ease, alignment was first acquired with the slits to M4 fully opened. Using the near IR viewer, the process for achieving cw lasing was repeated now using M4 instead of M4'.

13. After cw lasing was optimized, the slits to M4 were slowly closed down until a drop in power occurred. Power was once again optimized using the adjustment knobs on M4, and then again optimized by shifting the left and right position of the slits to center the beam by using the slits translational stage. This was a continual process of altering alignment and then re-optimizing power.

14. Once satisfied with the tilt of M4 and the position of the slits, the stage of P2 was quickly and gently tapped out of and back into the beam path to look for mode locking. The mode locked pulse can be monitored on either an oscilloscope with a photodetector or with a spectrometer.

3.1.3 Optimization of Ti:sapphire Oscillator

To obtain an optimum mode locked pulse, the tilt of M4 and the OC were adjusted. The position of the Ti:sapphire crystal between M1 and M2 also affected mode locking. Adjustments were made using the translational stages of both the Ti:sapphire crystal and M2. For a more stable mode locked pulse, the green beam was shifted towards the apex of P2. For a lower wavelength, the green beam was shifted towards the center of P2. If unable to find any mode locking, the Ti:sapphire rod was positioned closer to M1, however, power decreased, therefore it was about finding a balance between stability and power of the mode locked pulse. By adjusting the green beam towards the apex of P1, the wavelength decreased. These were a few observations made from working with the oscillator.
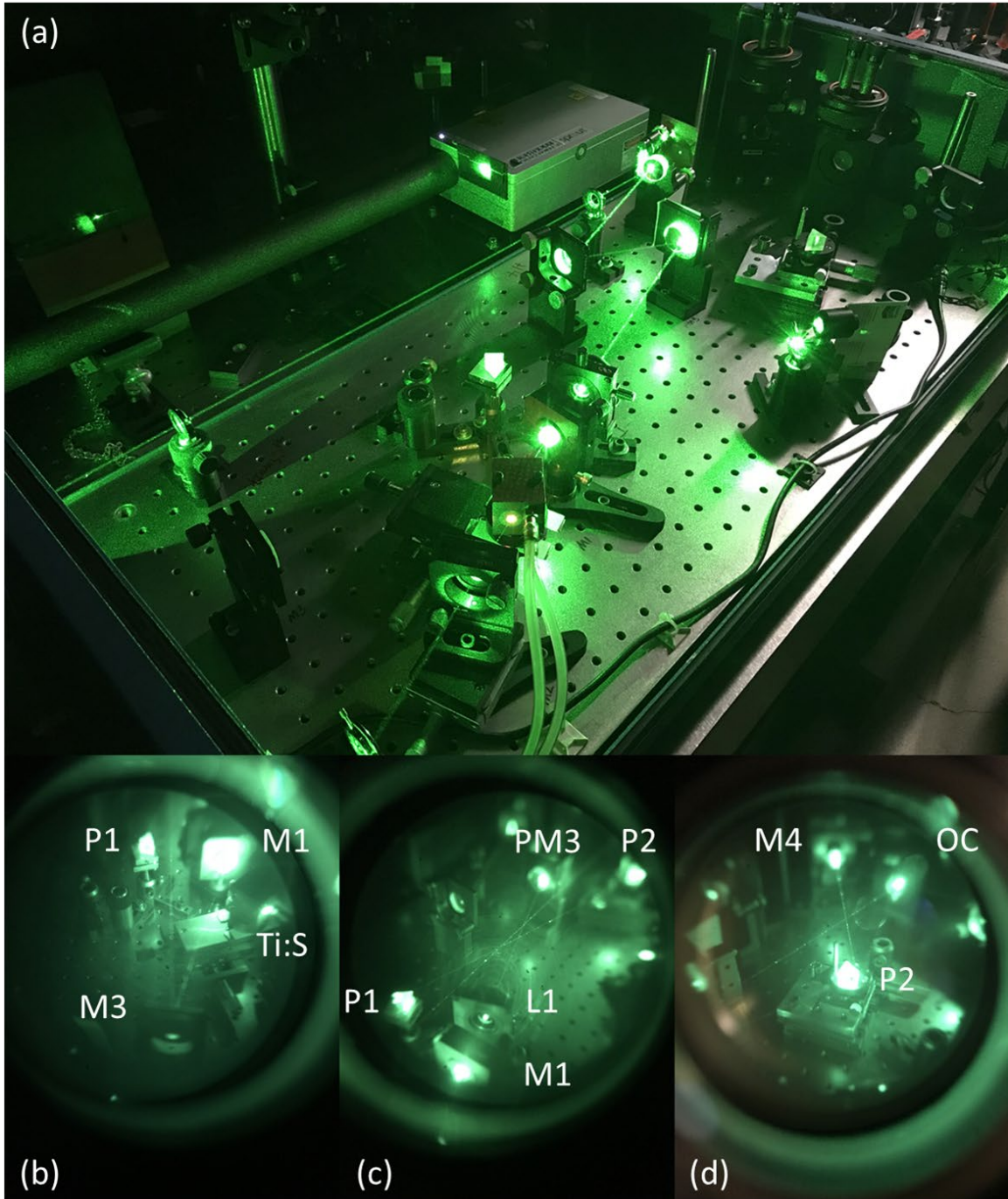
Figure 3.2 Photographs of the Ti:sapphire oscillator. **(a)** Image of the oscillator in its entirety. **(b)**, **(c)**, and **(d)** Images of lasing through an IR viewer from 3 different vantage points.

3.1.4 Cleaning Procedure for the Ti:sapphire Crystal

The Ti:sapphire crystal was wrapped in a thin layer of indium foil and then encased in a copper housing. The rod was cleaned at least once a year. To clean, the copper housing was first disassembled. If the indium foil was intact and seemed in good condition it was not replaced. If the indium foil was not smoothly enveloping the rod, a new layer layer was used to wrap the rod without overlapping. The two surfaces of the rod were cleaned with spectroscopic grade methanol with lens cleaning paper and cotton tipped applicators. Before being fully encased in the copper housing, the Ti:sapphire rod was set in the beam path in the idle mode. The positioning of the rod inside the copper housing was set by fixing all reflections from the crystal to the height of the floating iris. Once the rod positioning was set, the top of the copper housing was gently placed on top without shifting the rod's position. Holding the copper housing together, the housing was flipped upside and fastened together with its screws. The rod, now re-encased in the copper housing, was placed into the beam path and the oscillator was re-aligned using the steps given in *3.1.2*.

3.2 Autocorrelator

The mode locked pulses were monitored with a photodetector and oscilloscope on a nanosecond scale. However, the pulses were on an order of femtoseconds, and since no method was available to resolve the pulse, the pulse was measured against itself.[2] To use the pulse itself, an autocorrelator was constructed, shown in Figure 3.3 (a).
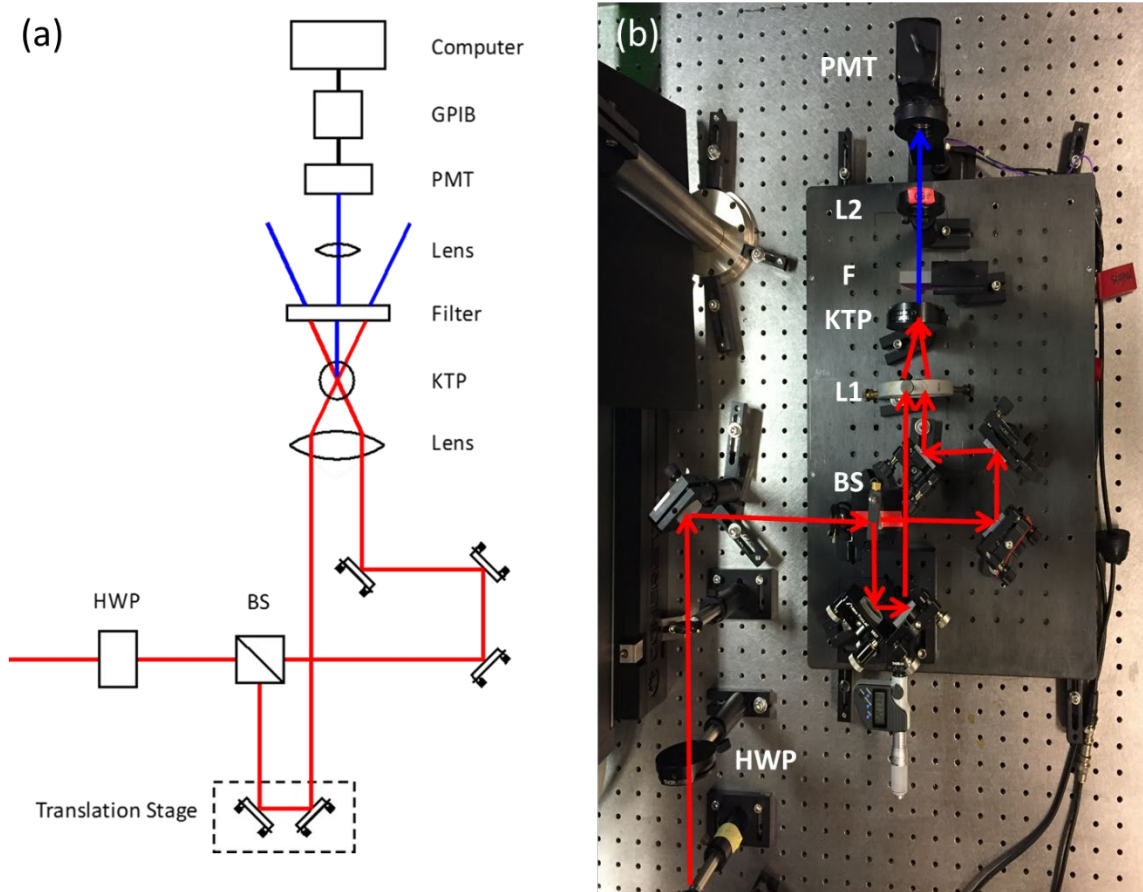
Figure 3.3 (a) Schematic of the layout and optical components for the autocorrelator where HWP is a half-wave plate, BS is a beam splitter, KTP is a potassium titanyl phosphate crystal, and PMT is a photomultiplier tube. **(b)** Image of the autocorrelator set up on the laser table.

The beam from the oscillator was split using a polarized beam splitter (BS) and, after travelling through different paths, was recombined in a nonlinear crystal, potassium titanyl phosphate (KTP). The pulses were recombined by adjusting the delay of one arm of the auto correlator, which was manipulated by a translational stage. When the delay was large, the pulses were shown as two separate curves, but as the delay approached Δt = 0, the pulses began to converge. The total energy of the SH pulse was the greatest when the two pulses incident on the nonlinear crystal temporally overlapped at Δt = 0. The

change of intensity as the pulses recombined was monitored by a PMT and sent to a computer for analysis using a GPIB interface and a LabVIEW code.

With a non-collinear setup, the SH was only measured for the overlap of the pulses, while the energy from the SH generated from each pulse itself was suppressed and not accounted for in the correlation trace. The correlation trace was fitted with a Gaussian function, Figure 3.4 (a). The pulse duration was calculated by dividing the full width at half maximum (FWHM), determined from Figure 3.4 (a), by the deconvolution factor of $\sqrt{2}$,[2] resulting in a pulse duration of 112 fs. A spectrum of the pulse with a wavelength of 804 nm is shown in Figure 3.4 (b).
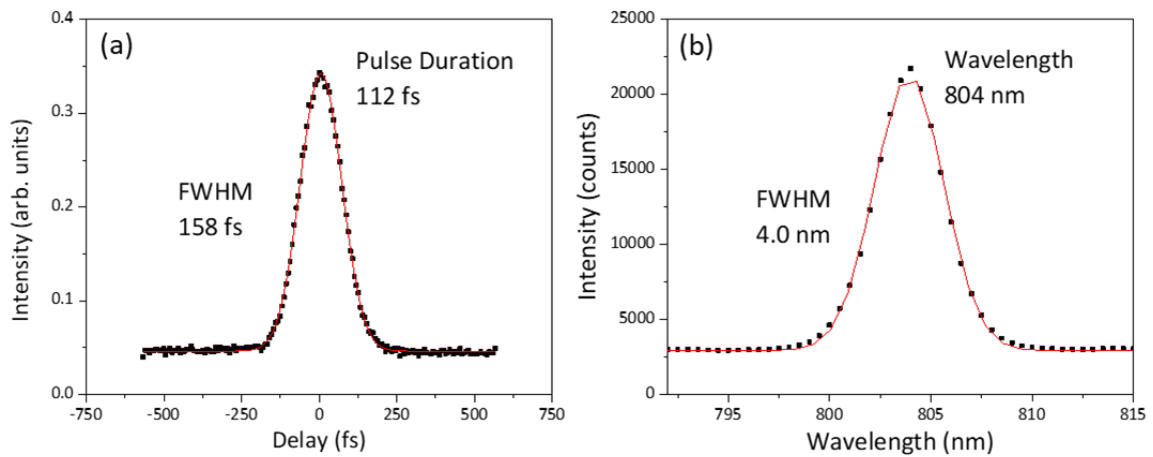
Figure 3.4 (a) Autocorrelation trace and the pulse duration determined from the full width at half maximum. **(b)** Spectrum taken of the pulse from the Ti:sapphire oscillator and the corresponding wavelength.

With a pulse duration of 112 fs, the laser system was characterized using the average output power from the oscillator, the repetition rate of the oscillator, and the measured beam size at the sample stage. From these parameters, the pulse energy, peak

power, and peak power density were calculated. All characterizations are shown in Table

3.1

Table 3.1 Characterization of the pulse.

Wavelength	804 ± 1.0 nm
Average Power	400 mW
Repetition Rate	79 MHz
Pulse Duration	112 ± 3 fs
Sample Beam Area	0.011 ± 0.001 mm^2
Pulse Energy	5.1 nJ
Peak Power	45208 W/pulse
Peak Power Density	0.422 GW/cm^2

3.3 Second Harmonic Generation Set-Up

The SH optical set-up has three main sections: the incident beam, the sample

stage, and the detection system. The layout is shown below in Figure 3.5.
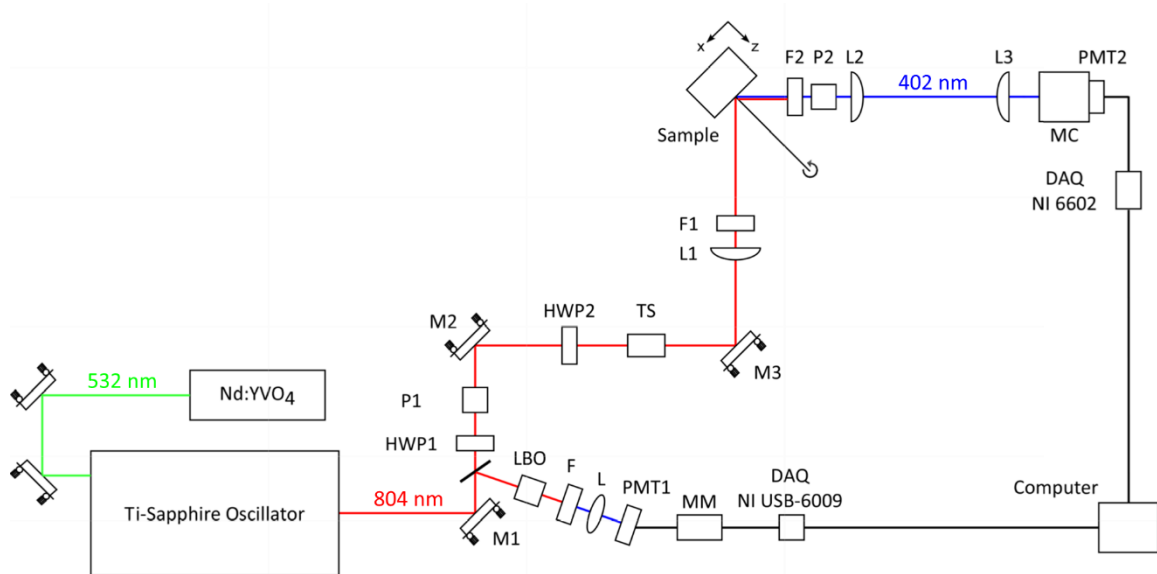
Figure 3.5 Top view schematic of the optical layout used in the set-up for generating the SH where M refers to a mirror, F refers to a filter, L refers to a lens, PMT refers to a photomultiplier tube, MM refers to a multimeter, LBO refers to a lithium triborate crystal, HWP refers to a half-wave plate, P refers to a polarizer, TS refers to a telescope, MC refers to a monochromator, and NI USB-6009 and NI 6602 are data acquisition devices.

The incident beam, also referred to as the fundamental beam, was centered at 804 nm with an average power of 400 mW. The fundamental beam was used to induce a polarization at the sample surface and to monitor the stability of the oscillator. Using a lithium triborate (LiB_3O_5) crystal (LBO), a filter (F), a lens (L), and a photomultiplier tube (PMT1), a reference arm was constructed to monitor the effect of fluctuations in the oscillator cavity on the SH. The signal from the PMT was observed by a multimeter, which sent the data to a computer through a National Instruments (NI) USB-6009 data acquisition (DAQ) device. From the reference channel, normalization of the SH signal against laser power fluctuations was achieved.

The fundamental beam passed through a half-wave plate (HWP1) and polarizer (P1) combination that act as an attenuator to adjust the intensity of the beam. A second half-wave plate (HWP2) allowed the polarization of the incident beam to be changed from vertically to horizontally polarized to the incidence plane. The telescope (TS) magnified the beam diameter three times its original size. A lens (L1) focused the beam onto the sample and an 815 nm bandpass filter (F1) was placed before the sample to separate the fundamental beam from any SH generated from any optical surface.

The sample was placed on a home-built sample stage, which allows for translation in the x-z plane for alignment purposes. The stage was also equipped for sample rotation about the surface normal. This allowed for the rotational anisotropy of samples to be examined. The fundamental beam polarized the surface of the sample at a 45° angle from the surface normal in the x-z plane, and the fundamental beam and the generated SH

were reflected at an angle of 45° from the surface normal.
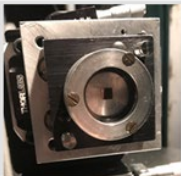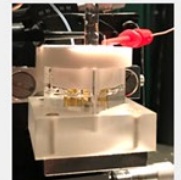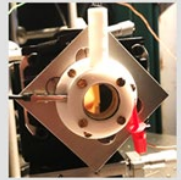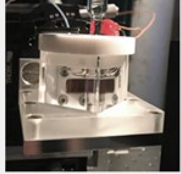
Both the fundamental and the SH beam were reflected towards the detection arm of the setup. A 415 nm bandpass filter (F2) separated the fundamental and SH beams allowing only the SH beam to be detected. A polarizer (P2) allowed only a certain polarization of the beams to be detected, whether it be parallel or perpendicularly polarized to the incidence plane. Prior to detection, the beams pass through two lenses. The first lens (L2) collimated the beam, and the second (L3) focused the beam on the slits of a monochromator. The monochromator transmitted a selected wavelength into the photon counting photomultiplier tube (PMT2). The PMT was connected to a NI 6602 DAQ device, which, in turn, was connected to a computer and through a LabVIEW code, the SH signal generated from the sample was collected and analyzed.

3.4 Cell Designs

The home-built sample stage was designed for multiple samples/systems to be studied with relatively simple changes. For rotational anisotropy measurements, a specialized cell was used to study samples both exposed to atmosphere and samples, which when the cell was put together in a glove box, limited the samples exposure to the atmosphere. For samples that were studied simultaneously with second harmonic generation and electrochemistry, two polytetrafluoroethylene (PTFE) caps were designed and machined to hold all electrodes in the appropriate quartz cuvette. This allowed for solid-liquid interfaces to be studied with an applied potential. An additional cell

constructed from PTFE was designed to study evaporated film samples, while eliminating any edge effects. Through the combination of the specialized sample stage and the different cell adapters, both gas-solid and solid-liquid interfaces of different systems were studied. Table 3.2 below gives a brief overview of all cells that will be further explained in the following sections.

Table 3.2 Overview of all cells designed and the potential sample and interfacial uses.

Cell	Sample	Interface	Picture
Rotational Cell	Copper Single Crystals	Gas-Solid	
Thin Film Cell	Gold Evaporated Films	Solid-Liquid	
PTFE Thin Film Cell – No Edges	Gold Evaporated Films	Solid-Liquid	
Bulk Metal Cell	Bulk Copper	Solid-Liquid	

3.4.1 Rotational Anisotropy Cell

For rotational anisotropy measurements, a cell was needed that could be easily assembled inside of a glovebox to minimize exposure to the atmosphere. This cell allowed

for the gas-solid interface to be studied. By machining an aluminum cell fitted with a Viton O-ring and a quartz window, the cell was able to be customized and mounted onto a repurposed mirror mount to allow for fine tilt adjustments to ensure proper alignment. The cell consisted of two aluminum halves, one referred to as the base and the other as the top. The base of the cell screwed into the repurposed mirror mount. It was also fitted with an inset for an aluminum disc ranging in thicknesses. The sample was mounted onto an aluminum disc with double sided tape. The disc was then placed in the base of the cell with a Viton O-ring, which had a width of 3.55 mm and an inner diameter of 21.2 mm, and quartz window placed on top. The top of the cell was fitted with a thin Viton O-ring to safely secure the quartz window, while preventing any damage. When the top of the cell was placed over the quartz window, three screws were then used to fasten the cell together creating a seal that minimized atmosphere exposure and contamination. A picture of the rotational cell attached to the sample stage is shown below in Figure 3.6.
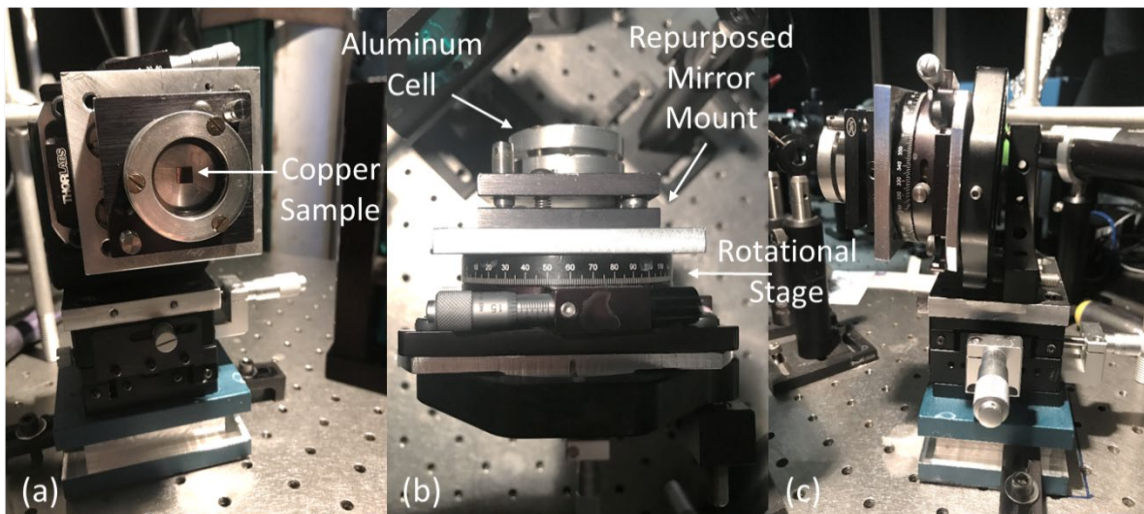
Figure 3.6 Rotational anisotropy cell for a gas-solid interface. **(a)** Front view of the stage, **(b)** Top view of the stage. **(c)** Side view of the stage.

3.4.2 Evaporated Film Cell

To study the reactions occurring at the surface of an evaporated film on silica, in most cases gold, with both cyclic voltammetry and SHG, a $20 \times 20 \times 20$ mm^3 quartz cuvette was utilized. This allowed for the solid-liquid interface to be probed under applied potentials. A specially designed PTFE cap was machined with both a lathe and milling machine. A 20×20 mm^2 square with a depth of about 8 mm was carved out of a 1.5 inch cylinder of PTFE using a Bridgeport milling machine. Three holes were drilled in the front diagonal half for the working, counter, and reference electrodes. An additional slit across the diagonal of the 20×20 mm^2 square was cut about 5 mm deep to hold both the evaporated film and the gold wire that allows contact between the film and the potentiostat. The back half of the cap also had three holes for a nitrogen purge line and a solution input and output. Figure 3.8 shows an image of the PTFE cap where the through holes and diagonal slit are clearly seen.

Figure 3.7 Evaporated film cell for solid-liquid interfaces where WE refers to the working electrode, CE refers to the counter electrode, RE refers to the reference electrode, and N_2 is the nitrogen purge line. **(a)** Front view of the cell. **(b)** The view of the cell along the direction of the beams travelled path. **(c)** Top view of the cell showing the electrode connections.

Figure 3.8 Image of the PTFE cap used for the evaporated film cell. **(a)** Image of the top side of the cap with 6 through holes for the electrodes, nitrogen purge line, and solution input and output. **(b)** Bottom view with the diagonal cut where the evaporated film fits into. **(c)** Side view of the PTFE cap.

To eliminate experimental complications due to edge effects, a second cell for the evaporated gold films was designed. The entire cell was constructed from PTFE. The cell consisted of a base for the evaporated film to rest on, a spacer 5 mm thick, and a top with

an inset for a quartz window. The spacer was fitted for two Viton O-rings that have a width

of 2 mm and an inner diameter of 20.5 mm. The O-rings created a seal between the

evaporated film on one side and between the quartz window on the other side. The 1

inch quartz window was 1 mm thick and was purchased from Esco Optics. On the top of

the spacer a 4-40 hole was drilled and tapped for a cylindrical tube, which was fitted for

the reference electrode. The cell body was fastened together with four 4-40 brass screws.

A picture of the assembled cell is shown below in Figure 3.9.
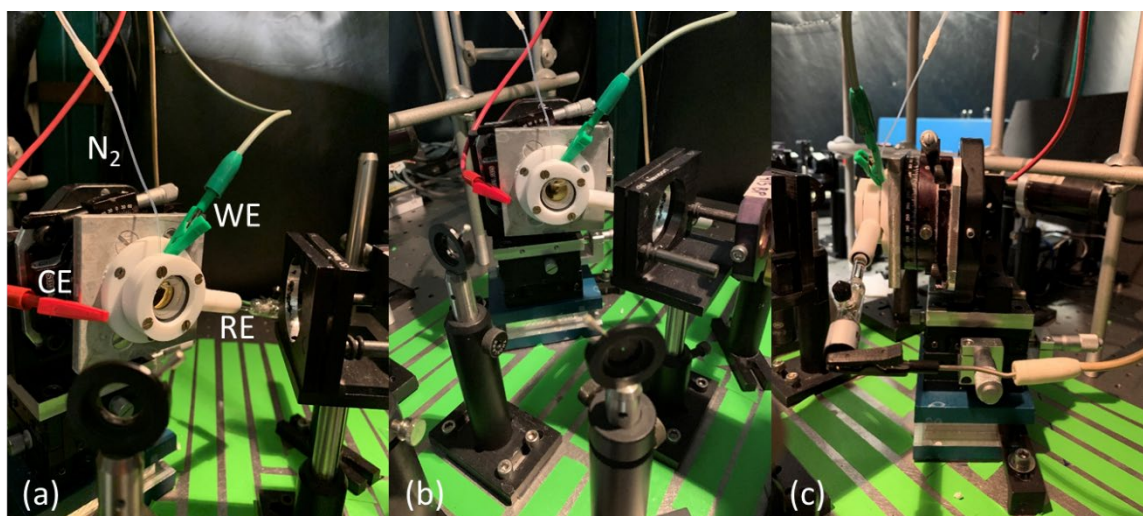
Figure 3.9 PTFE cell for solid-liquid interfaces used for evaporated film experiments. **(a)** View of the cell along the direction of the beams travelled path. **(b)** Front view of the assembled cell. **(c)** Side view of the cell on the sample stage.

A technical drawing of all the parts of the PTFE cell. Figure 3.10 (a) is the top fitted

with an inset for the quartz window. The 5 mm spacer fitted for two Viton O-rings is shown

in Figure 3.10 (b). The drawing shows the creation of a V-shaped cavity for a solid-liquid

interface. The specialized cavity is utilized to use a smaller sample size while having a 1

inch window for probing. Figure 3.10 (c) is the PTFE base where the sample rests on. All three parts are combined and fastened with four 4-40 brass screws.
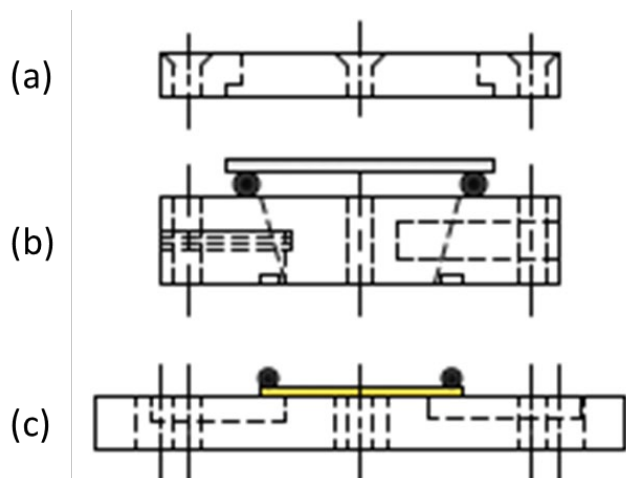
Figure 3.10 Technical drawing of the PTFE cell. **(a)** Top with an inset for a quartz window. **(b)** Spacer fitted for two Viton O-rings with a 5 mm cavity. **(c)** Base where the working electrode sits.

3.4.3 Bulk Metal Cell

To study bulk metals, an additional cell was needed to isolate the polished surface. This allowed for the solid-liquid interface to be probed under applied potentials without contributions without any exposure to the edges and back side of the sample. For bulk copper samples, a 30 × 30 × 30 mm^3 quartz cuvette with a customized PTFE cap was designed, which is shown in Figure 3.11. Starting with a two inches piece of PTFE, a 30 × 30 mm^2 square was machined to a depth of 25 mm. A 6.3 mm think trapezoid was created in the middle of the square across the diagonal. This left a 7 mm lip on the edges of the square so that the cap would be held inside the cuvette. The front side of the trapezoid was identified as the side centered at the middle diagonal of the square. Six 4-40 screw holes were drilled and then tapped on the front side of the trapezoid to attach the

window that secured the copper electrode. The window was a 19.6 × 28.8 mm^2 rectangle with a 9.5 × 23.5 mm^2 rectangle inset that was 7 mm deep. The window had six 4-40 through holes that were counter sunk to keep the 4-40 316 stainless steel screws from protruding. Three holes were drilled in the front diagonal half for the working, counter, and reference electrodes. Three additional holes were drilled in the back half of the cap for a nitrogen purge line and a solution input and output. Figure 3.12 shows images of the PTFE cap used from different angles to better understand the design and structure.
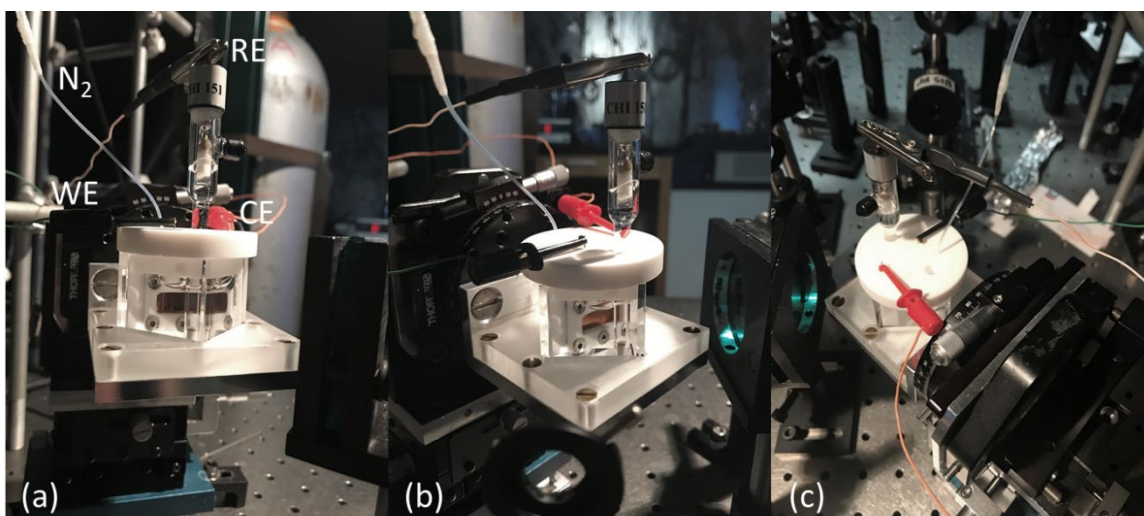
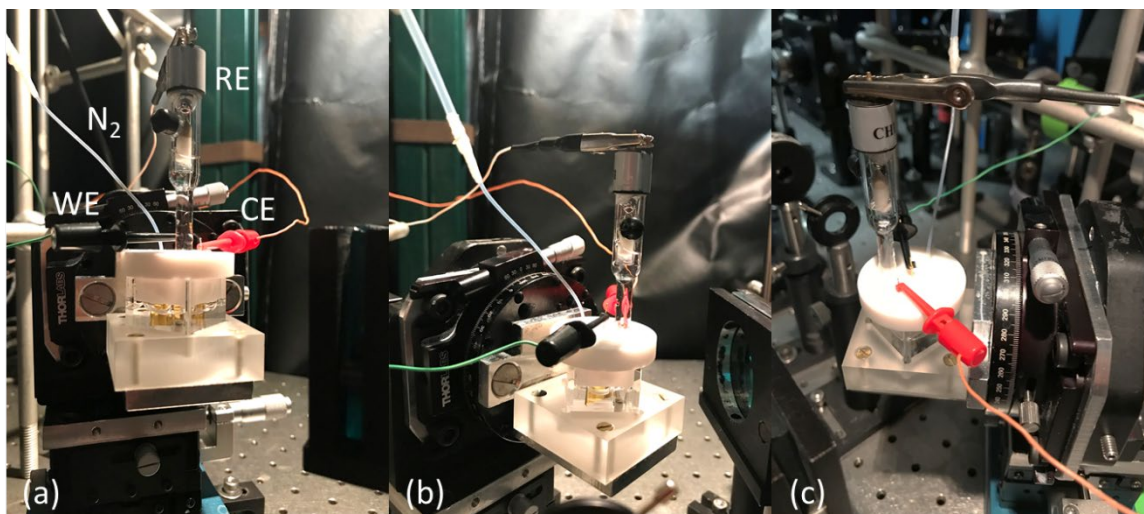**Figure 3.11** Bulk metal cell for a solid-liquid interface where WE refers to the working electrode, CE refers to the counter electrode, RE refers to the reference electrode, and N$_2$ is the nitrogen purge line. **(a)** Front view of the assembled cell. **(b)** The view of the cell along the direction of the beams travelled path. **(c)** Side view of the cell on the sample stage.
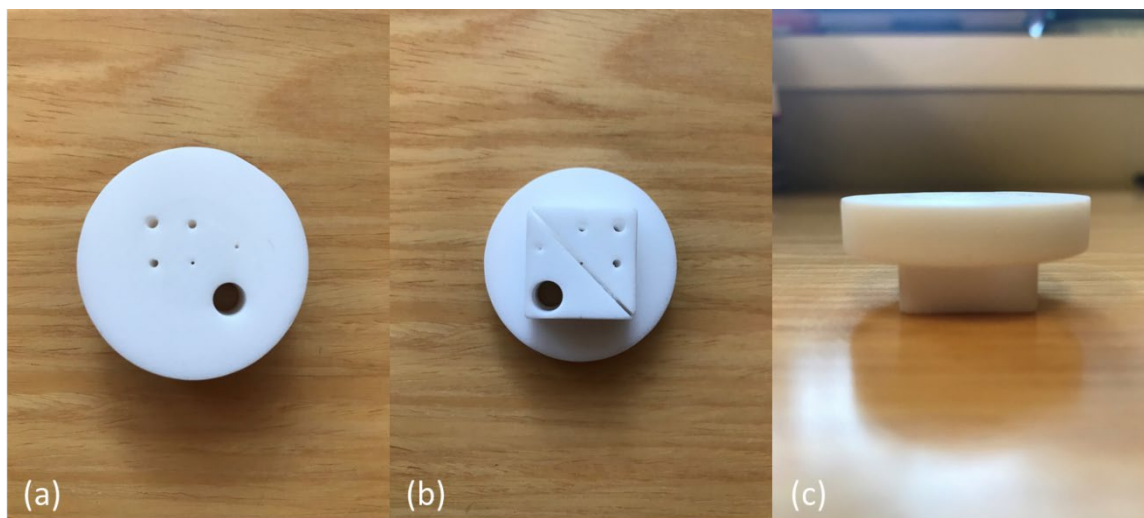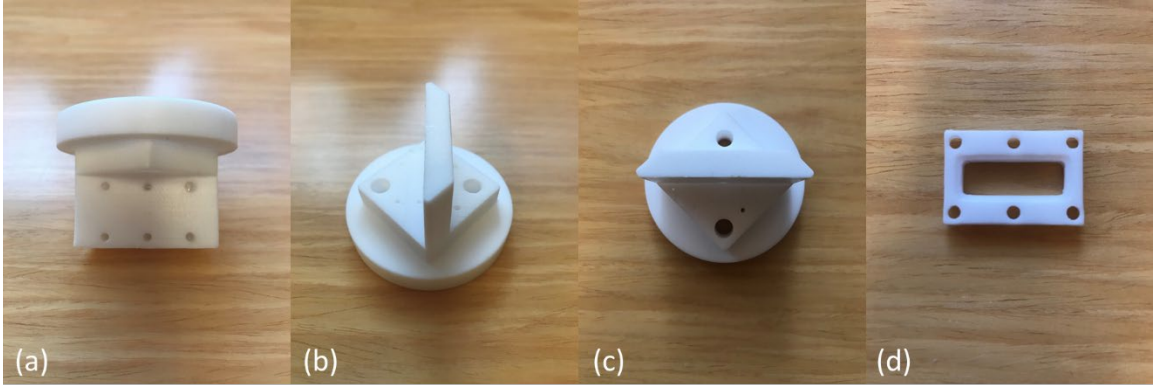
Figure 3.12 Image of the PTFE cap used for the bulk metal cell disassembled. **(a)** Front side of the trapezoid with the six screw holes. **(b)** Side view where the trapezoid slice can be easily identified. **(c)** Top view from the bottom of the cap. **(d)** The image of the window shows an inset where the bulk metal samples sits and the six through holes used to attach the window to the cap.

3.5 Calibration with GaAs(100)

GaAs(100) is a widely-studied cubic single crystal with a high second order susceptibility, making it a typical sample to calibrate the SH set-up.[3] Through rotational anisotropy, the modulation in the SH intensity was monitored as GaAs was rotated about its surface normal. Using a half-wave plate and a polarizer, the polarization of the fundamental and SH beams were adjusted. This allows for symmetry to be observed from all four polarization combinations: pp, ps, sp, and ss, where p refers to polarized light parallel to the incidence plane and s refers to polarized light perpendicular to the incidence plane. The results, which are consistent with literature, are shown in Figure 3.13.[3-7]
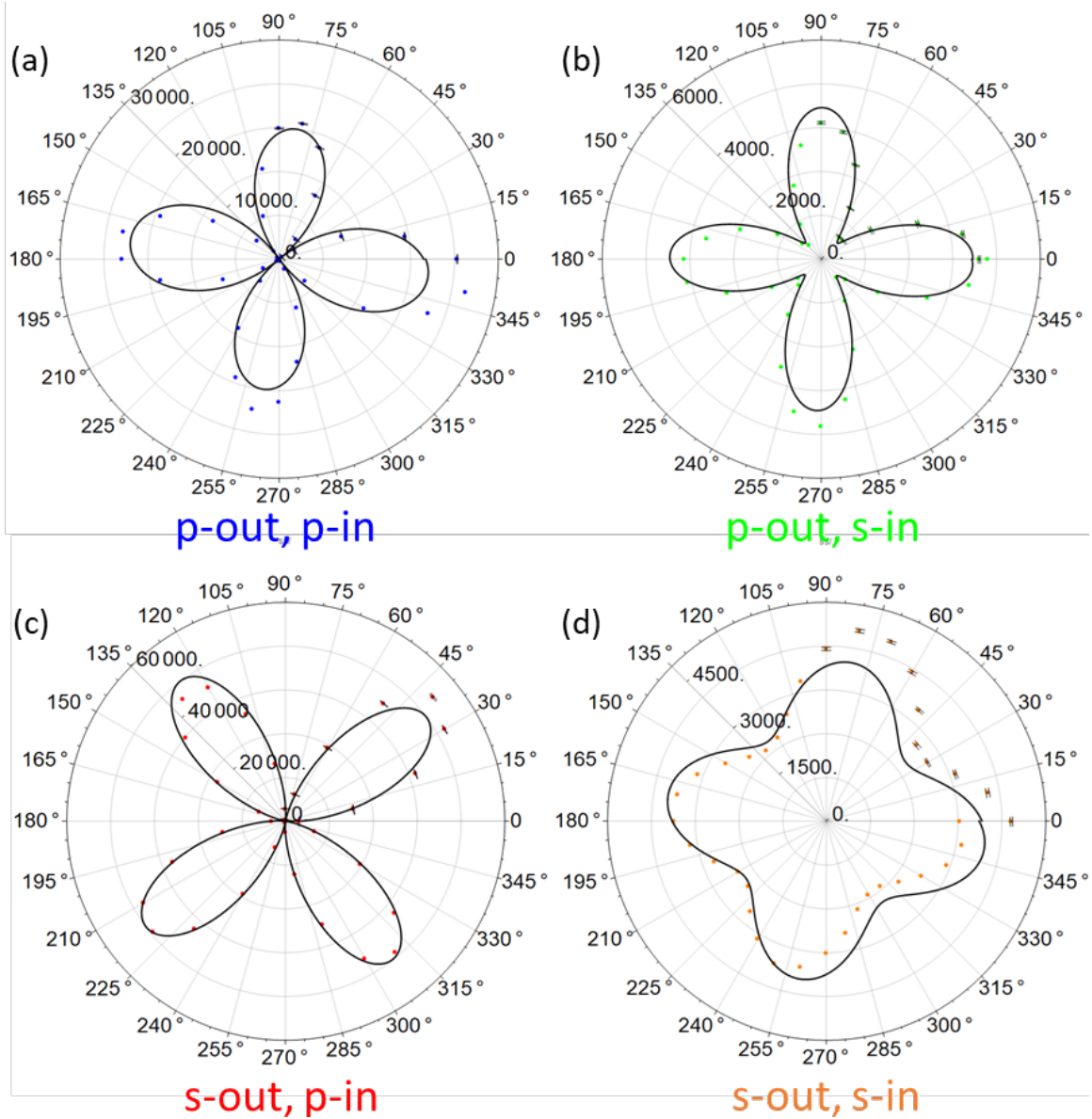
Figure 3.13 Polar plots for GaAs(100) at different polarization combinations **(a)** p-out, p-in; **(b)** p-out, s-in; **(c)** s-out, p-in; **(d)** s-out, s-in.

Figure 3.13 (b), (c), and (d) showed a four-fold symmetry, while Figure 3.13 (a) showed a two-fold symmetry where the petals at roughly 80° and 260° present a lower SH intensity than the other two petals. The four-fold symmetry was expected with any surface contribution from the single crystal, and literature suggested that the two-fold

symmetry present in the pp polarization combination comes from the interference between the surface and bulk susceptibilities.[3-6] It is difficult to specify the component of the surface susceptibility that is responsible for such anisotropy.[7]

The polar plots are fitted with a non-linear model function on Wolfram Mathematica. For ps, sp, and ss polarizations, the fit equation is shown in Equation 3.1. For the pp polarization, a two-fold symmetry was shown and the fit Equation 3.2 was used. Both equations are shown as a function of azimuthal angle, φ.

$$f(\varphi) = a + b \times \cos[c \times \varphi + d] \qquad [3.1]$$

$$f(\varphi) = \sqrt{(a + b \times \cos[c \times \varphi + d])^2} \qquad [3.2]$$

The variables a and b correspond to the isotropic and anisotropic contributions to the symmetry. The symmetry order is represented by c. The variable d is a phase correction with respect to φ. Table 3.3 shows the fitting parameters for each polarization combination.

Table 3.3 Fitting parameters for polar plots of GaAs(100) for all four polarization combinations.

	pp	sp	ss	ps
a	1287.6	23890	2955.59	2384.4
b	19233.3	24073.3	702.849	1764.4
c	2	-4	4	-4
d	50.5	15.1	0.56	0.03

3.6 Data Processing

The second harmonic signal from the sample and the reference arm were acquired by a LabVIEW program, simultaneously. The signal from the sample was sent through a monochromator to ensure that only the desired wavelength was collected by a photomultiplier tube. The Hamamatsu H6240 Series photon counting PMT was connected to a BNC 2121 connector accessory, which communicated with LabVIEW through a DAQ NI PCI 6602.The signal from the reference channel was collected by an International Light PMT and monitored by a Keithley 6517 electrometer, which sent the data to LabVIEW through a DAQ NI USB-6009.

(a)

55
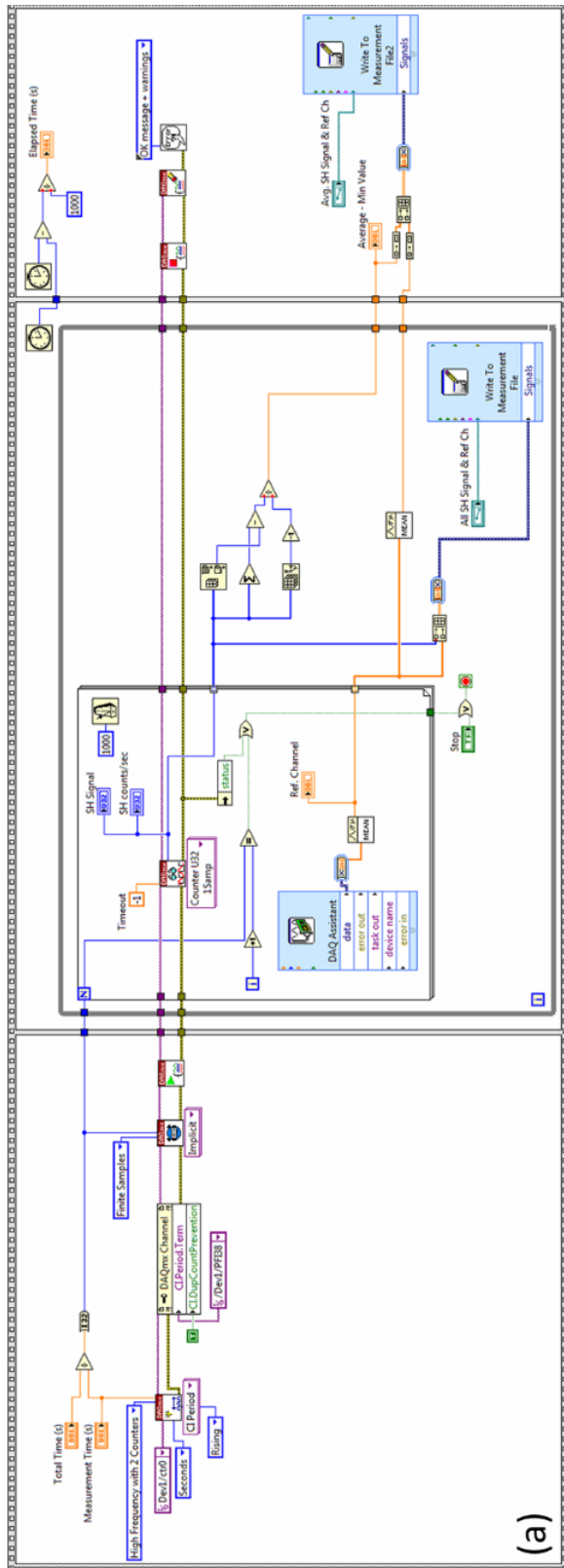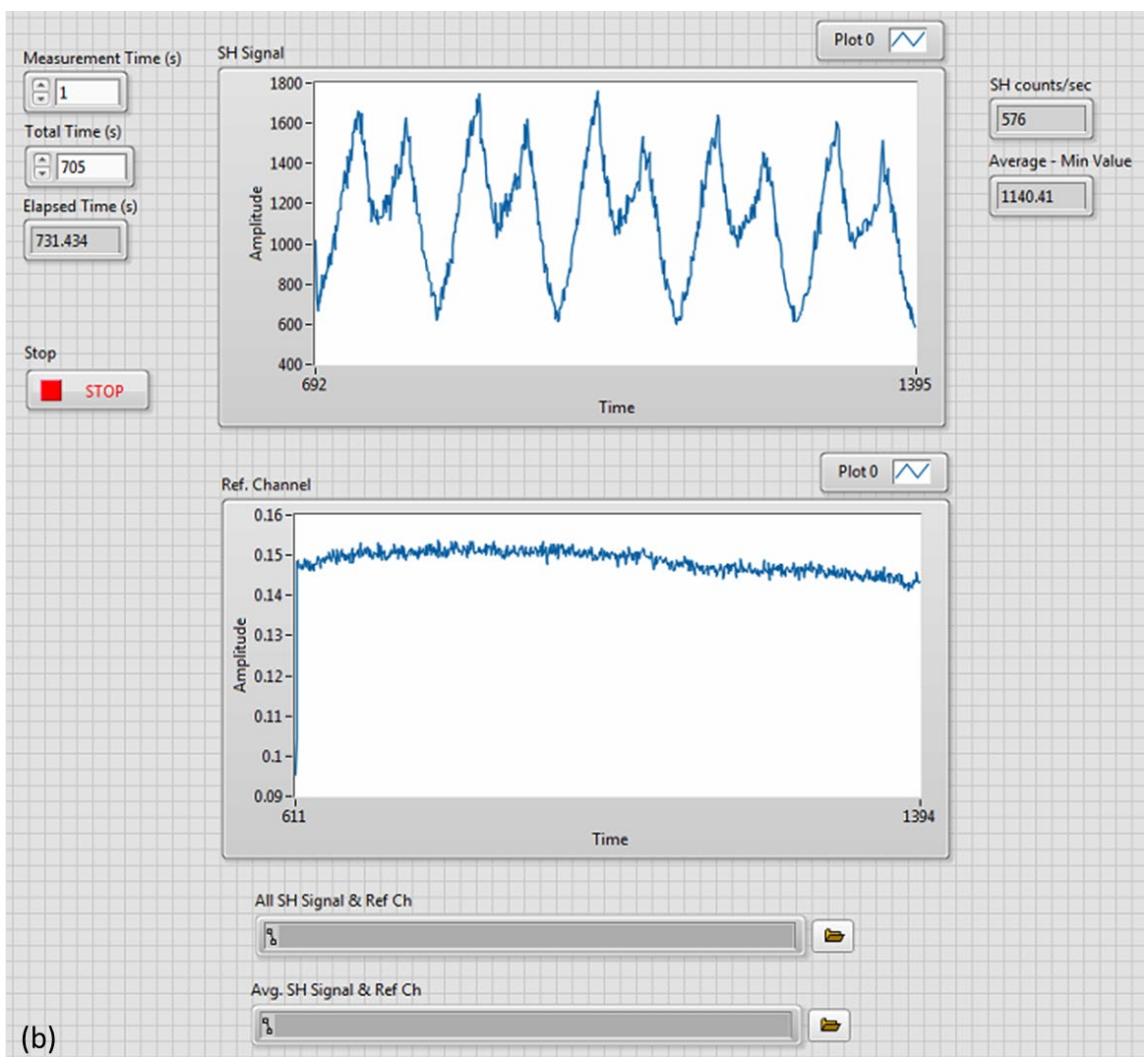
Figure 3.14 LabVIEW program used for the simultaneous collection of the SH signal and the reference channel. Program file located on the SHG computer at the file directory M:\Michelle\LabVIEW Programs\SH Signal & Ref Ch. **(a)** Block diagram of the LabVIEW program. **(b)** Front panel of the LabVIEW program where the signal from both channels are monitored on a waveform chart.

Figure 3.14 shows both the block diagram and front panel of the LabVIEW code used for data acquisition (DAQ). A flat sequence structure was used to ensure that each frame executes sequentially. The code was broken up into three sections as seen in Figure 3.14 (a). The top line of DAQmx tasks corresponded to the signal acquired from the

sample in question. In the second section of the flat sequence, there was a for-loop inset in a while-loop. The for-loop was set to execute n-times depending on the set measurement and total time. These timing features were set in the front diagram shown in Figure 3.14 (b). In the second sequence, a DAQ Assistant was used for collecting signal from the reference channel. On the front panel, shown in Figure 3.14 (b), the SH signal and reference channel data were shown on their corresponding waveform chart. This was useful for monitoring any sudden changes in the SH signal and to help determine whether it was originating from a change in the chemical system being studied or from the oscillator.

The signal from both the DAQmx task and the DAQ Assistant were combined and written to a measurement file. After the total time had elapsed, two windows appeared prompting the user to save the acquired data. Two files were saved: one with every data point collected and the other where the average of the data was taken and appended in one text file. The measurement files were imported into Wolfram Mathematica for further manipulation. The background noise for each PMT was subtracted from the raw data. The intensity of the SH, I_{SH}, was corrected for any oscillator fluctuations by dividing the background subtracted SH signal by the background subtracted reference channel signal. This is shown in Equation 3.3 where $I_{SH,raw}$ is the raw SH intensity from the sample and $I_{SH,back}$ is the background from the PMT used for sample data collection. $I_{ref,raw}$ represents the intensity of the raw SH from the reference channel and $I_{ref,back}$ is the background signal from the PMT used for the reference channel. In Equation 3.3 the

intensity of the SH is shown as a function of scan number, n. This is for measurements

taken in real-time with respect to cyclic voltammetry.

$$I_{SH}(n) = \frac{(I_{SH,raw} - I_{SH,back})}{(I_{ref,raw} - I_{ref,back})}$$ [3.3]

$$Norm[I_{SH}] = \frac{I_{SH}(n)}{Max[I_{SH}(n=30)]}$$ [3.4]

For electrodesorption experiments, a total of 30 CV cycles were scanned. To

normalize the SH intensity, the maximum value of the thirtieth scan was used. Here, a

bare electrode is expected, which is why the data set for scans $1 - 29$ are normalized to

this point. After the SH signal was normalized and divided accordingly, the data was

exported to a text file. The data was then imported into Origin Pro 8.6 for graphing. The

SH data can be used independently or combined with any simultaneously acquired cyclic

voltammetry data. For the acquisition of SH during electrochemical experiments, the data

is plotted as a function of potential. This allows for the SH to be correlated to different

chemical reactions at the electrode surface.

A sample plot is shown in Figure 3.15, where both the SH and cyclic voltammetry

are plotted as a function of potential (V) with respect to a mercury-mercurous sulfate

electrode, MSE. The left hand y-axis is the current density in µA/cm^2 for the

voltammogram. The right hand y-axis is the normalized SH intensity. The CV shows the

oxidation and reduction of gold, which corresponds with a decrease and increase in the

SH, respectively. The oxidation of gold occurs from 0.7 to 0.8 V. The reduction of gold is

shown by a sharp peak around 0.5 V. The plot confirms the sensitivity of the SH to

chemical reactions occurring at the working electrode.
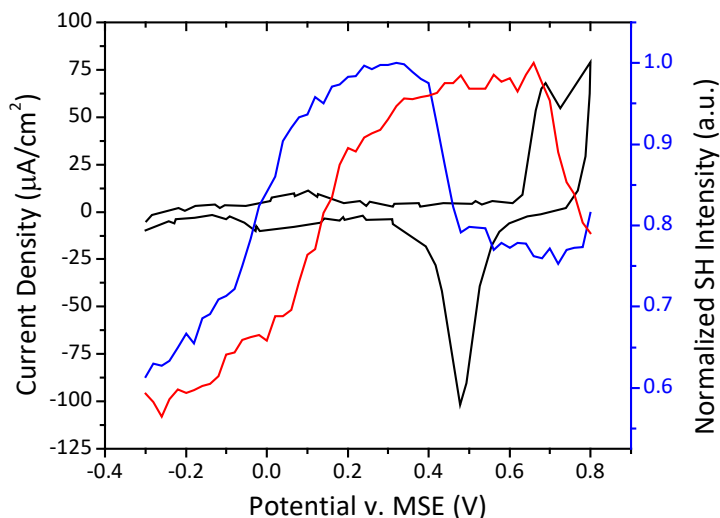
Figure 3.15 Double plot of a gold WE in 0.1M H_2SO_4. Scan Rate: 20 mv/s. The black solid curve is the cyclic voltammogram. The blue and red solid curves are the SH intensity for the cathodic and anodic curves, respectively.

3.7 Electrochemistry

All electrochemistry measurements consisted of a three electrode system driven by a 263A Princeton Applied Research Potentiostat/Galvanostat. The following subsections describe the cleaning procedures and sample preparation for all materials used in electrochemical experiments as well as the necessary solutions and underpotential deposition procedure.

3.7.1 Electrodes

All electrodes have a specific cleaning and storing protocol. The evaporated gold film working electrodes (WE) wer stored in ultra-pure water from a Millipore system with

an 18.2 MΩ · cm resistivity. For experimental use, the gold film was removed from ultra-pure water, washed with ethyl alcohol 200 proof, washed with the corresponding electrolyte solution, and then placed into the PTFE cap and into the cell. The bulk copper sample working electrode was stored in ethyl alcohol 200 proof. For experimental use, the copper sample was rinsed with ethanol and then dried with nitrogen before being mounted in the cap holder. The counter electrode (CE) used in all experiments was a 0.5 mm platinum wire (99.95%) purchased from Alfa Aesar. Platinum was cleaned in a 50:50 volume ratio of nitric to sulfuric acid for several hours, washed thoroughly with ultra-pure water, and then flame annealed with a hydrogen flame before use. Clean platinum was stored in ultra-pure water. The reference electrode (RE) used was a mercury-mercurous sulfate electrode (MSE) stored in a saturated K_2SO_4 solution; it was purchased from CH Instruments, Inc. Prior to and after use, the RE was washed with copious amounts of ultrapure water.

3.7.2 Electrochemical Cells

All quartz cuvettes were purchased from eBay seller QuartzCrystal. They were cleaned in a 50:50 HNO_3:H_2SO_4 acid mixture and thoroughly washed with ultra-pure water. In between uses, all quartz cuvettes were stored in ultra-pure water. All PTFE pieces, both caps and the cell, were cleaned in a 50:50 HNO_3:H_2SO_4 acid mixture, thoroughly washed with ultra-pure water, and then kept in ultra-pure water overnight before being used. Clean PTFE was stored in ultra-pure water between uses. Viton O-rings were boiled in ultra-pure water six times and then stored in ultra-pure water.

3.7.3 Chemical Solutions

Electrolytes were made using ultra-pure water from a Millipore system with an 18.2 M$\Omega \cdot$ cm resistivity. Ultrapure sulfuric acid (93 – 98%) was purchased from J. T. Baker and used as received. Potassium hydroxide (88%) was purchased from Mallinckrodt Chemicals and used as received. Both the acidic and basic electrolytes were used at a concentration of 0.1M. Copper (II) sulfate pentahydrate (98+%) was purchased from Sigma Aldrich and used as received. A 1mM $CuSO_4 \cdot 5H_2O$ in 0.1M H_2SO_4 was used for all copper underpotential deposition experiments. All solutions were degassed with ultra-high purity nitrogen (99.999%) prior to experiments for 15 minutes. Potassium hydroxide was degassed for a minimum of 30 minutes. All systems were kept under nitrogen flow during the entirety of the experiments.

The alkanethiols 1-dodecanethiol (≥98%) and 1-octadecanethiol (98%) were purchased from Sigma Aldrich and were used as received. 1-decanethiol (96%) was purchased from Alfa Aesar and was used as received. All alkanethiols solutions were prepared at a concentration of 5mM with ethyl alcohol 200 proof purchased from Decon Laboratories.

3.7.4 Sample Preparation

Gold shot (99.999%) was purchased from Kamis Incorporated. Chromium rods (99.9%) were purchased from R.D. Mathis Company. Silicon single crystal, Si(100), wafers were purchased from University Wafer and were only polished on one side. All

gold samples were preconditioned in 0.1M H_2SO_4 with a scan rate of 50 mV s^{-1} in the range of -0.3 V to 0.825 V with respect to a mercury-mercurous sulfate electrode (vs. MSE).

Copper foil (99.999%) 1.0 mm thick was purchased from Alfa Aesar. From the copper foil, a sample size was cut to roughly 9.5 × 23.5 mm^2 with a diamond wafering blade. The sample was mounted in a standard 1 inch-diameter mold with epoxy using a 10:2 ratio of Koldmount resin powder to Koldmount curing liquid purchased from Precision Surfaces International, Inc. The epoxy took about 30 minutes to set. Once the sample was set, the sample surface was cut with a 2000 grit abrasive sheet until all four corners of the sample no longer have a visible layer of epoxy. This side of the copper was then considered flat, so the sample piece was dismounted from the epoxy by soaking in acetone overnight. Once dismounted, the sample piece was flipped and remounted in epoxy using the above procedure. Again, the copper piece was cut using a 2000 grit abrasive sheet. After the removal of any noticeable epoxy around the edges, the surface was ground for 3-4 minutes in a figure eight motion to ensure an even distribution of pressure along the surface. Next, the sample was polished with diamond paste on final finish polishing cloths purchased from Precision Surfaces International, Inc. starting with 20, 6, 3, 1.5, 0.05-micron diamond paste. The sample was polished for 3-4 minutes with each paste, then sonicated in isopropanol for 30 minutes to remove any particles and to ensure no cross contamination between pastes. To finish, the copper piece was polished for 3-4 minutes with a 0.05-micron alumina-water slurry, then sonicated in ultrapure

water for 20 minutes. The copper piece was washed with isopropanol, then stored in ethyl alcohol 200 proof.

3.7.5 Underpotential Deposition

For deposition of a monolayer of copper on polycrystalline gold, the electrodes were immersed in an aqueous solution of $CuSO_4 \cdot 5H_2O$ and a potential of -0.4 V (vs. MSE) was held for 30 seconds. Prior to the underpotential deposition of copper, a cyclic voltammogram was recorded with a scan rate of 20 mV s^{-1} in a range from 0.1 V to -0.4 V (vs. MSE). This CV is shown in Figure 3.16 (a) with the corresponding SH intensity. The left hand y-axis is the current density in $\mu A/cm^2$ for the voltammogram. The right hand y-axis is the normalized SH intensity. Both y-axes are shown as a function of potential (V) with respect to a mercury-mercurous sulfate electrode, MSE. The deposition and stripping of copper is a reversible process and is shown in the CV in Figure 3.16 (a). Cycling from 0.1 to -0.4 V, copper is deposited and the SH increases shown as the solid blue curve. Reversing the potential strips the copper from the electrode and the SH decreases shown as the solid red curve.
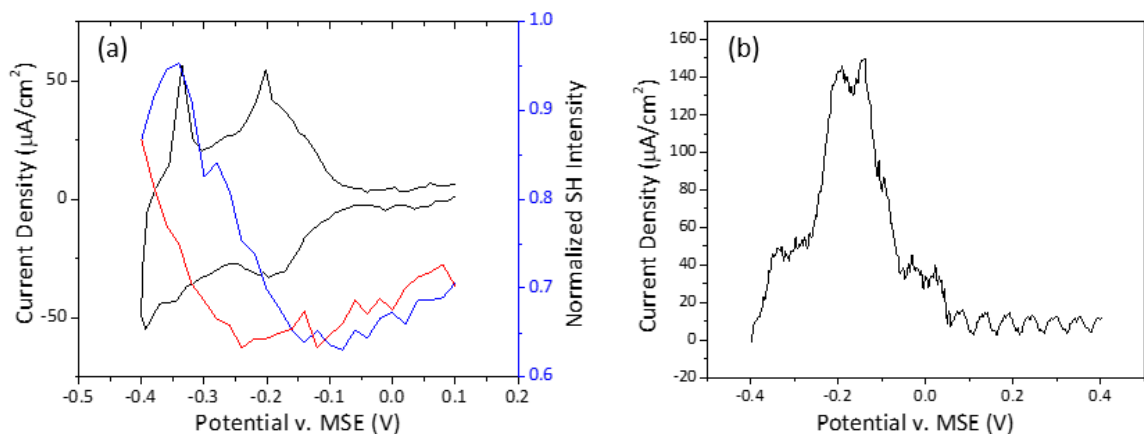
Figure 3.16 (a) Double plot of the underpotential deposition of copper on a gold WE in 1mM $CuSO_4 \cdot 5H_2O$ in 0.1M H_2SO_4 in parallel with SH acquisition. Scan Rate: 20 mv/s. The black solid curve is the cyclic voltammogram. The blue and red solid curves are the SH intensity for the cathodic and anodic curves, respectively. **(b)** Linear sweep voltammogram of the stripping of copper from a gold WE in 0.1M H_2SO_4. Scan Rate: 20 mv/s.

Figure 3.16 (b) shows a linear sweep voltammogram of the stripping of copper from a gold WE. By integrating the curve, a charge density of 8.10×10^{-4} C/cm^2 was calculated. This corresponded to roughly 2 ML of copper deposited onto a gold WE. This could be due to the roughness of the electrode and from not subtracting the baseline from the voltammogram prior to integrating. However, this confirmed a deposition of copper onto evaporated gold.

3.8 References

1.   Bloembergen, N.; Pershan, P. S., Light Waves at the Boundary of Nonlinear Media. *Phys. Rev.* **1962,** *128* (2), 606-622.

2.   Weiner, A., *Ultrafast optics*. John Wiley & Sons: 2011; Vol. 72.

3.   Takebayashi, M.; Mizutani, G.; Ushioda, S., Azimuthal angle dependence of optical second harmonic intensity from a vicinal GaAs(001) wafer. *Opt. Commun.* **1997,** *133* (1), 116-122.

4.   Lazarescu, V.; Lazarescu, M. F.; Santos, E.; Schmickler, W., Second harmonic generation and impedance spectroscopy at n-GaAs(1 0 0) electrodes. *Electrochim. Acta* **2004,** *49* (24), 4231-4238.

5.   Tanaka, H.; Mizutani, G.; Ushioda, S., A new resonance of the surface SHG from GaAs(001) in air. *Surf. Sci.* **1998,** *402-404*, 533-536.

6.   Hollering, R. W. J., Bulk and surface second-harmonic generation in noncentrosymmetric semiconductors. *Opt. Commun.* **1992,** *90* (1), 147-150.

7.   Yamada, C.; Kimura, T., Rotational symmetry of the surface second-harmonic generation of zinc-blende-type crystals. *Physical Review B* **1994,** *49* (20), 14372-14381.

Chapter 4
Reductive Desorption of Alkanethiols

This chapter compares the reductive desorption of self-assembled monolayers (SAMs) on gold and an underpotential deposition (UPD) copper layer on gold. Real time second harmonic generation (SHG) was used to monitor changes at the surface as the self-assembled monolayer was electrodesorbed from the substrate through cyclic voltammetry (CV). This study is focused on three alkanethiols: 1-decanethiol (DT), 1-dodecanethiol (DDT), and 1-octadecanethiol (ODT). Before and after reductive desorption, samples are checked with sum frequency generation (SFG) spectroscopy, X-ray photoelectron spectroscopy (XPS), and contact angle (CA). These techniques confirmed the electrodesorption of short chain alkanethiols, while long chain alkanethiols were proven to remain near the surface of the electrode. However, for a DDT monolayer on the copperUPD-gold electrode was made. While DDT was easily desorbed from a gold substrate, the DDT behaved similarly to a long chain on the copperUPD-gold electrode. These observations will be further discussed and a hypothesis is proposed as to how the copperUPD layer stabilizes the DDT monolayer.

4.1 Introduction

At metal surfaces, two forms of surface modification have provided the possibility of tailoring a surface's properties. Underpotential deposition (UPD) is the phenomenon

of the electrodeposition of a metal adlayer onto a dissimilar metal.[1-3] Generally, UPD is used to form an adlayer with a coverage of no more than a monolayer. Self-assembled monolayers (SAMs) are organic molecules that spontaneously adsorb onto metal or metal oxide surface. The most common SAMs are *n*-alkanethiols, which form a well-ordered, oriented monolayer on metal substrates.[3-5] The monolayer thickness can be easily controlled within a few Angstroms (Å).[3, 5] With the ability to form structured and ordered adlayers, these systems can serve as models for modifying surfaces and interfaces. Potential applications of adlayers include wetting, lubrication, sensors, and corrosion inhibition, to name just a few.[6-12]

4.2 Experimental

4.2.1 Materials

Electrolytes were made using ultra-pure water from a Millipore system with an 18.2 MΩ · cm resistivity. Potassium hydroxide (88%) was purchased from Mallinckrodt Chemicals and used as received. Both the acidic and basic electrolytes were used at a concentration of 0.1M. Ultrapure sulfuric acid (93 – 98%) was purchased from J. T. Baker and used as received. Copper (II) sulfate pentahydrate (98+%) was purchased from Sigma Aldrich and used as received. A 1mM $CuSO_4 \cdot 5H_2O$ in 0.1M H_2SO_4 was used for all copper underpotential deposition experiments. All solutions were degassed with ultra-high purity nitrogen (99.999%) prior to experiments for 15 minutes. Potassium hydroxide was

degassed for a minimum of 30 minutes. All systems were kept under nitrogen flow during the entirety of the experiments.

The alkanethiols 1-dodecanethiol (≥98%) and 1-octadecanethiol (98%) were purchased from Sigma Aldrich and were used as received. 1-decanethiol (96%) was purchased from Alfa Aesar and was used as received. All alkanethiols solutions were prepared at a concentration of 5mM with ethyl alcohol 200 proof purchased from Decon Laboratories.

4.2.2 Sample Preparation

Gold shot (99.999%) was purchased from Kamis Incorporated. Chromium rods (99.9%) were purchased from R.D. Mathis Company. Silicon single crystal, Si(100), wafers were purchased from University Wafer and were only polished on one side. Gold wafers for alkanethiol deposition were washed with absolute ethanol and used as is.

Before deposition of copper, gold evaporated films were electrochemically cycled in 0.1M H_2SO_4 with a scan rate of 50 mV s^{-1} in the range of -0.3 V to 0.825 V with respect to a mercury-mercurous sulfate electrode (vs. MSE). The gold film was immersed in an aqueous solution of $CuSO_4 \cdot 5H_2O$ and a potential of -0.4 V (vs. MSE) was held for 30 seconds. Prior to the underpotential deposition of copper, a cyclic voltammogram was recorded with a scan rate of 20 mV s^{-1} in a range from 0.1 V to -0.4 V (vs. MSE).

Evaporated gold films were immersed for 24 hours, while the copperUPD-gold film was immersed for 3 hours. Samples were removed from solution, washed with ethyl

alcohol 200 proof, and blown dry with nitrogen gas. Samples were assembled in a specialized PTFE cell.

4.2.3 Cyclic Voltammetry and In-situ Second Harmonic Generation

All electrochemistry measurements consisted of a three electrode system driven by a 263A Princeton Applied Research Potentiostat/Galvanostat. Cyclic voltammetry of the reductive desorption of SAMs was performed in a specialized PTFE cell with the use of 0.5 mm platinum as the counter electrode (CE) and a mercury-mercurous sulfate electrode (MSE) as the reference electrode (RE). The potential of a MSE with respect to the standard hydrogen electrode (SHE) is +0.64 V. A solution of 1M KOH served as the electrolyte.

In-situ SHG was performed with a 79 MHz Ti:Sapphire oscillator which generates 804 nm mode locked pulses with an average power of 400 mW. The fundamental beam irradiates on the sample surface at an incident angle of 45°. Both the fundamental and SH beams were p-polarized. SH data acquisition was monitored via a PC using Labview (National Instruments).

Cyclic voltammograms were recorded starting at -0.4 V and ending in a potential necessary for alkanethiol desorption. For experiments where SH and CVs are recorded in parallel, a scan rate of 20 mV/s was used.

4.3 Comparison between Substrates

A thorough comparison between a bare gold film and bare copperUPD-gold film was needed. This provided a baseline for all techniques in reference to electrodes with and without alkanethiols. Both substrates were examined with in-situ SHG and CV and ex-situ SFG, CA, and XPS. For the gold film, two cases were examined. One where the gold film was washed with 200 proof absolute ethanol. The second is where the gold film was electrochemically cleaned from -0.3 to -1.825 V at 50 mV/s for 10 cycles. This gold is referred to as cycled gold.

4.3.1 Cyclic Voltammetry and In situ Second Harmonic Generation

With the use of the specialized PTFE cell shown in *3.4.2*, bare gold was monitored with SHG while cyclic voltammograms were recorded between -0.4 V and -1.95 V at stepped potentials to mimic the potential range for alkanethiol desorption. For SAM desorption, three potential ranges are used, all starting at -0.4 V and ending at -1.85, -1.9, or -1.95 V. These three plots are shown below in Figure 4.1. For plots (a), (b), and (c), the left hand y-axis is the current density in $\mu A/cm^2$ for the voltammogram. The right hand y-axis is the normalized SH intensity. Both y-axes are shown as a function of potential (V) with respect to a mercury-mercurous sulfate electrode, MSE.

Figure 4.1 A gold WE in 1M KOH is cycled in parallel with SH acquisition. Scan Rate: 20 mv/s. The black solid curve is the cyclic voltammogram. The blue and red solid curves are the SH intensity for the cathodic and anodic curves, respectively. The SH intensity was fitted with a linear curve at three ranges. Plot **(a)** shows the potential range from -0.4 to -1.85 V, **(b)** shows the potential range from -0.4 to -1.9 V, and **(c)** shows the potential range from -0.4 to -1.95 V. The SH intensity in each plot was divided in three sections where a slop change was observed. The areas were fitted with a linear line and the resulting slope is listed on the plots.

From the SH intensities in Figure 4.1, three different slopes can be assigned to three regions of the CV. The first region is from -0.4 to -0.8 V in both the cathodic and anodic sweeps. This slope in SH coincides to the reduction and oxidation of gold. The second region is from -0.8 to -1.65 V in both the cathodic and anodic sweeps of the CV. This is region is known as the double layer and the slope change in the SH is a response to the charging of the gold electrode. Finally, from -1.65 to -1.95 V in the cathodic sweep,

the sharp peak in the CV is from the hydrogen evolution reaction (HER). This also gives a third slope in the SH. The most noticeable change in Figure 4.1 is due to the increase in hydrogen evolution from stepping further negative in the cathodic region. From the plots in Figure 4.1, there is a change in the SH intensity without the presence of an alkanethiol monolayer. These plots provide a reference to compare the behavior of the SH with that of a modified electrode.

Once copper was deposited onto a gold film, the now copperUPD-gold film was transferred to the PTFE cell and immersed in 1M KOH. A potential was applied and swept over potential ranges where SAM desorption occurs. Due to in situ SH measurements in parallel with cyclic voltammetry, the potential was stepped less negative as needed to prevent the formation of bubbles on the surface due to hydrogen evolution. In Figure 4.2, the potential range from (a) to (e) starts at -0.4 V and reverses at -1.9, -1.95, -2.0, -2.05, and -2.1 V, respectively.

The SH intensity of a copperUPD-gold film with respect to the potential can be divided into three regions. The first is from -0.4 to -0.7 V in both the cathodic and anodic sweeps, which is from the reduction and oxidation of both the copper and gold. The second region is the double layer from -0.7 to -1.6-1.75 V in both the cathodic and anodic sweeps. The third region is from -1.6-1.75 to -2.1 V, which is in response to the hydrogen evolution reaction. These three regions result in three slope changes in the SH intensity. Again, there is a noticeable change in the slope as the potential is stepped further negative in the cathodic scan resulting in the evolution of hydrogen.

72

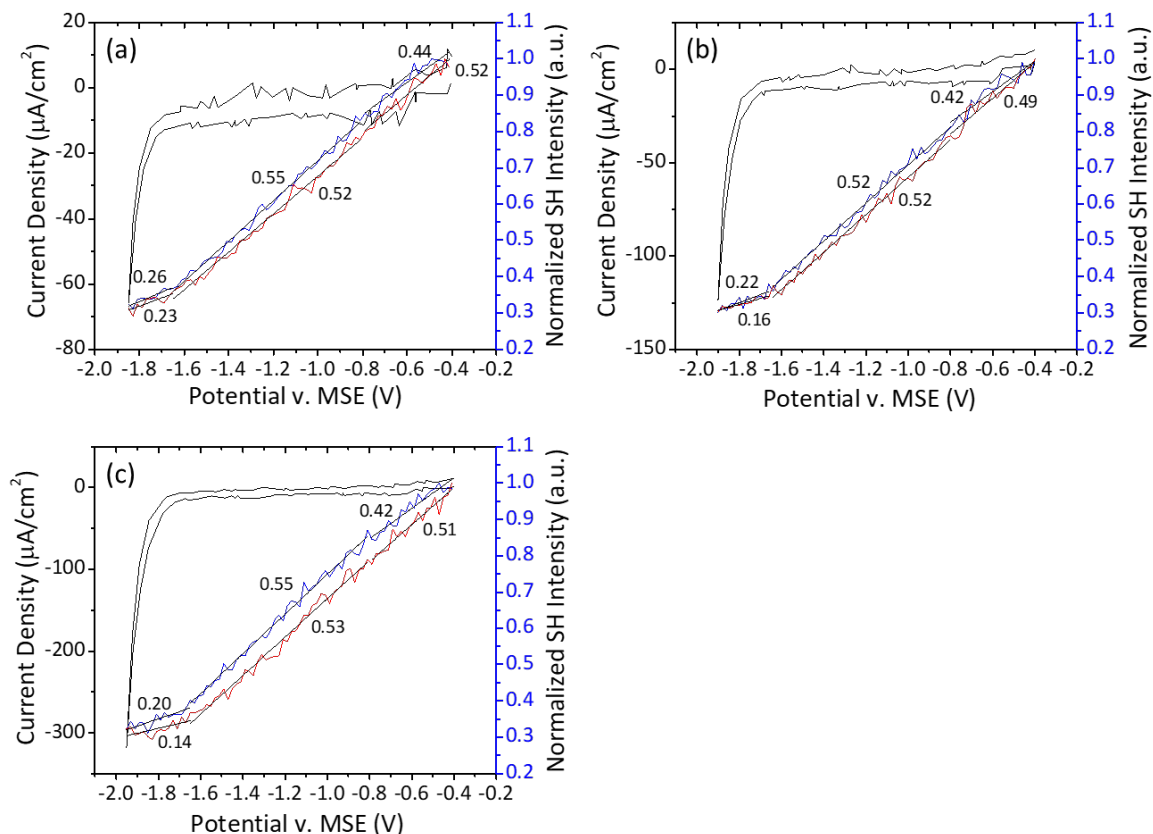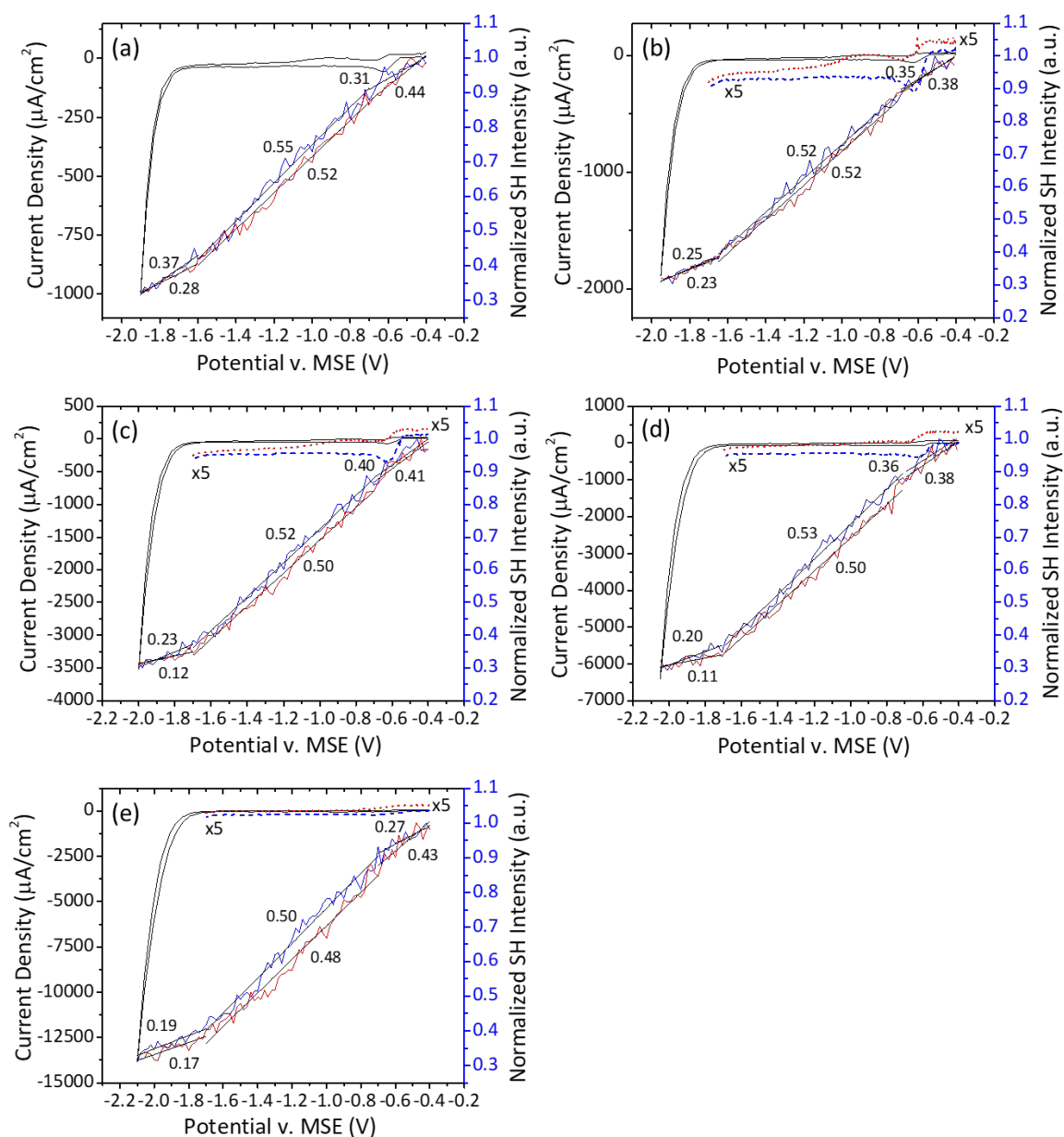**Figure 4.2** A copperUPD-gold WE in 1M KOH is cycled in parallel with SH acquisition. Scan Rate: 20 mv/s. The black solid curve is the cyclic voltammogram. The blue and red solid curves are the SH intensity for the cathodic and anodic curves, respectively. The region between -0.4 to -1.7 V is magnified by 5 times. The dashed blue curve is the zoomed cathodic region and the dotted red curve is the zoomed anodic region. The SH intensity in each plot was divided in three sections where a slop change was observed. The areas were fitted with a linear line and the resulting slope is listed on the plots. Plot **(a)** shows the potential range from -0.4 to -1.9 V, **(b)** shows the potential range from -0.4 to -1.95 V, **(c)** shows the potential range from -0.4 to -2.0 V, **(d)** shows the potential range from -0.4 to -2.05 V, and **(e)** shows the potential range from -0.4 to -2.1 V.

In both cyclic voltammograms of the gold film and the copperUPD-gold film, there is a consistent shape. The SH intensity shows a similar behavior as the electrodes are cycled in the perspective potential ranges. However, there are differences that are worth noting from the CV and observed SH behavior. By adding a copper overlayer on the evaporated gold film, there is a shift in potential needed to reductively desorb an alkanethiol. For a gold electrode, the maximum cathodic potential scanned is -1.95 V, while for a copperUPD-gold electrode, the potential is scanned to -2.1 V. Given the differences in potential, there is also a great difference in current densities. This is due to the hydrogen evolution reaction (HER). Since more negative potentials are necessary for the desorption process on a copperUPD-gold electrode, there is a greater overlap with the HER and greater possibility of the formation of bubbles at the electrode surface. Another notable difference, is the slope difference in the first region of the CV for both electrodes. The SH in this region coincides with the reduction and oxidation of the corresponding metals. For the copperUPD-gold electrode, there is a greater change in slopes in this region compared to the gold electrode. These are observations that should be noted when analyzing the SH due to the reductive desorption of alkanethiols from both electrodes.

4.3.2 Contact Angle

The water contact angle (CA) of both the gold film and copperUPD-gold film were measured. Figure 4.3 shows the contact angle images of a gold film and a copperUPD-

gold film. The gold film has two measurements. The first image (a) is from a gold film washed with ethyl alcohol 200 proof and is referred to as bare gold. The second image (b) is of an electrochemically cleaned gold film, which was cycled ten times in 0.1M H_2SO_4 with a scan rate of 50 mV/s. The gold film is referred to as cycled gold. The copperUPD-gold film (b) was washed with ultra-pure water and dried with nitrogen.
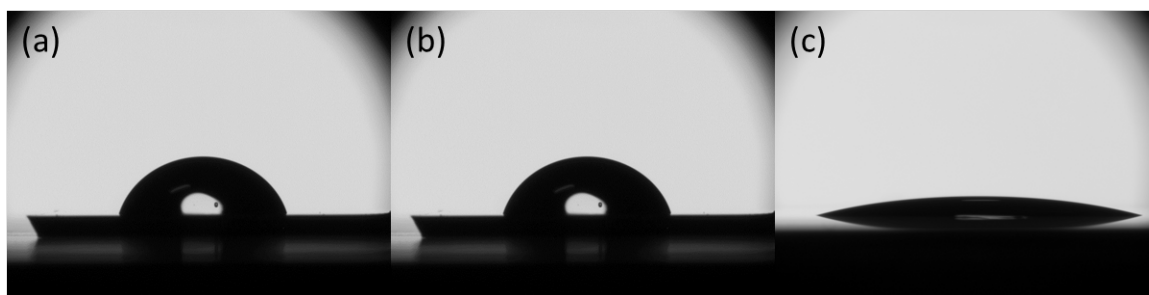
Figure 4.3 Water contact angle images of **(a)** bare gold, **(b)** cycled gold, and **(c)** copperUPD-gold.

From the CA images, there is a visible contrast between the wettability of a gold surface and a copperUPD-gold surface. The static contact angle of the gold film whether electrochemically cleaned or not is 69°. The copper UPD layer on the gold film has a static contact angle of 14°. Though CA does not show a difference between cleaning methods of a gold film, there is clear evidence of the gold being altered by the UPD of copper. The drastic difference in CA can be attributed to the effect of oxidation.[1] Compared to gold, copper is easily oxidized in atmosphere, which can lead to surface roughening and the adsorption of contaminations.

4.3.3 Sum Frequency Generation

Sum frequency generation (SFG) spectroscopy was used as a supplemental technique to check the order of a self-assembled monolayer before and after electrodesorption. Prior to the formation of a SAM of alkanethiols, the gold films and copperUPD-gold film were scanned from 2775 to 3060 cm^{-1}. The spectra from all three substrates are shown in Figure 4.4. The plots are stacked and separated by an arbitrary value for clarity.
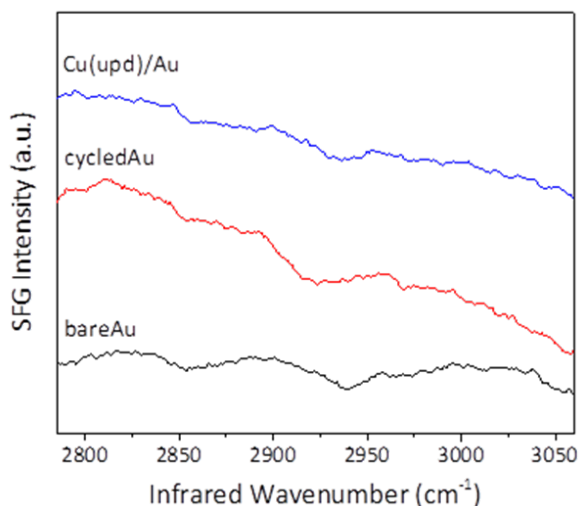
Figure 4.4 SFG spectra of a bare gold substrate, an electrochemically clean gold substrate, referred to as cycled gold, and a copper UPD layer on gold.

The SFG spectra above shows broad dips for all three samples suggesting trace amounts of impurities for all films. Similarly to contact angle measurements, no clear difference is seen between a bare gold and a cycled gold sample.

4.3.4 X-ray Photoelectron Spectroscopy

Ex-situ x-ray photoelectron spectroscopy (XPS) was used to identify elements present at the surface, to verify the deposition of copper onto a gold film, and to confirm a thiolate bond with the metal electrode. Figure 4.5 shows the high resolution XPS spectra for four elements. Binding energies were referenced to Au($4f_{7/2}$) at 84 eV.[1] Across all three samples, the gold $4f_{7/2}$ and $4f_{5/2}$ peaks are consistent and are shown in Figure 4.5 (a).[13-14] In the high resolution copper 2p region, Figure 4.5 (b), only the copperUPD-gold sample showed copper peaks, which was expected. The copper UPD sample has two peaks at 932.3 and 952.0 eV, which correspond to the Cu($2p_{3/2}$) and Cu($2p_{1/2}$) positions, respectively.[1, 6, 8, 12, 15] In the Cu(2p) spectra for the copperUPD-gold sample, there is a broad shoulder centered around 944 eV. This region of the spectra was magnified by 10 to show the satellite peak, which points to a Cu(I) oxidation state.[15-16]
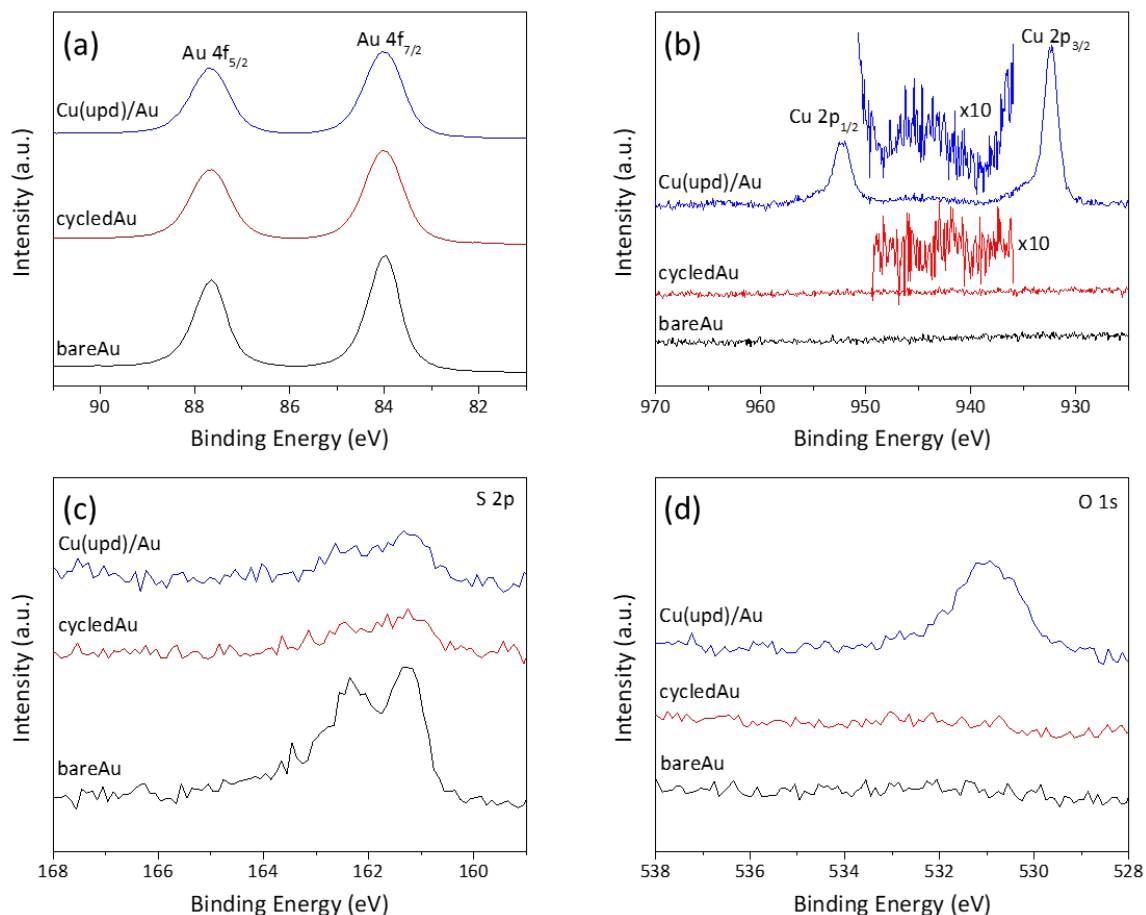
Figure 4.5 XPS spectra of a bare gold substrate, an electrochemically clean gold substrate, referred to as cycled gold, and a copper UPD layer on gold. The high resolution spectra of **(a)** gold, **(b)** copper, **(c)** sulfur, and **(d)** oxygen.

The high resolution sulfur region shows trace impurities of sulfur on all surfaces with a bare gold film having a more defined $2p_{3/2}$ peak. This is in agreement with the SFG spectra in Figure 4.4, which showed trace organic impurities. However, unlike the SFG spectra, a difference is seen between the bare gold and cycled gold substrates. This suggests the benefit of electrochemically cleaning a gold film. The oxygen 1s region showed a peak at around 531 eV on the copperUPD-gold sample, which corresponds to the existence of Cu(I) oxide suggested in the copper 2p spectra.[1]

4.4 In-situ Second Harmonic Generation of Alkanethiol Electrodesorption

Simultaneously acquired CV and SHG data was used to analyze the reductive desorption of alkanethiols from both gold and copperUPD-gold electrodes. Three alkanethiols were used to determine the effects of short and long chains. The short chain alkanethiols were 1-decanethiol (DT) and 1-dodecanethiol (DDT). The long chain alkanethiol studied was 1-octadecanethiol (ODT). From in-situ SHG, the behavior of the substrate was examined as the electrodesorption of the alkanethiols occurred. Over a total of 30 scans, SHG gradually changed and in most cases eventually mimicked that of a bare substrate prior to alkanethiol adsorption suggesting complete removal.

The following sections will show four representative scans of both the SHG and CV data for all three alkanethiols. Each figure will show a side by side comparison between a gold and copperUPD-gold electrode for each scan. The left column corresponds to the gold electrode and the right column corresponds to the copperUPD-gold electrode. The CVs and real time SHG were plotted in a double y-axis plot to directly compare the SH behavior as the potential was cycled. The left hand y-axis is current density in $\mu A/cm^2$ for the voltammogram shown as a solid black curve. For the copperUPD-gold electrode, the region from -0.4 to -1.8 V is magnified by five times. The blue dashed curve is the zoomed cathodic curve of the CV and the red dotted curve is the zoomed anodic curve of the CV. The right hand y-axis is the normalized SH intensity. The blue solid curve represents the SH along the cathodic curve and the red solid curve represents the SH along the anodic curve. All data is shown as a function of potential (V) with respect to a MSE.

79

All alkanethiol solutions were prepared to a concentration of 5mM with ethyl alcohol 200 proof. Gold electrodes were immersed for 24 hours, while the copperUPD-gold electrode was only immersed for 3 hours. The copperUPD-gold electrode was only immersed for 3 hours due to the possibility of the dissolution of the copper metal, which would result in discoloration and pitting.[16] Samples were removed from solution, rinsed thoroughly with ethanol, dried with nitrogen, and immediately placed in the PTFE cell. The cell was filled with 1M KOH and degassed for a minimum of 30 minutes.

4.4.1 1-decanethiol

For a short chain reference, 1-decanethiol (DT) was used. Real time SHG was monitored as cyclic voltammograms were recorded. For gold electrodes, the potential range was -0.4 to -1.85 V for all scans. For copperUPD-gold electrodes, the potential range was -0.4 to -2.0 V for the first 5 scans, then -0.4 to -1.95 V for scans 6-10, and then -0.4 to -1.9 V for scans 11-30. The shift in potential range for a copperUPD-gold electrode was to avoid the formation of bubbles on the electrode surface due to the hydrogen evolution reaction (HER). Figure 4.6 shows the data for the reductive desorption of DT from both a gold and copperUPD-gold electrode for scans 1, 3, 10, and 30. A total of 30 scans were cycled to complete the desorption process.

First, the focus will be on the gold electrode. In Figure 4.6 (a), the first reductive desorption scan shows a double desorption peak of DT starting at -1.4 V. This corresponds with results from literature.[17] As the potential is continually cycled, the desorption peak

decreases in intensity and shifts to more anodic potentials. There is also an increase in the HER. From the SH, the intensity begins to decrease at the first reductive desorption peak, and as the potential is reversed at -1.85 V, the SH intensity increases and plateaus at -1.3 V of the anodic scan (solid red curve). Scans 3, 10, and 30 are shown in Figure 4.6 (b), (c), and (d), respectively. There are noticeable changes not only in the CVs but also the SH. As the potential is continually cycled, the CV and SH begin to resemble the results of a bare gold substrate in KOH, from Figure 4.1 (a). This indicates that a significant amount of DT had been removed from the gold surface. To verify this statement, further sample examination was conducted using supplementary techniques.

Compared with the gold substrate, the copperUPD-gold substrate behaved differently. The CVs from Figure 4.6 (e), (f), (g), and (h) showed no obvious signs of desorption except for a broad shoulder seen around -1.85 V in the first scan, which overlaps with the HER. This signified a shift in desorption potential between the gold and copperUPD-gold electrode. For the most part, the CVs resembled that of a blank copperUPD-gold electrode in 1M KOH seen in Figure 4.2. As seen from the zoomed region of the CV, the first scan (b) showed features that did not resemble that of a bare electrode, but this was also noticeable in the SH behavior.

Figure 4.6 Real time SHG and CV plots of the reductive desorption of DT from a gold and copperUPD-gold electrode in 1M KOH. The solid black curves are the CV. The solid blue and red curves are the SH intensity corresponding to the cathodic and anodic scans, respectively. The SH intensity in each plot was divided in three sections where a slop change was observed. For a gold electrode, scans 1, 3, 10, and 30 are shown in **(a)**, **(b)**, **(c)**, and **(d)**, respectively. For a copperUPD-gold substrate, scans 1, 3, 10, and 30 are shown in **(e)**, **(f)**, **(g)**, and **(h)**, respectively. The region between -0.4 to -1.8 V is magnified by 5 times. The dashed blue curve is the zoomed cathodic region and the dotted red curve is the zoomed anodic region. Scan Rate: 20 mV/s.

While the CVs from the copperUPD-gold revealed no clear signs of electrodesorption, the SH behaved similarly to that of DT on a gold substrate, which suggested that desorption was occurring. For the copperUPD-gold samples, the supplemental techniques further verified the presence and stripping of DT. The absence of electrodesorption peaks in the CV may be due to the overlapping of the electrodesorption process with the HER.[18] As more negative potentials are applied to the system, alkanethiol is stripped from the surface and the copperUPD layer is exposed. The once protected copperUPD layer is now in contact with the electrolyte, which provided a good environment for the HER to occur.[18] Despite the lack of information from the CVs show, the SH suggested that electrodesorption was occurring in comparison with that of a gold electrode.

For a more direct comparison, the double plots from both electrodes were overlaid. Figure 4.7 shows both the CV and SH data for both a gold and copperUPD-gold electrode. The solid curves represent the gold electrode, and the dashed curves are for a copperUPD-gold electrode. The black curves are the CVs and the blue and red curves are the SH intensity corresponding to the cathodic and anodic scans, respectively. Scans 1, 3, 5, and 10 are shown below in (a), (b), (c), and (d), respectively. The CVs from the gold electrode in (b), (c), and (d) were magnified by 5 times.
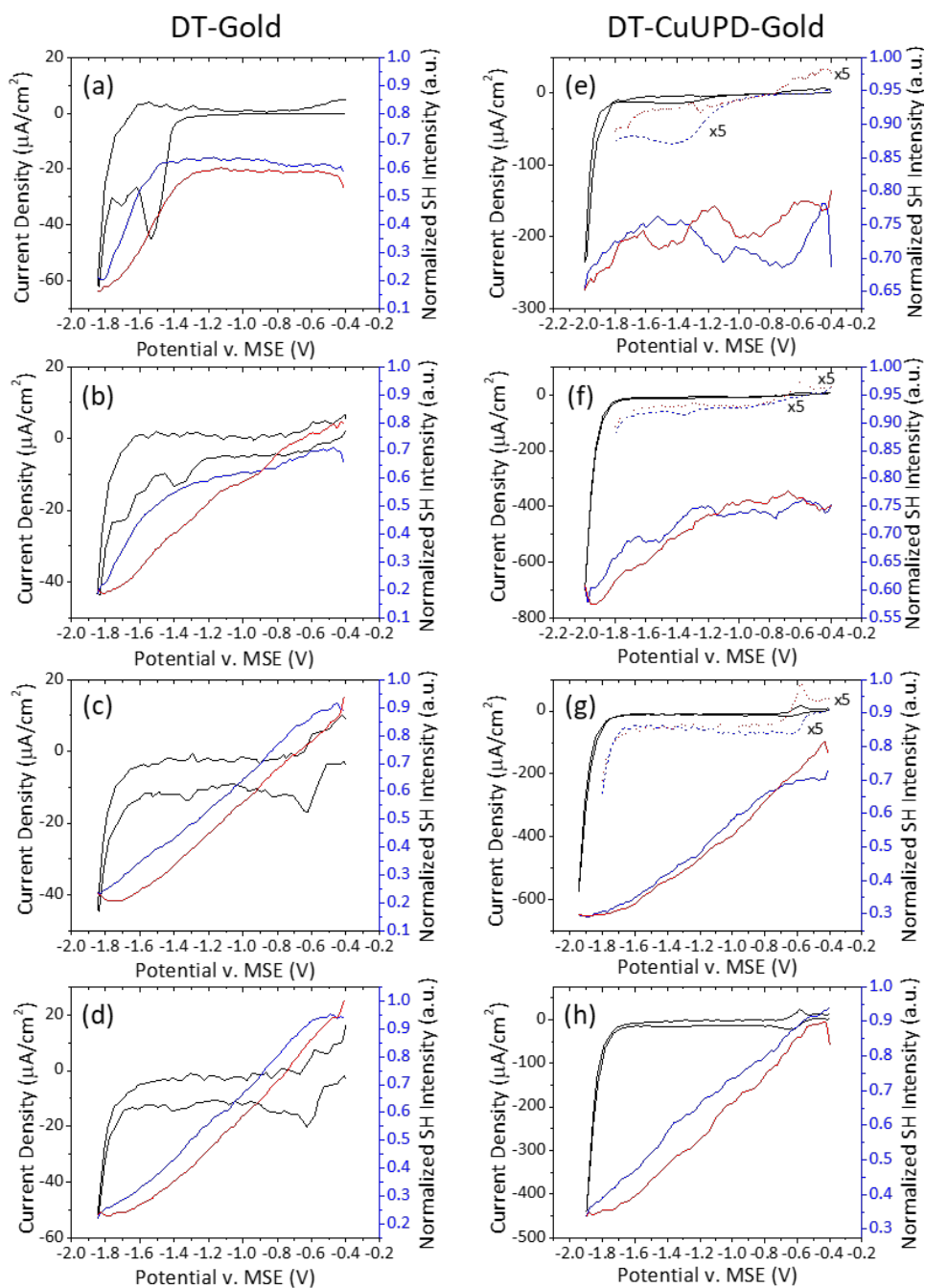
Figure 4.7 Real time SHG and CV plots of the reductive desorption of DT from both a gold and copperUPD-gold electrode in 1M KOH. The (---) curves correspond to a copperUPD-gold electrode, and the (—) curves correspond to a gold electrode. The black curves are the CVs. The blue and red curves are the SH intensity for the cathodic and anodic scans, respectively. Scans 1, 3, 5, and 10 are shown in **(a)**, **(b)**, **(c)**, and **(d)**, respectively. Scan Rate: 20 mV/s.

In all scans, there is an evident difference between the CVs from a gold and copperUPD-gold electrode. Only the CVs from a gold electrode showed clear desorption peaks. However, the SH behaved similarly by returning to a linear trend representative of a bare electrode, shown in Figure 4.7 (d). Though they both are linear independently, there are visible differences between electrodes. The biggest difference is the gap between the cathodic and anodic scans for each electrode. For the gold electrode, there is a defined separation between the SH. While for the copperUPD-gold electrode, the SH

of the cathodic and anodic scans are almost overlapping. This difference is also evident in the CVs. With a lack of desorption features in the CV, the electrodes are assumed to be thiol free, which would result in the charging of bare electrodes. Therefore, the difference in SH could be correlated to the charging of the electrode.

4.4.2 1-octadecanethiol

For a long chain reference, 1-octadecanethiol (ODT) was used. From literature, when a long chain alkanethiol is electrodesorbed, it remains near the surface of the electrode and in turn is readsorbed to the electrode.[19] Through real time SHG, the behavior of ODT during the electrodesorption process was observed and compared with that of DT.

For gold electrodes, the potential range was -0.4 to -1.95 V for the first five scans, -0.4 to -1.9 V for scans 6-10, and then -0.4 to -1.85V for scans 11-30. For copperUPD-gold electrodes, the potential range was -0.4 to -2.1 V for the first 5 scans, then -0.4 to -2.05 V for scans 6-10, and then -0.4 to -2.0 V for scans 11-30. Results from CV scans 1, 3, 10, and 30 are shown below in Figure 4.8 for both a gold and copperUPD-gold electrode. The first column are the representative CV scans for the gold electrode, while the second column shows the CV data for copperUPD-gold electrode.
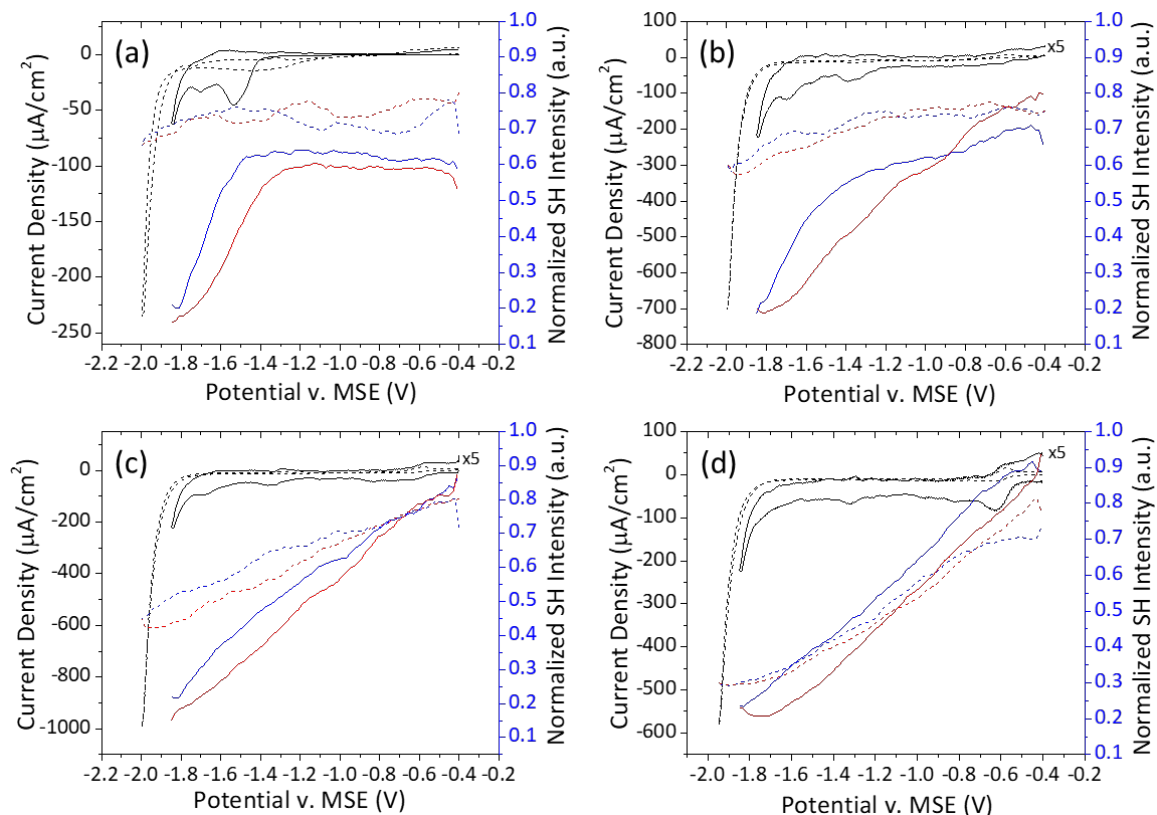
Figure 4.8 Real time SHG and CV plots of the reductive desorption of ODT from a gold and copperUPD-gold electrode in 1M KOH. The solid black curves are the CV. For a gold electrode, the region between -0.4 to -1.6 V is magnified by 10 times. For a copperUPD-gold electrode, the region between -0.4 to -1.8 V is magnified by 5 times. The dashed blue curve is the zoomed cathodic region and the dotted red curve is the zoomed anodic region. The solid blue and red curves are the SH intensity corresponding to the cathodic and anodic scans, respectively. For a gold electrode, scans 1, 3, 10, and 30 are shown in **(a)**, **(b)**, **(c)**, and **(d)**, respectively. For a copperUPD-gold substrate, scans 1, 3, 10, and 30 are shown in **(e)**, **(f)**, **(g)**, and **(h)**, respectively. Scan Rate: 20 mV/s.

In Figure 4.8 (a), the first reductive desorption scan of ODT from a gold electrode is shown. The CV shows an electrodesorption peak at around -1.85 V followed with a second peak at -2.1 V, which corresponds to the onset of hydrogen evolution. With the electrodesorption potential of ODT being close to the HER, after the first scan, all evidence of desorption from the CV scans vanishes. However, the SH behaves relatively the same in all representative scans shown in the left column of Figure 4.8. The SH begins at -0.4 V as a blue curve and begins to decrease at -1.65 V. At -1.95 V, the SH intensity (now a red curve) decreases for less than 0.1 V then gradually increases until -1.35 V where it plateaus for the remainder of the CV. Unlike DT, the SH intensity for ODT never returns to a linear curve representative of a bare gold electrode from Figure 4.1. This leads to the belief that though the first CV cycle shows a desorption peak, ODT is very much still near the surface of the gold electrode. This is also in agreement with literature.[19-21]

For a copperUPD-gold electrode, ODT once again behaves differently than DT, which is to be expected given the difference in chain length.[19-21] In the right column of Figure 4.8 (e), (f), (g), and (h), the CV cycles 1, 3, 10, and 30 are shown as representatives of the reductive desorption of ODT from a copperUPD-gold electrode, respectively. The region from -0.4 to -0.8 V is magnified by five to be able to relate any changes in the SH to features in the CV. All four CV scans show no desorption features, which is similar to DT on a copperUPD-gold electrode from Figure 4.6. Again, this is due to the overlap of the desorption peak with the HER.[18] For the SH intensity, though noisy, there are no clear features. The SH is considered to remain essentially constant throughout both the

cathodic and anodic curves. Though the SH behaves differently than that for the gold electrode, the SH intensity is consistent among all four CV cycles, which points to the assumption that ODT is not electrodesorbed from the copperUPD-gold electrode. This will be shown in the following results.

Figure 4.9 shows the overlapped CV and SH data for both a gold and copperUPD-gold electrode. The solid curves represent the gold electrode, and the dashed curves are for a copperUPD-gold electrode. The black curves are the CVs and the blue and red curves are the SH intensity corresponding to the cathodic and anodic scans, respectively. Scans 1, 3, 5, and 10 are shown below in (a), (b), (c), and (d), respectively.
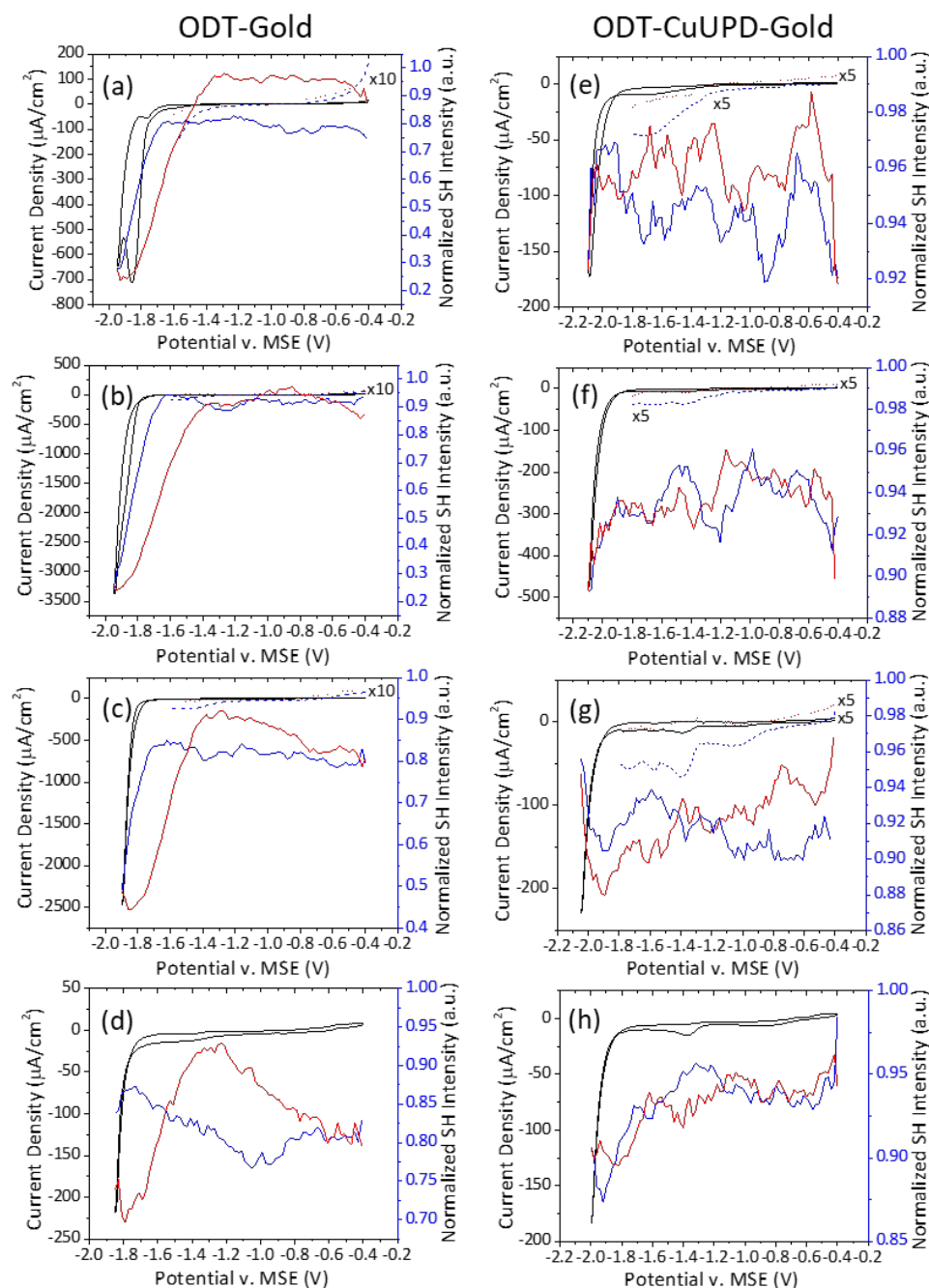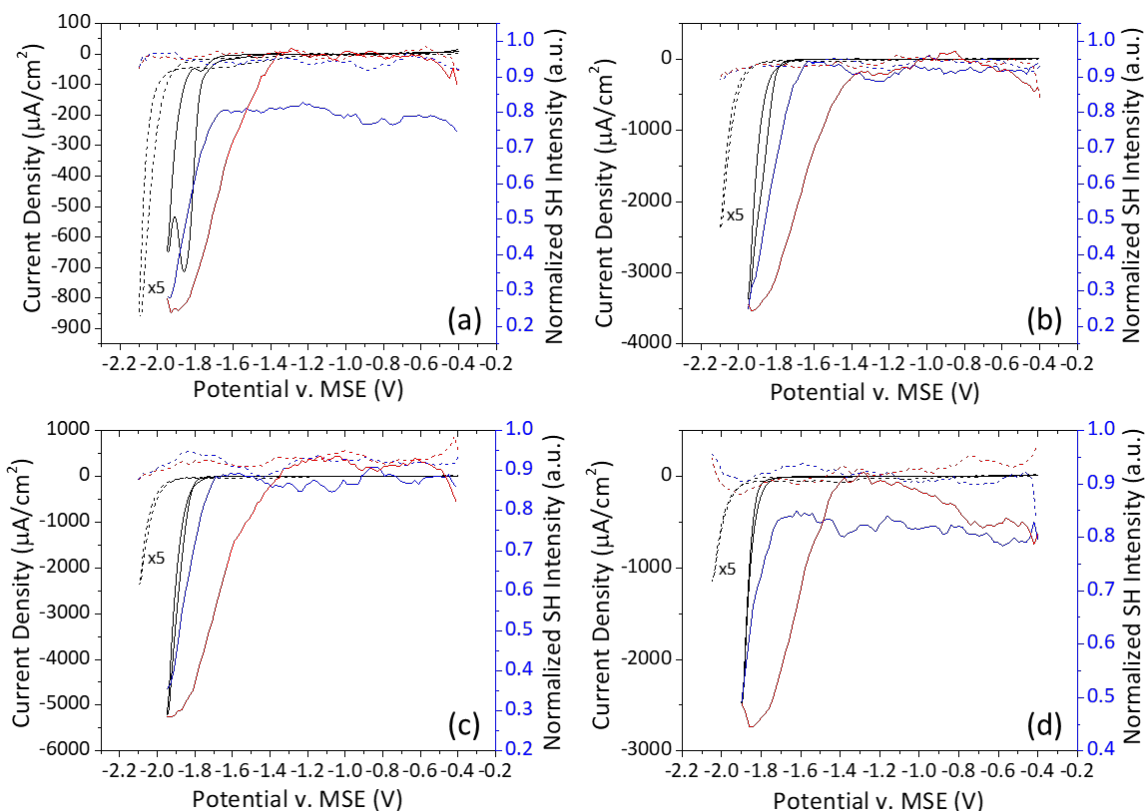
Figure 4.9 Real time SHG and CV plots of the reductive desorption of ODT from both a gold and copperUPD-gold electrode in 1M KOH. The (---) curves correspond to a copperUPD-gold electrode, and the (—) curves correspond to a gold electrode. The black curves are the CVs. The blue and red curves are the SH intensity for the cathodic and anodic scans, respectively. Scans 1, 3, 5, and 10 are shown in **(a)**, **(b)**, **(c)**, and **(d)**, respectively. Scan Rate: 20 mV/s.

The most noticeable difference is seen between the SH from both electrodes. While there are differences between electrodes, there is consistency between cycle numbers. As more CVs are collected, the SH shows a similar shape. For a gold electrode, the SH begins to decrease near the electrodesorption potential and then increases and eventually plateaus returning to the shape of the cathodic scan. From DT, the decrease and increase correspond to the electrodesorption process, where the SH eventually became linear similar to that of a bare electrode. For ODT, the SH never resembles a linear

curve, which implies that the alkanethiol remains near the surface. However, due to the decrease and increase in SH, the question of how the alkanethiol is interacting with the electrode surface was considered. With the consistency of the SH behavior among all four representative scans and the lack of desorption features after the first scan, the SH suggests influence from the ODT monolayer, while the CV implies that the ODT monolayer is no longer chemisorbed to the gold electrode. This is in agreement with literature.[19-21]

For the copperUPD-gold electrode, the SH intensity never showed any sharp decreases or increases. At the scale in Figure 4.9, the SH resembles a constant line for all representative scans. The consistency of SH between each scan indicates a SAM was still present. Though the SH remains unchanged for both electrodes, there is a noticeable difference in SH behavior between the electrodes, which was not seen from bare electrodes. This suggests a difference in the thiolates binding to the electrodes or their monolayer structure.

4.4.3 1-dodecanethiol

Frequently referred to as the turning point between short and long chain alkanethiols, 1-dodecanethiol (DDT) was chosen as the third and final SAM.[19] Interestingly, for DDT, the copperUPD-gold electrode seemed to stabilize the SAM and allowed DDT to remain intact at the surface compared to a gold electrode where DDT was easily electrodesorbed. With in situ SHG, the real time reductive desorption process was monitored and analyzed.

For gold electrodes, the potential range was -0.4 to -1.85 V for all scans. For copper-gold electrodes, the potential range was -0.4 to -2.0 V for the first 5 scans, then -0.4 to -1.95 V for scans 6-10, and then -0.4 to -1.9 V for scans 11-30. In Figure 4.18, the data shown represent CV scans 1, 3, 10, and 30 for both a gold and copperUPD-gold electrode. The first column is results for a gold electrode, while the second column shows the results for a copperUPD-gold electrode.

91

Figure 4.10 Real time SHG and CV plots of the reductive desorption of DDT from a gold and copperUPD-gold electrode in 1M KOH. The solid black curves are the CV. The solid blue and red curves are the SH intensity corresponding to the cathodic and anodic scans, respectively. For a gold electrode, scans 1, 3, 5, and 10 are shown in **(a)**, **(c)**, **(e)**, and **(g)**, respectively. For a copperUPD-gold substrate, scans 1, 3, 5, and 10 are shown in **(b)**, **(d)**, **(f)**, and **(h)**, respectively. The region between -0.4 to -1.8 V is magnified by 5 times. The dashed blue curve is the zoomed cathodic region and the dotted red curve is the zoomed anodic region. Scan Rate: 20 mV/s.

The first CV cycle of DDT on gold is shown in Figure 4.10 (a). The CV scan shows a small, broad desorption peak at -1.6 V followed by a broad shoulder at -1.8 V. For CV scans 3, 10, and3, the cyclic voltammograms show no evidence of remaining DDT. The drastic disappearance of reductive desorption peaks can be due to both the electrodesorption of DDT and the overlap with the HER. It also can be proof of a fast desorption process.[19]

For the first reductive desorption CV, the SH intensity for the cathodic curve, represented by a blue solid line, starts constant at -0.4 V and then gradually decreases at -1.65 V. At -1.85 V, the SH intensity of the anodic curve, the red solid curve, continues to decrease for 0.05 V, then gradually increases until -1.35 V where the SH then returns to a constant. This behavior resembles that of ODT on a gold electrode shown in Figure 4.8 (a). However, unlike ODT, as the amount of CV cycles continues, the SH becomes linear similarly to a blank gold electrode seen in Figure 4.1. This change in SH intensity is analogous to DT on a gold electrode.

DDT monolayers on a gold electrode have traits similar to both DT and ODT. On the other hand, the behavior of DDT monolayers on a copperUPD-gold electrode mimics that of ODT. Similarly to all alkanethiol monolayers on the copperUPD-gold electrode, the CV cycles show no signs of desorption. The SH intensity seems a bit unusual compared to the other alkanethiol monolayers, however, from the zoomed region of the CV, there are small features that could correspond with the SH.

The overlapped CV and SH data for both a gold and copperUPD-gold electrode are shown in Figure 4.11. The solid curves represent the gold electrode, and the dashed curves are for a copperUPD-gold electrode. The black curves are the CVs and the blue and red curves are the SH intensity corresponding to the cathodic and anodic scans, respectively. Scans 1, 3, 5, and 10 are shown below in (a), (b), (c), and (d), respectively.
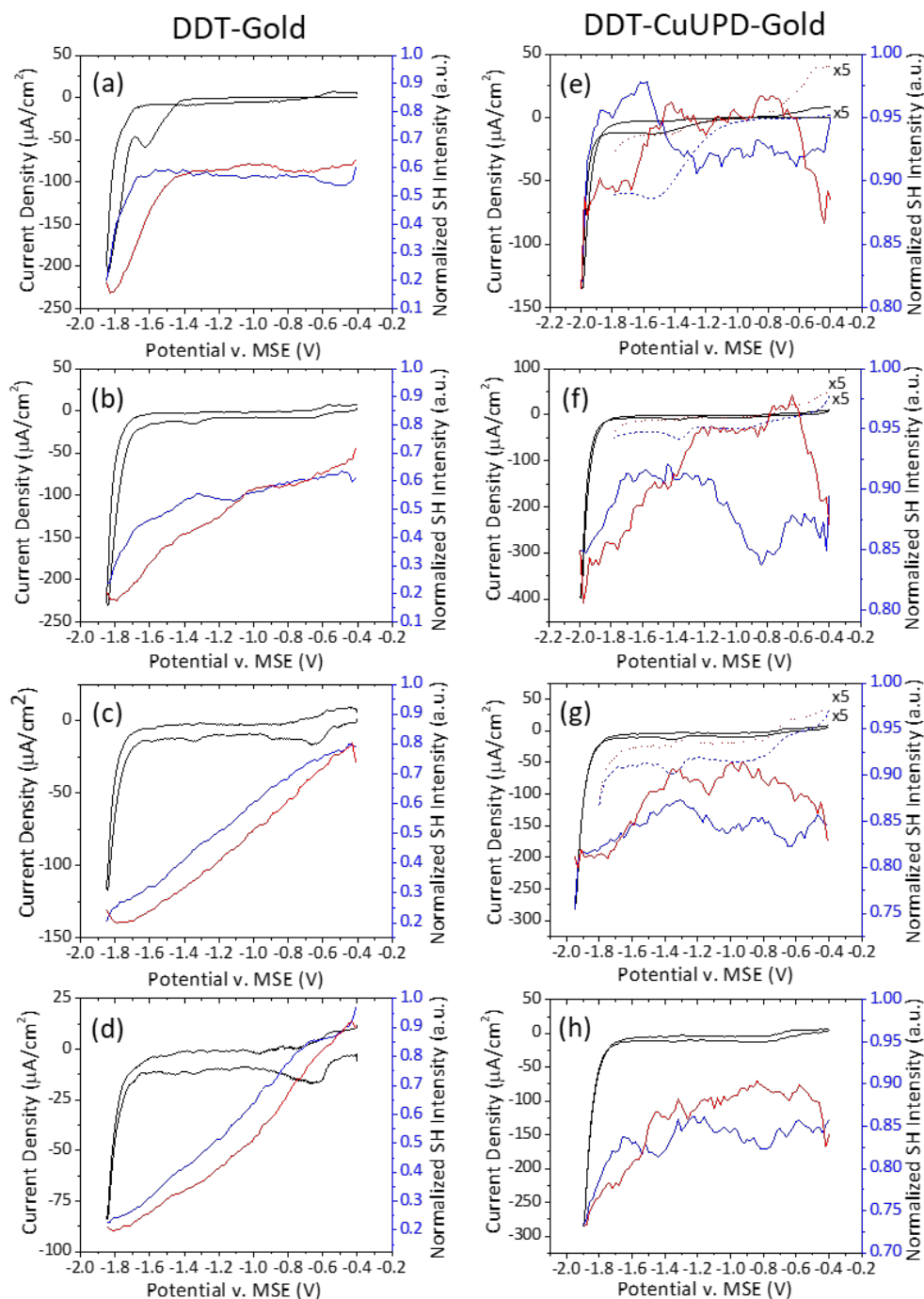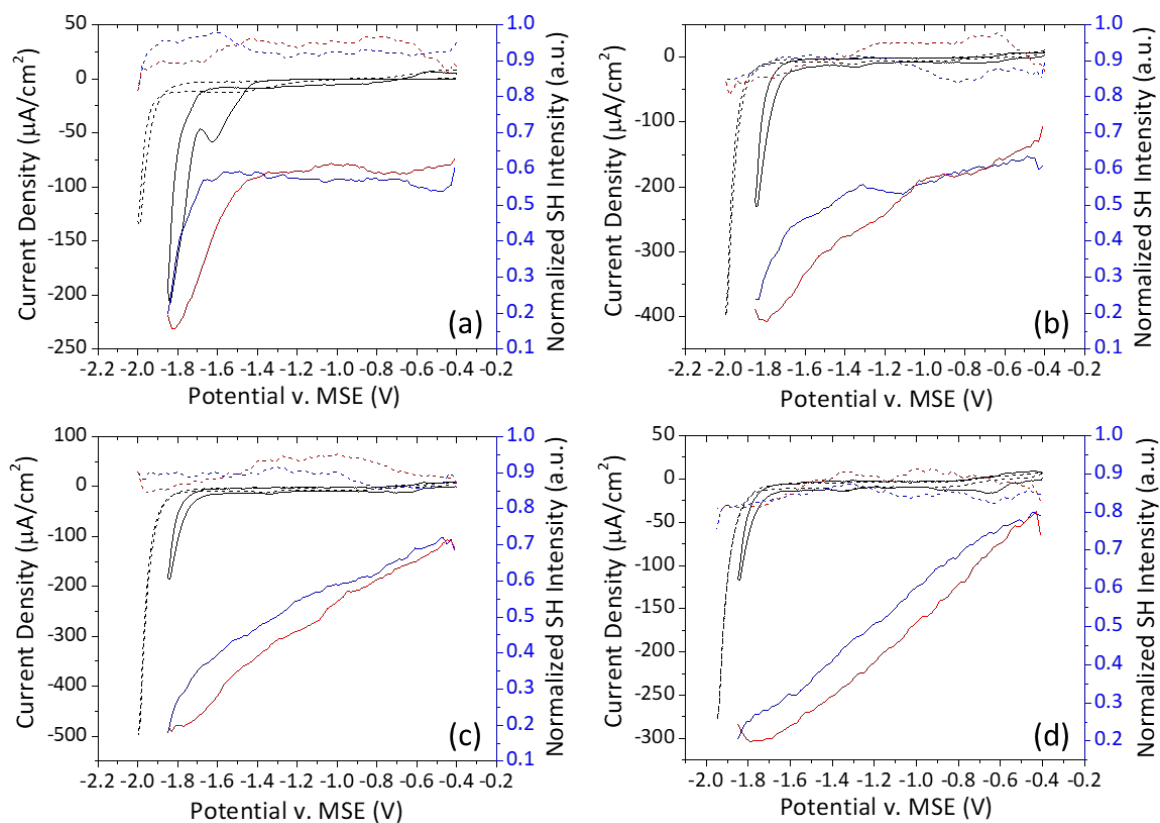

Figure 4.11 Real time SHG and CV plots of the reductive desorption of DDT from both a gold and copperUPD-gold electrode in 1M KOH. The (---) curves correspond to a copperUPD-gold electrode, and the (—) curves correspond to a gold electrode. The black curves are the CVs. The blue and red curves are the SH intensity for the cathodic and anodic scans, respectively. Scans 1, 3, 5, and 10 are shown in **(a)**, **(b)**, **(c)**, and **(d)**, respectively. Scan Rate: 20 mV/s.

From Figure 4.11, a drastic difference is seen between the SH from a gold and copperUPD-gold electrode. For a gold electrode, the SH behaves similarly to that for a DT monolayer on a gold electrode where over ten scans the SH becomes linear resembling that of a bare electrode. However, the SH for a copperUPD-gold electrode behaves similarly to that of an ODT monolayer on a copperUPD-gold electrode remaining overall constant in the given scale.

4.5 Sum Frequency Generation

SFG was used to check the alkanethiol monolayer prior and after the electrodesorption process. For additional information, samples were checked after every ten scans. This provided information about the intermediate stages for all monolayers. The normalized SFG spectra is shown below for all alkanethiols on both a gold electrode and a copperUPD-gold electrode. Each spectra has two curves. The spectra before any surface modification is shown as black circles connected by a black solid line. The spectra after a given amount of CV scans (10, 20, or 30) are represented by red circles connected by a solid red line. Figures 4.12, 4.13, and 4.14 are for DT, ODT, and DDT, respectively.

All SFG spectra were taken with all beams set to a p-polarization, ppp. The observed modes are for the methyl and methylene C-H stretching. [20-25] Three dips are attributed to methyl resonances. The first dip at around 2875 cm^{-1} is assigned to the symmetric C-H stretch of the methyl group. The second dip around 2935 cm^{-1} is attributed to the Fermi resonances between the symmetric mode and the overtone of the bending

mode of the methyl group. The last dip at 2960 cm^{-1} is assigned to the methyl antisymmetric C-H stretch. Two remaining dips are attributed to the methylene symmetric C-H stretching and the Fermi resonance stretching modes at 2850 cm^{-1} and 2915 cm^{-1}, respectively. All three alkanethiols form well-ordered monolayers with an all-trans configuration. However, if methylene stretching modes are observed, this is an indicator of conformational disorder.[20, 23, 26-27] The presence of methylene stretching modes are seen in several SFG spectra after a number of CV scans, which is further implication of the disordering of monolayer and possible alkanethiol reduction.

4.5.1 1-decanethiol

For both the gold and copperUPD-gold electrode, there is a significant change of the peak shapes and intensities after 30 CV cycles. Figure 4.12 shows the SFG spectra of a DT monolayer on both electrodes with the left column corresponding to a gold electrode and the right column a copperUPD-gold electrode. From the SFG spectra before any CV cycles for a gold electrode, a well-ordered monolayer is expected due to the lack of methylene stretching modes. However, after just 10 CV cycles, (a) the SFG spectra, shown in red, shows the Fermi resonance of the methylene stretching mode around 2915 cm^{-1}. Similarly to the gold electrode, the SFG spectra of a DT monolayer on a copperUPD-gold electrode reveals a peak around 2915 cm^{-1}. The copperUPD-gold electrode also showed a peak at 2850 cm^{-1}, which was assigned to the methylene symmetric C-H stretching mode. These peak suggests a disordered monolayer, which can be a result of the

electrodesorption process. These results are in good agreement with the in-situ SHG in

Figure 4.6, which suggested that the DT monolayer was desorbed due to the return of the

SH to a linear curve.

Figure 4.12 Normalized SFG ppp spectra of DT on gold and copperUPD-gold before and after CV sweeps. The black circles connected with a solid black line are spectra before and the red circle connected with a solid red line are spectra after CV sweeps. The left column are spectra for DT-gold sample after **(a)** 10, **(b)** 20, and **(c)** 30 CV cycles. The right column are spectra for DT-copperUPD-gold sample after **(d)** 10, **(e)** 20, and **(f)** 30 CV cycles.

4.5.2 1-octadecanethiol

Figure 4.13 shows the SFG spectra of an ODT monolayer on both a gold and copperUPD-gold electrode. All spectra before any CV cycles for both electrodes showed a well-ordered monolayer with only the presence of methyl C-H stretching modes. Despite some anomalies to the SFG spectra after 10 and 20 CV cycles for a gold electrode, the SFG spectra after 30 CV cycles for both the gold and copperUPD-gold electrodes showed little change in the peak positions and intensities. There were also no peaks seen from the methylene C-H stretching modes. This implied a well-ordered ODT monolayer before and after 30 CV cycles. These results also were in good agreement with the in-situ SHG from Figure 4.8. Both the SFG and SHG remained unchanged during the electrodesorption process.

ODT-Gold

ODT-CuUPD-Gold

Figure 4.13 Normalized SFG ppp spectra of ODT on gold and copperUPD-gold before and after CV sweeps. The black circles connected with a solid black line are spectra before and the red circle connected with a solid red line are spectra after CV sweeps. The left column are spectra for ODT-gold sample after **(a)** 10, **(b)** 20, and **(c)** 30 CV cycles. The right column are spectra for DT-copperUPD-gold sample after **(d)** 10, **(e)** 20, and **(f)** 30 CV cycles.

4.4.3 1-dodecanethiol

The SFG spectra of DDT on a gold and copperUPD-gold electrode is shown in Figure 4.14. From the side by side comparison between a gold and copperUPD-gold electrode, there are clear differences between the SFG spectra after CV cycles. The DDT monolayer on a gold electrode behaves similarly to a DT monolayer with the presence of methylene C-H stretching modes after a number of CV cycles. This implies a disordered monolayer due to the electrodesorption process and is in good agreement with the in-situ SHG results from Figure 4.10.

Alternatively, the DDT monolayer on a copperUPD-gold electrode mimics the behavior of an ODT monolayer. In Figure 4.14 (f), after 30 CV cycles, the before and after SFG spectra are nearly identical. With only a few intensity differences, the spectra overall suggests a well-ordered monolayer. There is, however, a small peak at around 2915 cm^{-1}, which is representative of the Fermi resonance of the methylene C-H stretching. Though a sign of disorder, the SFG spectra overall suggests an ordered DDT monolayer after 30 CV cycles. The SFG spectra from both electrodes further points to the differing behavior of the monolayer based on substrate.
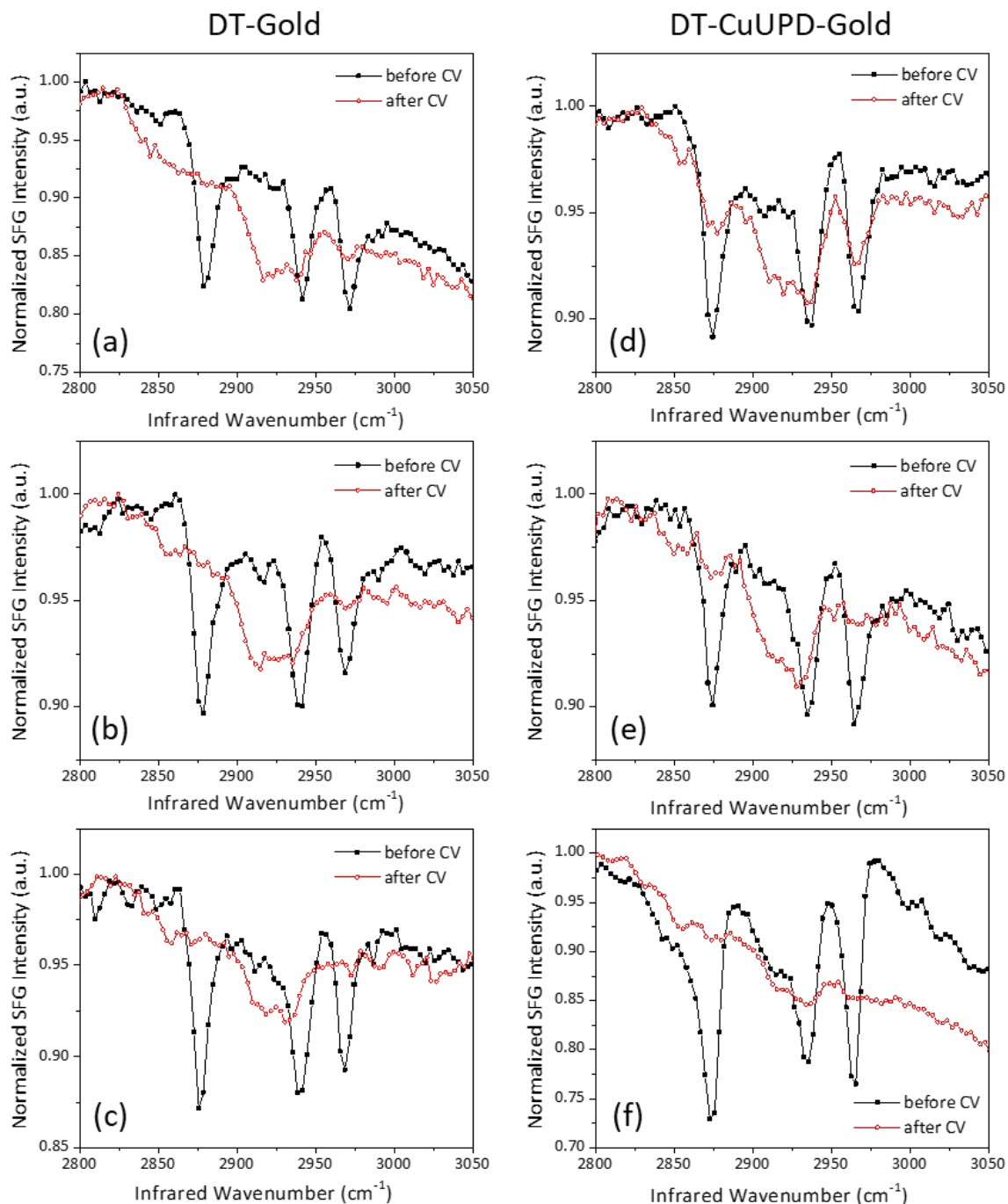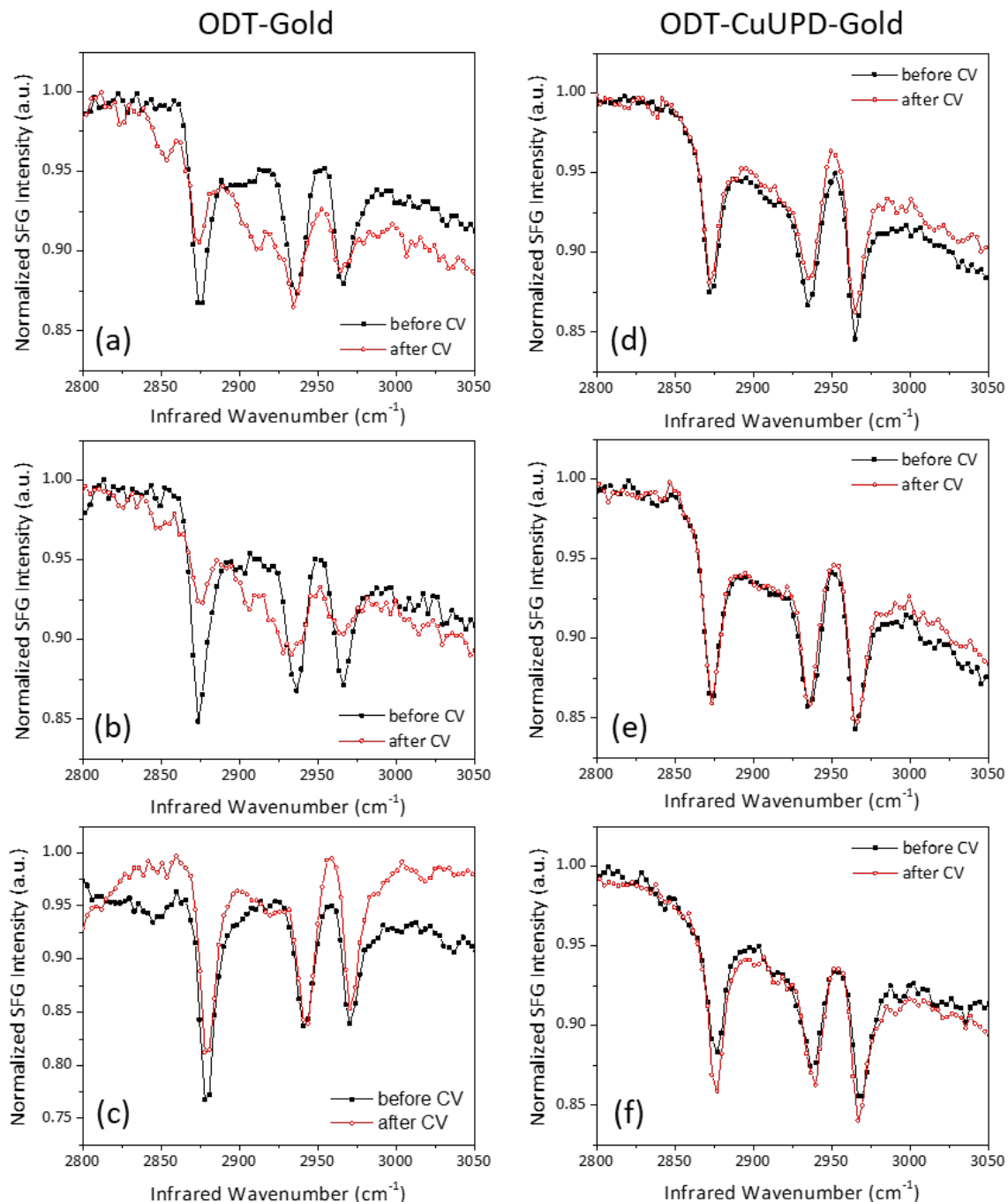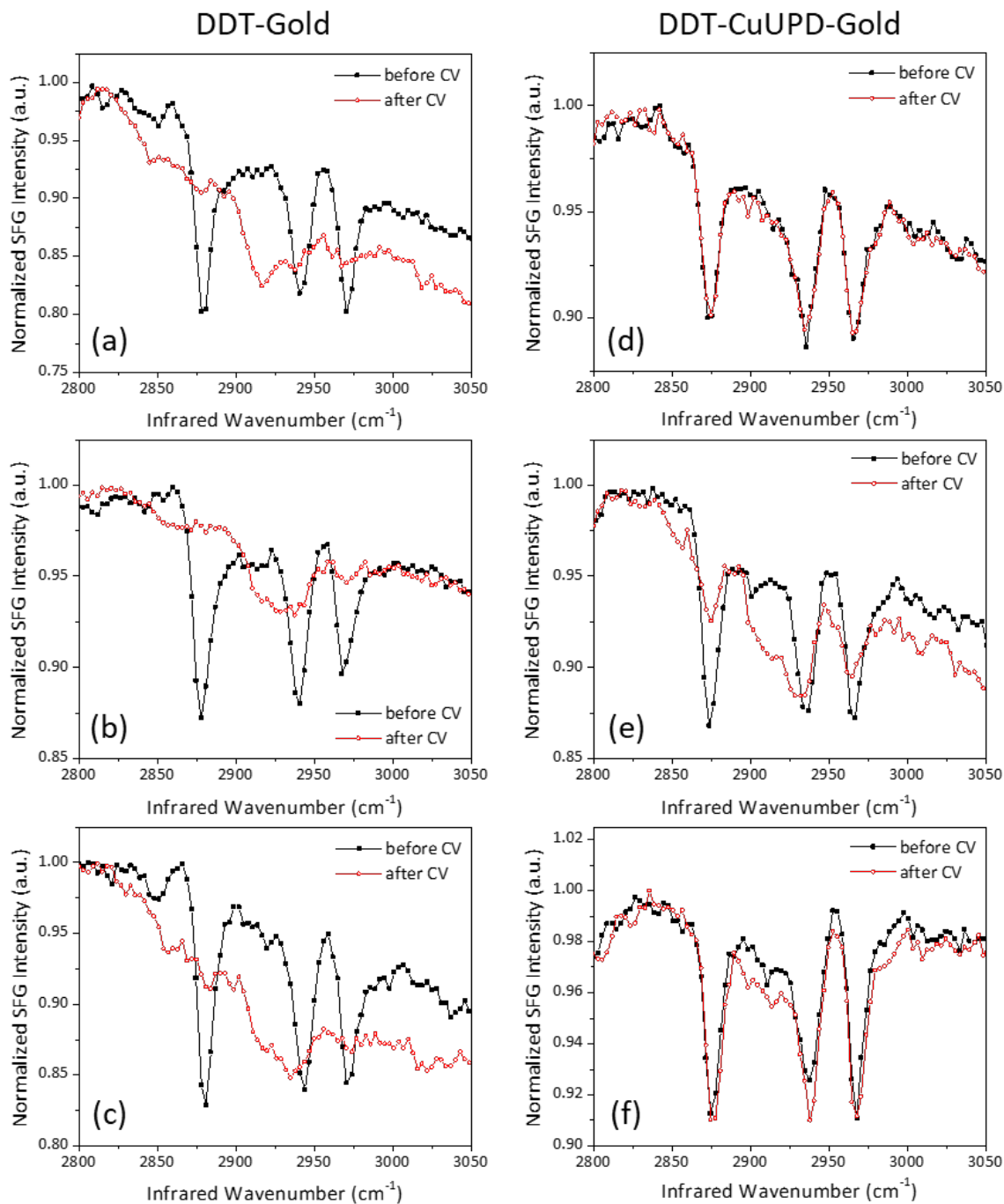
Figure 4.14 Normalized SFG ppp spectra of DDT on gold and copperUPD-gold before and after CV sweeps. The black circles connected with a solid black line are spectra before and the red circle connected with a solid red line are spectra after CV sweeps. The left column are spectra for DDT-gold sample after **(a)** 10, **(b)** 20, and **(c)** 30 CV cycles. The right column are spectra for DT-copperUPD-gold sample after **(d)** 10, **(e)** 20, and **(f)** 30 CV cycles.

4.6 X-ray Photoelectron Spectroscopy

Ex-situ XPS was used to determine the elemental composition of the samples before and after CV cycles. The following figures show the high resolution XPS spectra for gold, sulfur, oxygen, and copper, when present. Binding energies were referenced to Au(4f$_{7/2}$) at 84 eV.[1] Each XPS spectra contains the spectra before (black solid curve) and after (red solid curve) 30 CV cycles. All samples revealed two gold peaks in the 4f region corresponding to 4f$_{7/2}$ and 4f$_{5/2}$.[13-14] All copperUPD-gold samples had two peaks at about 932.6 and 952.4 eV, which correspond to the Cu(2p$_{3/2}$) and Cu(2p$_{1/2}$) positions, respectively.[1, 6, 8, 12, 15] These peaks can be assigned to Cu(0) or Cu(I), showing no additional features at 942 eV suggesting a presence of Cu(II) species.[28] Figure 4.15 shows the high resolution XPS spectra of the gold 4f and the copper 2p regions for a DT monolayer on a gold and copperUPD-gold electrode, respectively.
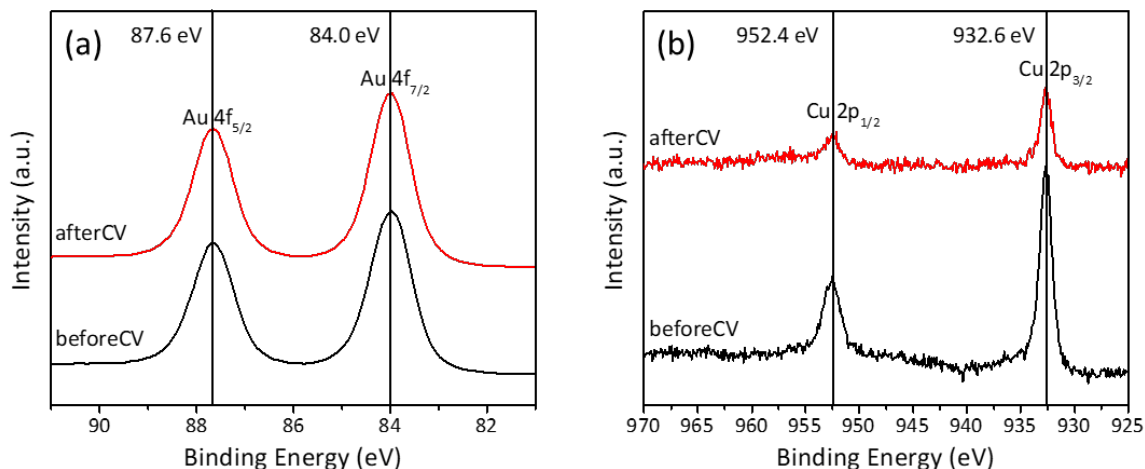
Figure 4.15 (a) High resolution x-ray photoelectron spectroscopy of the gold 4f region for a DT monolayer on a gold electrode. **(b)** High resolution x-ray photoelectron spectroscopy of the copper 2p region for a DT monolayer on a copperUPD-gold electrode. The black solid curve represents the spectrum of a fresh DT monolayer. The red solid curve represents the spectrum of a DT monolayer after 30 CV scans.

From literature, an alkanethiol monolayer on a gold electrode has a $S(2p_{3/2})$ peak at 161.9 eV, while an alkanethiol monolayer on a copper electrode has a $S(2p_{3/2})$ peak at 162.1 eV.[9, 11, 16, 29-30] These binding energies were observed for all alkanethiol monolayers on both a gold and copperUPD-gold electrode. Figure 4.16 (a) shows the high resolution XPS spectra of the sulfur 2p region for all samples with a fresh monolayer. The bottom three spectra are for a DT, DDT, and ODT monolayer on a gold electrode, labelled as A, B, and C, respectively. Spectra D, E, and F, are for a DT, DDT, and ODT monolayer on a copperUPD-gold electrode, respectively. Figure 4.16 (b) shows the high resolution XPS spectra of the sulfur 2p region for all samples after 30 CV scans. The spectra are ordered identically to Figure 4.16 (a). Each plot has two reference lines. The black line corresponds

to a binding energy for the gold electrodes and the red line corresponds to a binding

energy for a copperUPD-gold electrode.
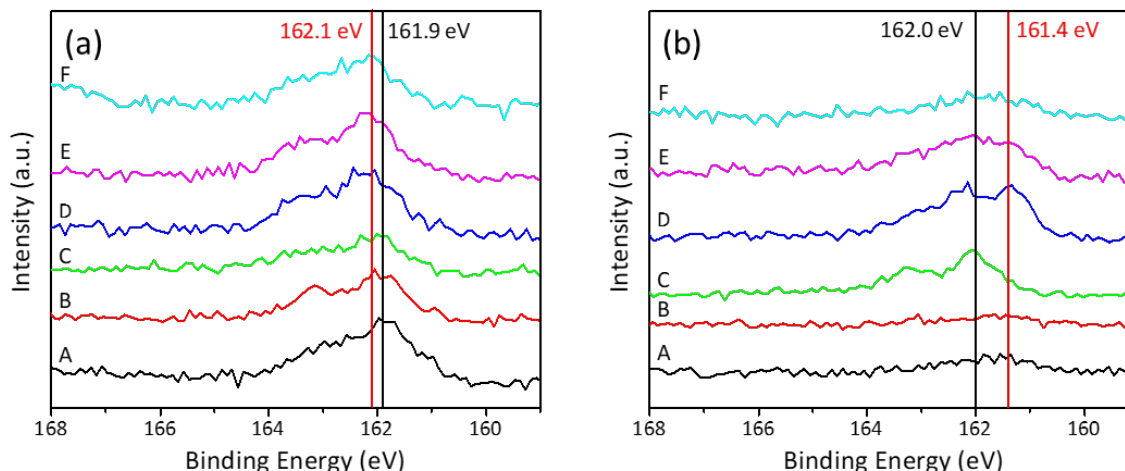
Figure 4.16 High resolution x-ray photoelectron spectroscopy of the sulfur 2p region **(a)** for a fresh monolayer before any CV scans, and **(b)** for a monolayer after 30 CV scans. **A**, **B**, and **C** correspond to a DT, DDT, and ODT monolayer on a gold electrode, respectively. **D**, **E**, and **F** represent a DT, DDT, and ODT monolayer on a copperUPD-gold electrode, respectively. The black reference lines reference a binding energy for a gold electrode and the red reference lines refer to a binding energy for a copperUPD-gold electrode.

Qualitatively, the sulfur $2p_{3/2}$ peaks in Figure 4.16 (a) show a shift to a higher

binding energy for the copperUPD-gold electrodes. This would suggest the binding of the

thiolates to the copperUPD layer and not the gold substrate. However, without further

analyzation this is only conjecture. After 30 CV scans, the sulfur $2p_{3/2}$ peaks for a DT and

DDT monolayer on a gold electrode lose any defining features and decrease in intensity,

shown in Figure 4.16 (b) spectrum A and B, respectively. In Figure 4.16 (b) spectrum C,

the ODT monolayer on a gold electrode shows a sulfur $2p_{3/2}$ peak indicating the presence

of an adsorbed thiolate. These results are in agreement with SHG and SFG, which suggest

the electrodesorption of DT and DDT monolayers but the existence of an ODT monolayer on the gold electrode. For a copperUPD-gold electrode, the sulfur 2p region shows a change in the features of the $2p_{3/2}$ peak for all three alkanethiols with the most pronounced features in the spectrum for a DT monolayer. These results are contrary to SHG and SFG results, which point to the removal of a DT monolayer but the presence of a DDT and ODT monolayer on the copperUPD-gold electrode. The change in the sulfur peak can be attributed to the disordering of the monolayer. Also, the quality of the SAMs formed on the copperUPD-gold substrate can be affected by the oxidation of the copperUPD adlayer.[1]

4.7 Contact Angle

The water contact angle of all alkanethiol monolayers on both a gold and copperUPD-gold electrode were measured. Contact angle images were taken on a fresh monolayer and the resulting monolayer after 30 CV cycles. Contact angles were measured using ImageJ and a contact angle plugin. Figure 4.17 shows the contact angle images for all samples. The contact angles measured 105°, 108°, and 107° for a fresh DT, DDT, and ODT monolayer on a gold electrode, respectively. For a copperUPD-gold electrode, the contact angles measured 102°, 103°, and 102° for a fresh DT, DDT, and ODT monolayer, respectively. These contact angles suggested a well-ordered alkanethiol monolayer on all electrodes.

Gold Electrode   **CuUPD-Gold Electrode**
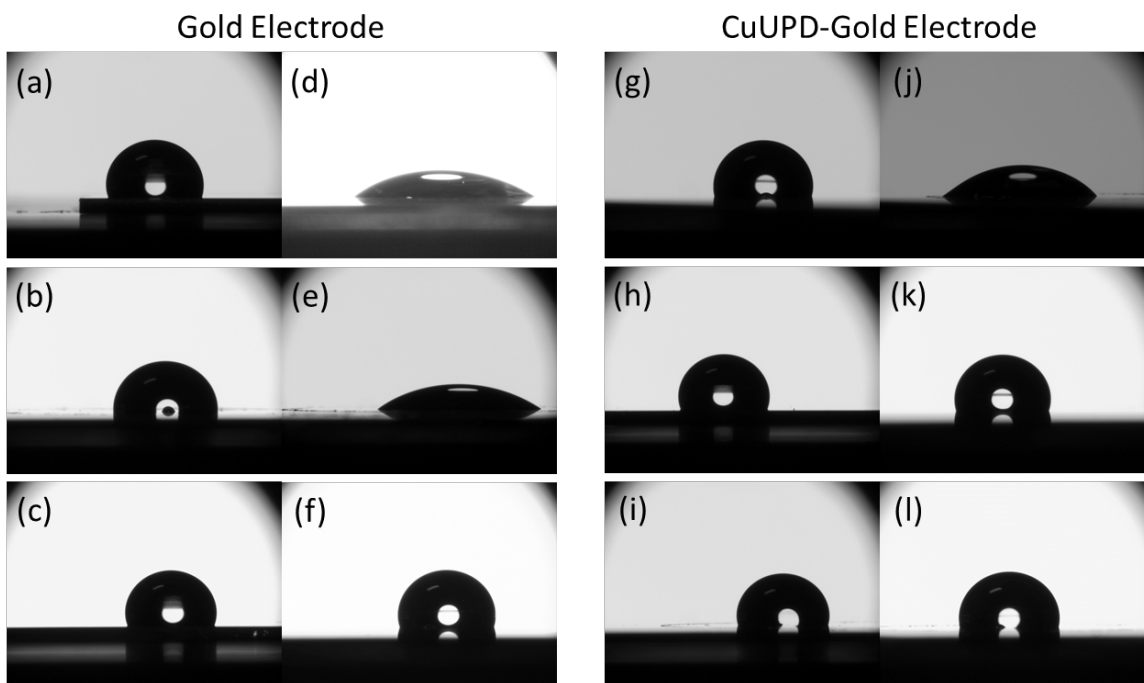
Figure 4.17 Water contact angle images of an alkanethiol monolayer on a gold and copperUPD-gold electrode before and after 30 CV cycles. The leftmost column of images are for a fresh **(a)** DT, **(b)** DDT, and **(c)** ODT monolayer on a gold electrode. The second column are the contact angle images of a **(d)** DT, **(e)** DDT, and **(f)** ODT monolayer after 30 CV cycles. For a copperUPD-gold electrode, the images for a fresh DT, DDT, and ODT monolayer are shown in **(g)**, **(h)**, and **(i)**, respectively. The rightmost column of images are for a **(j)** DT, **(k)** DDT, and **(l)** ODT monolayer on a copperUPD-gold electrode after 30 CV cycles.

After 30 CV cycles, the contact angle images show significant changes for a DT and DDT on a gold electrode and for DT on a copperUPD-gold electrode. This is seen in Figure 4.17 (d), (e), and (j), respectively. The decrease in contact angle is attributed to the electrodesorbing of the alkanethiol monolayer and the increase in wettability of the surface. The measured contact angles are 33°, 45°, and 34°, respectively. Similarly to the results from SHG and SFG, the contact angles for ODT on gold, DDT on copperUPD-gold, and for ODT on copperUPD-gold measured 99°, 89°, and 98°, respectively, which implied

the existence of a well-ordered SAM at the electrode surface. The contact angle images and measurements confirmed the results from in-situ SHG.

4.8 Discussion

The adsorption of alkanethiols on gold creates a thiolate-gold bond shown in the following equation. With the addition of an UPD layer of copper on gold, there is an expected change in the self-assembly mechanism. This is noted by the binding structures of both sulfur and copper with gold.

$$Au(0) + HSR\ (solution) \rightarrow Au—SR + \tfrac{1}{2}\ H_2\ (g) \qquad\qquad [4.1]$$
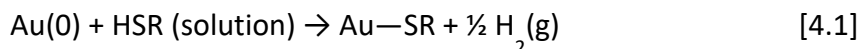
From literature, thiolates form a $(\sqrt{3} \times \sqrt{3})R30°$ structure relative to a Au(111) substrate with the alkyl chains aligning in an all-trans configuration.[4, 8, 16, 18, 25, 29, 31-32] While for evaporated gold films, the binding structure is not certain, SFG suggests an all-trans configuration given the lack of methylene stretches. An all-trans configuration is also measured for a SAM on the copperUPD-gold electrode, but the thiolates interaction with the gold and copperUPD layer is convoluted. At submonolayer coverages, the copper UPD layer forms a $(\sqrt{3} \times \sqrt{3})R30°$ adlayer on Au(111) followed by a (1 × 1) adlayer at higher coverages.[1-2, 33-35] With a thiolates desired binding sites taken by copper, the structural arrangement of the adsorbates must be altered on the UPD layer from those on the gold substrate. This is presumed due to differences seen in both the CV and the SH intensities between the gold and copperUPD-gold electrode. Also, from a qualitative

inspection of the binding energies for the S $2p_{3/2}$ peak in Figure 4.16 (a), there is a slight separation in binding energies between electrodes for a fresh monolayer.

Given the noted differences for the self-assembly process at a gold and copperUPD-gold electrode, a difference in the electrodesorption of DT, DDT, and ODT from the two electrodes was also expected. Alkanethiols can reductively desorb from gold in a two-step process shown in Equations 4.2 and 4.3.

$$Au—SR + e^- \rightarrow Au(0) + {}^-SR \text{ (surface)} \qquad [4.2]$$

$$Au(0) + {}^-SR \text{ (surface)} \rightarrow Au(0) + {}^-SR \text{ (solution)} \qquad [4.3]$$
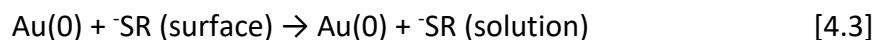
As necessary negative potentials are applied, the gold surface gains an electrode as the thiolate-gold bond is cleaved. The chemically desorbed thiolate species dissolves into the electrolyte solution at different rates depending on the solubility and diffusion coefficient of the thiolates.

In-situ SHG monitored the electrodesorption process of alkanethiols from a gold and copperUPD-gold electrode. For a gold electrode, the short chain alkanethiols, DT and DDT, were desorbed from the substrate. The long chain alkanethiol, ODT, was not reductively desorbed after 30 CV cycles. Instead, ODT is desorbed and remains near the surface of the electrode, which is attributed to the decrease in solubility of the desorbed thiolates in aqueous solutions, and can be oxidatively readsorbed.[19-21, 36] These results were confirmed through ex-situ techniques of SFG, XPS, and CA.

For the copperUPD-gold electrode, DT and ODT monolayers behaved similarly to the monolayers self-assembled on a gold electrode. The short chain alkanethiol readily desorbed, while the long chain alkanethiol remained in the vicinity of the electrode. Interestingly, DDT did not behave like the short chain DT monolayer on the copperUPD-gold electrode nor the DDT monolayer on a gold electrode. After 30 CV scans, all techniques suggested a well-ordered DDT monolayer remaining at the copperUPD-gold electrode surface.

The reduction of alkanethiolates resulted in a change in charge at the electrode surface. This change was observed by the SH response. Firstly, while the CVs of a copperUPD-gold electrode showed no features characteristic of the reductive desorption of alkanethiols, the SH was sensitive to change in charge at the potential was cycled. At potentials where the electrodesorption process occurred, the SH decreased for both electrodes. However, there were notable differences in the SH response between electrode surfaces. The differences are evident for a DT monolayer after 10 scans on both a gold and copperUPD-gold electrode shown in Figure 4.7 (d). There is a slope difference in the SH between the electrodes, and also a significant gap between the cathodic and anodic scans for the copperUPD-gold electrode. The gap difference mimics the difference in the double layer region for both electrodes, respectively. While DT was successfully desorbed from both electrodes, the SH was sensitive to a corresponding difference between the electrode surface; the addition of a copper UPD layer.

Given the complexity of the system, a circuit is proposed in Figure 4.18 to show the contribution of each component. There are four capacitors contributing to the system: the gold capacitance, Q_{Au}, the UPD capacitance, Q_{UPD}, the double layer capacitance, Q_{dl}, and the capacitance of stray molecules in the electrolyte, Q_{stray}. The resistors R_{Au}, R_{UPD}, R_{CT}, R_{un}, and R_s correspond to the gold, UPD layer, charge transfer, uncompensated resistance, and the solution. In literature, the calculated capacitance density of a bare gold electrode is about 55 µF/cm^2.[21] Given a lead UPD layer on the gold, the capacitance density is between 10 and 20 µF/cm^2.[37] This difference in capacitance for a lead UPD layer on gold provides a reason to infer a change in capacitance for a copperUPD-gold electrode. Notably, the differences observed in the SH response between the gold and copperUPD-gold electrodes further suggest a change in capacitance. This parallels with a change in the electron density of the electrode corresponding to a change in the Fermi level of the metal.
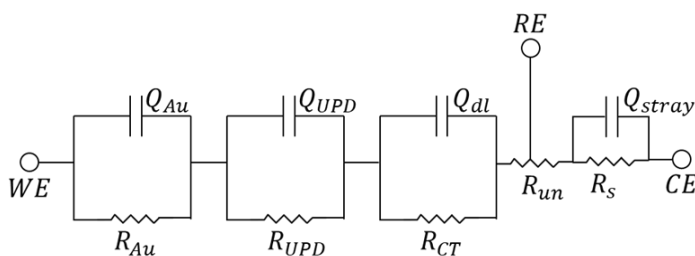

Figure 4.18 Proposed circuit for the underpotential deposition of copper onto gold.

Furthermore, a significant difference is observed in the SH response between electrodes for the reductive desorption of ODT. For a gold electrode, the SH decreases as sufficiently negative potentials are reached to electrodesorbed the long chain alkanethiol.

However, as stated above, long chain alkanethiols desorbed yet remain in the vicinity of the electrode surface. This is confirmed by both in-situ SHG and ex-situ SFG. The SH behaves similarly to a DT monolayer at a gold surface where the stripping of the alkanethiol results in a decrease in the SH, but SFG shows a well-ordered monolayer after 30 CV cycles. Alternatively, the SH response to the electrodesorption of ODT on a copperUPD-gold electrode shows no change. These variances between the SH behavior supports the contribution of a capacitance difference between electrode surfaces. For a gold electrode, electrochemical impedance spectroscopy revealed differences to the total interfacial capacitance density before and after reductive desorption.[21] For a fresh DT, DDT, and ODT monolayer on gold, the total interfacial capacitance density was 1.63, 1.41, and 0.79 $\mu F/cm^2$, respectively.[21] Compared to a bare gold electrode, there is a significant decrease in capacitance with the addition of an alkanethiol. There is also a decrease in capacitance as the alkanethiol chain length increases from DT to ODT. After 30 CV cycles, the total interfacial capacitance density of DT, DDT, and ODT was 11.79, 17.14, and 1.04 $\mu F/cm^2$, respectively.[21] For the short chain alkanethiols, there was an increase in capacitance, which was comparable to a double layer capacity of a polycrystalline gold electrode.[38] This supported the SH and SFG data, which showed a successful desorption of DT and DDT from a gold electrode. However, for ODT, there is only a small increase in capacitance pointing to the monolayer remaining near the surface in the double layer region. Applying these results from literature with our system, it is expected that the alkanethiols behave similarly on a copperUPD-gold electrode with the exception of DDT.

Given the difference in the SH response, DDT showed a behavior similar to ODT on a copperUPD-gold electrode. This would imply that the copper UPD layer is further changing the capacitance and stabilizing the alkanethiol monolayers compared with a bare electrode. However, further investigation and experiments are needed to confirm this.

4.9 Conclusion

CV and SHG results showed a difference between the electrodesorption of alkanethiols from a gold and copperUPD-gold electrode. The change in SH is attributed to the change in capacitance between a gold and copperUPD-gold electrode. When the SAM was formed on the copperUPD-gold electrode, the reductive potentials were pushed to more negative potentials, which resulted in a lack of desorption features in the corresponding CVs due to the HER. The copperUPD layer stabilized the SAMs. This effect is most noticeable for DDT where the SAM was reductively desorbed from a gold electrode, but remained near the surface for the copperUPD-gold electrode. This was confirmed with ex-situ techniques of SFG, XPS, and CA.

4.10 References

1.   Jennings, G. K.; Laibinis, P. E., Self-Assembled n-Alkanethiolate Monolayers on Underpotentially Deposited Adlayers of Silver and Copper on Gold. *Journal of the American Chemical Society* **1997,** *119* (22), 5208-5214.

2.   Herrero, E.; Buller, L. J.; Abruña, H. D., Underpotential Deposition at Single Crystal Surfaces of Au, Pt, Ag and Other Materials. *Chemical Reviews* **2001,** *101* (7), 1897-1930.

3.   Laibinis, P. E.; Bain, C. D.; Whitesides, G. M., Attenuation of photoelectrons in monolayers of n-alkanethiols adsorbed on copper, silver, and gold. *The Journal of Physical Chemistry* **1991,** *95* (18), 7017-7021.

4.   Schreiber, F., Structure and growth of self-assembling monolayers. *Progress in Surface Science* **2000,** *65* (5), 151-257.

5.   Porter, M. D.; Bright, T. B.; Allara, D. L.; Chidsey, C. E., Spontaneously organized molecular assemblies. 4. Structural characterization of n-alkyl thiol monolayers on gold by optical ellipsometry, infrared spectroscopy, and electrochemistry. *Journal of the American Chemical Society* **1987,** *109* (12), 3559-3568.

6.   Jennings, G. K.; Laibinis, P. E., Self-assembled monolayers of alkanethiols on copper provide corrosion resistance in aqueous environments. *Colloids and Surfaces A: Physicochemical and Engineering Aspects* **1996,** *116* (1), 105-114.

7.   Swalen, J. D.; Allara, D.; Andrade, J. D.; Chandross, E.; Garoff, S.; Israelachvili, J.; McCarthy, T.; Murray, R.; Pease, R., Molecular monolayers and films. A panel

report for the materials sciences division of the department of energy. *Langmuir* **1987,** *3* (6), 932-950.

8.   Laibinis, P. E.; Whitesides, G. M., Self-assembled monolayers of n-alkanethiolates on copper are barrier films that protect the metal against oxidation by air. *Journal of the American Chemical Society* **1992,** *114* (23), 9022-9028.

9.   Feng, Y.; Teo, W. K.; Siow, K. S.; Gao, Z.; Tan, K. L.; Hsieh, A. K., Corrosion protection of copper by a self-assembled monolayer of alkanethiol. *Journal of The Electrochemical Society* **1997,** *144* (1), 55-64.

10.   Jennings, G. K.; Munro, J. C.; Yong, T.-H.; Laibinis, P. E., Effect of Chain Length on the Protection of Copper by n-Alkanethiols. *Langmuir* **1998,** *14* (21), 6130-6139.

11.   Yamamoto, Y.; Nishihara, H.; Aramaki, K., Self-Assembled Layers of Alkanethiols on Copper for Protection Against Corrosion. *Journal of the Electrochemical Society* **1993,** *140* (2), 436-443.

12.   Hutt, D. A.; Liu, C., Oxidation protection of copper surfaces using self-assembled monolayers of octadecanethiol. *Applied Surface Science* **2005,** *252* (2), 400-411.

13.   Canning, N. D. S.; Outka, D.; Madix, R. J., The adsorption of oxygen on gold. *Surface Science* **1984,** *141* (1), 240-254.

14.   Heister, K.; Zharnikov, M.; Grunze, M.; Johansson, L. S. O., Adsorption of Alkanethiols and Biphenylthiols on Au and Ag Substrates: A High-Resolution X-ray Photoelectron Spectroscopy Study. *The Journal of Physical Chemistry B* **2001,** *105* (19), 4058-4061.

15. Vickerman, J. C.; Gilmore, I. S., *Surface Analysis: The Principal Techniques*. John Wiley & Sons: United Kingdom, 2011.

16. Laibinis, P. E.; Whitesides, G. M.; Allara, D. L.; Tao, Y. T.; Parikh, A. N.; Nuzzo, R. G., Comparison of the structures and wetting properties of self-assembled monolayers of n-alkanethiols on the coinage metal surfaces, copper, silver, and gold. *Journal of the American Chemical Society* **1991,** *113* (19), 7152-7167.

17. Zhong, C.-J.; Porter, M. D., Fine structure in the voltammetric desorption curves of alkanethiolate monolayers chemisorbed at gold. *Journal of Electroanalytical Chemistry* **1997,** *425* (1), 147-153.

18. Azzaroni, O.; Vela, M. E.; Fonticelli, M.; Benítez, G.; Carro, P.; Blum, B.; Salvarezza, R. C., Electrodesorption Potentials of Self-Assembled Alkanethiolate Monolayers on Copper Electrodes. An Experimental and Theoretical Study. *The Journal of Physical Chemistry B* **2003,** *107* (48), 13446-13454.

19. Thom, I.; Buck, M., On the Interpretation of Multiple Waves in Cyclic Voltammograms of Self-Assembled Monolayers of n-Alkane Thiols on Gold. In *Zeitschrift für Physikalische Chemie*, 2008; Vol. 222, p 739.

20. Jacob, J. D. C.; Lee, T. R.; Baldelli, S., In Situ Vibrational Study of the Reductive Desorption of Alkanethiol Monolayers on Gold by Sum Frequency Generation Spectroscopy. *The Journal of Physical Chemistry C* **2014,** *118* (50), 29126-29134.

21. Cai, X.; Baldelli, S., Surface Barrier Properties of Self-Assembled Monolayers as Deduced by Sum Frequency Generation Spectroscopy and Electrochemistry. *The Journal of Physical Chemistry C* **2011,** *115* (39), 19178-19189.

22. Hines, M. A.; Todd, J.; Guyot-Sionnest, P., Conformation of alkanethiols on Au, Ag (111), and Pt (111) electrodes: A vibrational spectroscopy study. *Langmuir* **1995,** *11* (2), 493-497.

23. Ong, T. H.; Davies, P. B.; Bain, C. D., Sum-frequency spectroscopy of monolayers of alkoxy-terminated alkanethiols in contact with liquids. *Langmuir* **1993,** *9* (7), 1836-1845.

24. Ron, H.; Cohen, H.; Matlis, S.; Rappaport, M.; Rubinstein, I., Self-Assembled Monolayers on Oxidized Metals. 4. Superior n-Alkanethiol Monolayers on Copper. *The Journal of Physical Chemistry B* **1998,** *102* (49), 9861-9869.

25. Chidsey, C. E.; Loiacono, D. N., Chemical functionality in self-assembled monolayers: structural and electrochemical properties. *Langmuir* **1990,** *6* (3), 682-691.

26. Guyot-Sionnest, P.; Hunt, J. H.; Shen, Y. R., Sum-frequency vibrational spectroscopy of a Langmuir film: Study of molecular orientation of a two-dimensional system. *Physical Review Letters* **1987,** *59* (14), 1597-1600.

27. Nuzzo, R. G.; Korenic, E. M.; Dubois, L. H., Studies of the temperature-dependent phase behavior of long chain n-alkyl thiol monolayers on gold. *The Journal of chemical physics* **1990,** *93* (1), 767-773.

28.   Sung, M. M.; Sung, K.; Kim, C. G.; Lee, S. S.; Kim, Y., Self-Assembled Monolayers of Alkanethiols on Oxidized Copper Surfaces. *The Journal of Physical Chemistry B* **2000,** *104* (10), 2273-2277.

29.   Nuzzo, R. G.; Zegarski, B. R.; Dubois, L. H., Fundamental studies of the chemisorption of organosulfur compounds on gold (111). Implications for molecular self-assembly on gold surfaces. *Journal of the American Chemical Society* **1987,** *109* (3), 733-740.

30.   Bain, C. D.; Biebuyck, H. A.; Whitesides, G. M., Comparison of self-assembled monolayers on gold: coadsorption of thiols and disulfides. *Langmuir* **1989,** *5* (3), 723-727.

31.   Rieley, H.; Kendall, G. K.; Jones, R. G.; Woodruff, D. P., X-ray Studies of Self-Assembled Monolayers on Coinage Metals. 2. Surface Adsorption Structures in 1-Octanethiol on Cu(111) and Ag(111) and Their Determination by the Normal Incidence X-ray Standing Wave Technique. *Langmuir* **1999,** *15* (26), 8856-8866.

32.   Dubois, L. H.; Nuzzo, R. G., Synthesis, structure, and properties of model organic surfaces. *Annual review of physical chemistry* **1992,** *43* (1), 437-463.

33.   Koos, D.; Richmond, G., Structure and stability of underpotentially deposited layers on gold (111) studied by optical second harmonic generation. *The Journal of Physical Chemistry* **1992,** *96* (9), 3770-3775.

34.   Tadjeddine, A.; Guay, D.; Ladouceur, M.; Tourillon, G., Electronic and structural characterization of underpotentially deposited submonolayers and monolayer of

copper on gold (111) studied by in situ x-ray-absorption spectroscopy. *Physical Review Letters* **1991,** *66* (17), 2235-2238.

35. Omar, I. H.; Pauling, H.; Jüttner, K., Underpotential Deposition of Copper on Au (III) Single-Crystal Surfaces A Voltammetric and Rotating Ring Disk Electrode Study. *Journal of The Electrochemical Society* **1993,** *140* (8), 2187-2192.

36. Thom, I.; Buck, M., Electrochemical stability of self-assembled monolayers of biphenyl based thiols studied by cyclic voltammetry and second harmonic generation. *Surface Science* **2005,** *581* (1), 33-46.

37. Chang, B.-Y.; Ahn, E.; Park, S.-M., Real-Time Staircase Cyclic Voltammetry Fourier Transform Electrochemical Impedance Spectroscopic Studies on Underpotential Deposition of Lead on Gold. *The Journal of Physical Chemistry C* **2008,** *112* (43), 16902-16909.

38. Janek, R. P.; Fawcett, W. R.; Ulman, A., Impedance Spectroscopy of Self-Assembled Monolayers on Au(111): Evidence for Complex Double-Layer Structure in Aqueous NaClO4 at the Potential of Zero Charge. *The Journal of Physical Chemistry B* **1997,** *101* (42), 8550-8558.